

ABSTRACT

Title of Document:

**THE ADI-FDTD METHOD FOR HIGH
ACCURACY ELECTROPHYSICS
APPLICATIONS**

Mohammad Haeri Kermani,
Doctor of Philosophy, 2006

Directed By:

Professor Omar M. Ramahi,
Mechanical Engineering Department,
Electrical and Computer Engineering Department

The Finite-Difference Time-Domain (FDTD) is a dependable method to simulate a wide range of problems from acoustics, to electromagnetics, and to photonics, amongst others. The execution time of an FDTD simulation is inversely proportional to the time-step size. Since the FDTD method is explicit, its time-step size is limited by the well-known Courant-Friedrich-Levy (CFL) stability limit. The CFL stability limit can render the simulation inefficient for very fine structures. The Alternating Direction Implicit FDTD (ADI-FDTD) method has been introduced as an unconditionally stable implicit method. Numerous works have shown that the ADI-FDTD method is stable even when the CFL stability limit is exceeded. Therefore, the

ADI-FDTD method can be considered an efficient method for special classes of problems with very fine structures or high gradient fields.

Whenever the ADI-FDTD method is used to simulate open-region radiation or scattering problems, the implementation of a mesh-truncation scheme or absorbing boundary condition becomes an integral part of the simulation. These truncation techniques represent, in essence, differential operators that are discretized using a distinct differencing scheme which can potentially affect the stability of the scheme used for the interior region. In this work, we show that the ADI-FDTD method can be rendered unstable when higher-order mesh truncation techniques such as Higdon's Absorbing Boundary Condition (ABC) or Complementary Derivatives Method (COM) are used.

When having large field gradients within a limited volume, a non-uniform grid can reduce the computational domain and, therefore, it decreases the computational cost of the FDTD method. However, for high-accuracy problems, different grid sizes increase the truncation error at the boundary of domains having different grid sizes. To address this problem, we introduce the Complementary Derivatives Method (CDM), a second-order accurate interpolation scheme. The CDM theory is discussed and applied to numerical examples employing the FDTD and ADI-FDTD methods.

THE ADI-FDTD METHOD FOR HIGH ACCURACY ELECTROPHYSICS
APPLICATIONS

By

Mohammad Haeri Kermani

Dissertation submitted to the Faculty of the Graduate School of the
University of Maryland, College Park, in partial fulfillment
of the requirements for the degree of
Doctor of Philosophy
2006

Advisory Committee:
Professor Omar M. Ramahi, Chair
Professor Thomas M. Antonsen
Professor Christopher Davis
Professor Victor Granatstein
Professor Peter Sandborn

© Copyright by
Mohammad Haeri Kermani
2006

Dedication

I dedicate this dissertation to my parents for their love, sacrifices, and encouragement through the years.

Acknowledgments

I owe my gratitude to all the people who have made this dissertation possible. First and foremost I would like to thank my parents. If it was not for their love, sacrifices, and encouragement through the years, I would not be able to accomplish what I did.

Among the people who contributed to my academic success, my greatest appreciation surely belongs to my research advisor, Professor Omar M. Ramahi, for his guidance, understanding, patience, and most importantly, his friendship during my graduate studies at the University of Maryland. He encouraged me to not only grow as an engineer but also as a researcher and independent thinker.

I would also like to thank Professors Thomas M. Antonsen, Christopher Davis, Victor Granatstein, and Peter Sandborn for serving on my dissertation committee and providing many valuable comments.

During the past four and a half years at the University of Maryland, I have enjoyed the friendship of many great people. I would like to thank all of my good friends at the University of Maryland, especially those at the Electromagnetic Compatibility and Propagation Lab.

Table of Contents

DEDICATION.....	II
ACKNOWLEDGMENTS	III
TABLE OF CONTENTS	IV
LIST OF FIGURES	VII
LIST OF TABLES	XII
CHAPTER 1 INTRODUCTION.....	1
CHAPTER 2 LITERATURE REVIEW OF THE ADI-FDTD METHOD.....	8
CHAPTER 3 THEORY OF ADI-FDTD METHOD.....	20
3.1 STABILITY OF THE ADI-FDTD METHOD	24
3.2 NUMERICAL DISPERSION RELATION OF THE ADI-FDTD METHOD.....	27
CHAPTER 4 NUMERICAL IMPLEMENTATION OF THE ADI-FDTD	
METHOD.....	29
4.1 CODE VERIFICATION: RESONANT FREQUENCY OF CAVITY	29
4.2 CODE VERIFICATION: FREE SPACE WAVE PROPAGATION	31
4.3 ANTENNA APPLICATION	32
CHAPTER 5 ABSORBING BOUNDARY CONDITION (ABC).....	39
5.1 THEORY	39
5.2 HIGDON’S ABC	41
5.2.1 <i>Implementation of the Higdon’s ABC in the ADI-FDTD Method</i>	<i>43</i>

5.3	COMPLEMENTARY OPERATORS METHOD (COM)	45
5.3.1	<i>Implementation of COM in the ADI-FDTD Method</i>	49
5.3.2	<i>Analytical Investigation of Instability of the COM Using the Z-transform</i>	50
CHAPTER 6 COMPLEMENTARY DERIVATIVES METHOD		55
6.1	CDM THEORY	55
6.2	NUMERICAL EXPERIMENTS	62
6.2.1	<i>One-dimensional Experiments</i>	62
6.2.2	<i>Two-dimensional Experiments</i>	68
6.2.3	<i>Three-dimensional Experiments</i>	77
6.3	ANALYTICAL INVESTIGATION OF CDM	83
6.3.1	<i>Fundamental Modes of Propagation in the Numerical Solution: Advection Equation</i>	83
6.3.2	<i>Reflection from Grid Boundary: Standard Treatment of the Grid Boundary in Advection Equation</i>	86
6.3.3	<i>Reflection from Grid Boundary: CDM Treatment of the Grid Boundary in Advection Equation</i>	90
6.3.4	<i>Fundamental Modes of Propagation in the Numerical Solution: Leap-Frog Scheme of the Wave Equation</i>	93
6.3.5	<i>Reflection from Grid Boundary: Standard Treatment of Grid Boundary in the Wave Equation</i>	97
6.3.6	<i>Reflection from Grid Boundary: CDM Treatment of Grid Boundary in the Wave Equation</i>	100

6.3.7	<i>Results</i>	103
6.4	IMPLEMENTING THE CDM IN THE ADI-FDTD METHOD	105
6.4.1	<i>Numerical Experiments</i>	113
CHAPTER 7	CONCLUSIONS AND FUTURE WORK	117
7.1	CONCLUSIONS	117
7.2	FUTURE WORK	118
BIBLIOGRAPHY	119

List of Figures

Fig. 4.1-1	Dimensions and grid size of cavity.	29
Fig. 4.1-2	Relative errors of the calculated resonant frequencies vs. time-step size.	30
Fig. 4.2-1	Structure of the three-dimensional open-region simulation and the locations of source and monitor points.	31
Fig. 4.2-2	Values of ϵ_x calculated using the ADI-FDTD (solid line) and FDTD methods (solid line with squares).	32
Fig. 4.3-1	Dimensions of patch antenna.	33
Fig. 4.3-2	Structure simulated by the ADI-FDTD method.	34
Fig. 4.3-3	Structure of grids in the z -direction.	35
Fig. 4.3-4	S_{11} in dB for fine grid (Fig. 4.3-3 a).	36
Fig. 4.3-5	S_{11} in dB for coarse grid (Fig. 4.3-3 b).	37
Fig. 4.3-6	S_{11} in dB for a coarse grid in the z -direction which is refined around the antenna plane (Fig. 4.3-3 c).	38
Fig. 5.2-1	Structure of three-dimensional open-region simulation and the locations of source and monitor points.	43
Fig. 5.2-2	Simulation results of the first-, and third-order Higdon's ABCs implemented in the ADI-FDTD method.	44
Fig. 5.2-3	Scaled simulation results of the first, and third-order Higdon's ABCs implemented in the ADI-FDTD method.	45
Fig. 5.3-1	Outgoing and incoming waves at the computational boundary.	46
Fig. 5.3-2	Outgoing and complementary incoming waves at the computational boundary.	47

Fig. 5.3-3 Complementary reflections and average of them that cancels the first-order reflection.....	47
Fig. 5.3-4 Simulation results of the second-order COM implemented in the ADI-FDTD method.	49
Fig. 5.3-5 Scaled simulation results of the second-order COM implemented in the ADI-FDTD method.....	50
Fig. 6.1-1 Arrangement of E -fields and H -fields along the x -axis in the FDTD domain based on the Yee scheme. The grid size changes from Δ to Δ^R at the grid boundary.....	56
Fig. 6.1-2 FDTD E - and H -field nodes used for the implementation of CDM in the one-dimensional simulation.....	59
Fig. 6.1-3 Two-dimensional discretized structure. The grid size in the x -direction changes from Δ_x to Δ_x^R at x_0 and in the y -direction changes from Δ_y to Δ_y^R at y_0	62
Fig. 6.2.1-1 One-dimensional reference structure. The grid size is uniform ($\Delta=125\mu m$) throughout the domain.	63
Fig. 6.2.1-2 Simulated structure with different grid sizes. The grid size on the left side of the grid boundary is $\Delta=250\mu m$ and on the right side of the grid boundary is $\Delta' = 125\mu m$	64
Fig. 6.2.1-3 One-Dimensional FDTD simulation results using different grid size scenarios; Reference: Standard Yee scheme applied to a domain with a uniform cell size of $\Delta = 125\mu m$. Case 1: Standard Yee scheme applied to two domains with different grid sizes of $\Delta = 250\mu m$ and $\Delta' = 125\mu m$. Case 2: CDM applied to two domains with different grid sizes of $\Delta = 250\mu m$ and $\Delta' = 125\mu m$	65

Fig. 6.2.1-4 Simulated structure as reference. The grid size is $\Delta=50\mu m$ on the entire domain.....	66
Fig. 6.2.1-5 Simulated structure with different grid sizes. The grid size on the left side of the grid boundary is $\Delta = 200\mu m$ and on the right side of the grid boundary is $\Delta' = 50\mu m$	66
Fig. 6.2.1-6 Two different sets of complementary derivatives for a grid size reduction factor of $\alpha=1/4$	67
Fig. 6.2.1-7 One-dimensional FDTD simulation results using different grid size scenarios. Reference: Standard Yee scheme applied to a domain with a uniform cell size of $\Delta = 50\mu m$. Different Grid size: Standard Yee scheme applied to two domains with different grid sizes of $\Delta = 200\mu m$ and $\Delta' = 50\mu m$. CDM, Method 1: CDM (Method 1, Fig. 6.2.1-6 (a)) is applied to two domains with different grid sizes of $\Delta = 200\mu m$ and $\Delta' = 50\mu m$. CDM, Method 2: CDM (Method 2, Fig. 6.2.1-6 (b)) is applied to two domains with different grid sizes of $\Delta = 200\mu m$ and $\Delta' = 50\mu m$	68
Fig. 6.2.2-1 Simulated structure as reference. The grid size is uniform ($\Delta x=\Delta y=1mm$) throughout the computational domain.	69
Fig. 6.2.2-2 Simulated structure with different grid sizes. The grid size in the y-direction is uniform ($\Delta y=1mm$) on the entire domain. The grid size in the x-direction changes from $\Delta x = 1mm$ to $\Delta x' = 0.5, 0.25,$ and $0.125mm$	70
Fig. 6.2.2-3 Normalized error in the E-field as obtained using the standard FDTD interpolation scheme with and without CDM.....	71
Fig. 6.2.2-4 Dielectric slab-loaded rectangular waveguide.	72

Fig. 6.2.2-5 Discretized structure using a uniform grid size of $\Delta x = \Delta y = \Delta = 0.1942mm$	73
Fig. 6.2.2-6 Discretized structure using a uniform grid size of $\Delta x = \Delta y = \Delta = 0.6657mm$	74
Fig. 6.2.2-7 Structure is discretized uniformly in the x -direction with $\Delta x = 0.6657mm$. In the y -direction, the original grid size of $\Delta y = 0.6657mm$ is refined to $\Delta y' = 0.33285mm$ in the vicinity of the grid boundary.	75
Fig. 6.2.3-1 Structure of the three-dimensional simulation domain.	78
Fig. 6.2.3-2 Normalized error in the E-field as obtained using the standard FDTD interpolation scheme with and without CDM.....	79
Fig. 6.2.3-3 Cross section of the waveguide with an infinitely thin slot-line as the center conductor. The exact impedance is $Z_c = 94.2\Omega$	80
Fig. 6.2.3-4 Discretized structure of the waveguide with infinitely thin slot-line as center conductor.....	81
Fig. 6.2.3-5 Discretized structure of slot-line waveguide.....	82
Fig. 6.3.1-1 Uniform grid.....	83
Fig. 6.3.2-1 Non-uniform grid.	87
Fig. 6.3.2-2 Wave is propagating from left to right. In addition to the rightward waves in $X < 0$ and $X > 0$, there is a reflection from the interface in $X < 0$	88
Fig. 6.3.3-1 Implementing the CDM on a non-uniform grid.	90
Fig. 6.3.4-1 Leap-frog scheme to solve the wave equation.	94
Fig. 6.3.4-2 Leap-frog scheme to solve the wave equation. A uniform grid is used.	96
Fig. 6.3.5-1 Non-uniform grid in leap-frog scheme.....	98

Fig. 6.3.6-1	Implementing CDM on a non-uniform grid.....	101
Fig. 6.3.7-1	Reflection coefficient of the advection equation at grid boundary; refined mesh, coarsened mesh, and the CDM treatment of grid boundary.....	104
Fig. 6.3.7-2	Reflection coefficient of the wave equation at grid boundary; refined mesh, coarsened mesh, and the CDM treatment of grid boundary.....	105
Fig. 6.4-1	Two-dimensional discretized domain. The grid is uniform in the x - direction with the grid size of Δx . The grid size is non-uniform in the y -direction and changes from Δy to $\Delta y'$ at $j=j_0$	106
Fig. 6.4.1-1	Simulated structure as reference. The grid size is uniform ($\Delta x=\Delta y=1mm$) throughout the computational domain.....	114
Fig. 6.4.1-2	Simulated structure with different grid sizes. The grid size in the y - direction changes from $\Delta y=1mm$ to $\Delta y'=0.5, 0.25, 0.125mm$ at $j_0=32mm$	115
Fig. 6.4.1-3	Normalized error in the H -field as obtained using the ADI-FDTD method with and without CDM.	116

List of Tables

Table 4.1-1	Comparing the calculated resonant frequencies of the cavity using HFSS, FDTD, and ADI-FDTD to theory.....	30
Table 4.3-1	The first calculated resonant frequency for different grid structures in the z -direction.....	38
Table 6.2.2-1	Simulated cutoff frequencies and the analytical result.	77
Table 6.2.3-1	Error in calculated characteristic impedance using uniform and non-uniform grids with and without CDM.	82

Chapter 1 Introduction

The scientific community has become dependent on the Finite-Difference Time-Domain (FDTD) method to simulate a wide range of problems from acoustics, to electromagnetics, and to photonics, amongst others [1-1], [1-2]. The FDTD method has some good features which make it superior to the other methods. The FDTD method is simple to understand and straightforward to implement in software. The time-stepping nature of the FDTD method enables the visualization of the electromagnetic fields inside the model under investigation. Calculating a wide-band transfer function by performing a single simulation is the other important feature of the FDTD method. This is in sharp contrast to the frequency-domain methods which the transfer function of each frequency is calculated using one single simulation.

In the FDTD method, a uniform grid is utilized to mesh the structure. The central-difference scheme is used to approximate the first-order derivatives in the Maxwell's equations. Implementing the central-difference approximation on a uniform grid leads to a second-order accurate solution in both time and space and provides sufficient accuracy for a wide variety of applications.

The FDTD simulation usually needs to be run up to the time instant at which the time-domain signal reaches its steady state. The execution time of an FDTD simulation is inversely proportional to the time-step size. Since the FDTD is an explicit method, its time-step size is limited by the well-known Courant-Friedrichs-Lewy (CFL) stability limit, which is a function of minimum grid sizes in the x -, y -, and z -directions (in Cartesian co-ordinates). Therefore, the maximum time-step is limited by the minimum grid sizes in the x -, y -, and z -directions.

Grid sizes are governed by two requirements. First, a grid should resolve the highest frequency of interest, which is usually accomplished by using at least 10 points per wavelength at this frequency [1-2]. Second, the grid size should be small enough to ensure that all objects in the computational domain are spatially resolved by the cells. For objects with the fine scale dimensions compared to wavelength (e.g. thin material coatings, transmission lines with conductors of small dimensions), the second requirement is the most restrictive on the spatial grid size.

Increasing the time-step size beyond the CFL stability limit decreases the simulation time. Using an implicit scheme, the differential equations can be solved unconditionally stably and free of the CFL stability limit. Unfortunately, a fully implicit scheme requires the solution of a large linear system of equations representing the full volume discretization at each time-step. This becomes prohibitive for large practical problems.

A more efficient scheme is to split the operators such that the time-integration is implicit only along a single coordinate axis. This scheme is commonly referred to as Alternating Direction Implicit (ADI). The alternating direction implicit finite-difference time-domain (ADI-FDTD) method for solving electromagnetic radiation and scattering problems was introduced in [1-3] and [1-4]. It has been demonstrated that the ADI-FDTD method is unconditionally stable [1-3], [1-4]. The ADI-FDTD method allows for increasing the time-step size beyond the CFL stability limit, which results in a substantial reduction in the total execution time of numerical problems.

Whenever the ADI-FDTD method is used to simulate the open-region radiation or scattering problems, the implementation of a mesh-truncation scheme or

absorbing boundary condition [1-5]-[1-8] becomes an integral part of the simulation. For many applications of the ADI-FDTD method, the required duration of simulation needs only to extend over enough time steps to capture the bulk of the output energy or pulse at a desired point of observation. For such problems, the stability behavior of the mesh-truncation techniques does not pose a serious challenge. However, there is a wide class of problems where the output time signature needs to be obtained for a very long duration in order to reproduce the response of the system over a wide frequency band (via the Fourier transformation). For this important class of problems, care must be taken to ensure that the evolution of the field in time does not exhibit any unstable behavior. Therefore, we need to insure that the implementation of absorbing boundary condition does not introduce any instability.

The Higdon's absorbing boundary condition [1-6], [1-7] is very versatile and simple to implement. The other useful mesh truncation technique is the Complementary Operators Method (COM) [1-9]-[1-11]. The basic premise of the COM is the cancellation of the first-order reflection that arises when the computational domain is terminated with an ABC. This cancellation is made by averaging two independent solutions to the problem. These two solutions are obtained by imposing boundary operators that are complementary to each other. Therefore, two solutions that are generated from applying each of the two operators separately, when averaged, result in a solution that does not contain any of the first-order reflections. In this work, we apply the Higdon's ABC and COM on the outer surfaces of simulation domains and study the stability of these boundary conditions.

Nowadays, there is a widespread demand for very high accurate simulations. These very high accurate simulations are needed to provide results which can parallel the accuracy of recent measurement equipments (*136dB* accuracy is becoming standard on a variety of commercial test instruments), or can measure the shielding effectiveness up to *120dB*, or can measure the reflections from the absorbers that goes down to *-55dB*. High-order interpolation schemes can provide higher accuracy at the expense of losing the solution efficiency. However, even the high-order interpolation schemes suffer from flexibility when electric or magnetic fields (or both) have large gradients within a limited volume. For example, Microwave Integrated Circuits (MIC), Monolithic Microwave Integrated Circuits (MMIC), in the vicinity of current sources, sharp edges and corners of conductive and dielectric objects, simulation of vias and bond wires in high-frequency electronic packages, and detailed simulations for biomedical applications, need a very fine mesh to resolve the abrupt changes of fields in a very small volume. Considering the limitation of the computer memory and speed, a very fine mesh for the whole domain renders this method not very attractive for this large class of electromagnetic problems.

Using a refined mesh in a sub-region is a solution to this problem. Several methods of obtaining a more refined mesh in a sub-region have previously been reported. They can be divided into two main categories, namely: 1) non-uniform grids; and 2) sub-gridding. In the first method where non-uniform grid is used, the gridding extends throughout the entire cross section of the domain. In the sub-gridding methods, a local grid with smaller size than the main grid is placed within a part of domain to resolve the finer geometry features or electromagnetic fields.

Using different grid sizes, however, increases the truncation error at the interface of two domains with different grid sizes. Such errors are typically manifested as reflections from the grid boundary. The reflection from a grid boundary is unacceptable in many applications ([1-20]-[1-22], simulations that can parallel high accurate measurements, calculating shielding effectiveness, calculating reflection from absorbers).

Several papers have introduced different methods to reduce the truncation error at grid boundaries. In [1-12], the grid size is reduced by one-third of the main grid size and the spatial derivatives of the fields at the interface are expressed by central-difference approximations to achieve the second-order accuracy. However, in this method, the reduced grid size is limited to specific numbers which limits its applicability to specific geometries that conform to specialized grid. In [1-13] and [1-14], the derivative of magnetic field at electric field position is approximated by fitting a second-degree polynomial to the magnetic fields at three points. The coefficient in the error term of this approximation, however, is large, which limits the grid size reduction factor. In [1-15], two methods were introduced to maintain the second-order accuracy. One method uses an appropriate mesh ratio between two regions to obtain the central finite differences. The other method uses a universal gridding scheme with continuously variable lattice size; but a demonstration of the performance of this method was not reported. In [1-16], the computational accuracy was improved by interpolating the magnetic field components between the fine mesh and coarse mesh, which cannot guarantee the second-order accuracy. In [1-17], a high-order implicit scheme was enforced at the boundary to reduce the truncation

error. In [1-18], a numerically-derived three-dimensional sub-gridding scheme was introduced but without theoretical limits on its potential. In [1-19], the characteristic impedances of two waveguides with infinitely thin and square center conductors are calculated using the accurate methods of conformal mapping and mode matching, respectively. Then, the values of minimum grid size and amplification factor have been optimized to obtain good approximations of the characteristic impedances using the FDTD method. But there is no explanation whether these values can also be used for other experiments or each experiment needs different optimized values, which is not practical.

The Complementary Derivatives Method (CDM) is introduced as a second-order accurate interpolation scheme applicable to Finite-Difference methods. Using several experiments, we demonstrate the performance of CDM in reducing the reflection from the boundary of two domains having different grid sizes. We derive the fundamental modes of propagation in a numerical solution of wave equation using a leap-frog scheme. Also, we calculate the reflection coefficients of advection and wave equations at the grid boundary when the CDM is applied and compare them with the reflection coefficients of a standard treatment of the grid boundary.

Also, we apply the CDM to the ADI-FDTD method. By employing the Sherman-Morrison formula, we retain the numerical efficiency of conventional ADI-FDTD method when the CDM treatment is applied at the grid boundary.

The remainder of this dissertation is organized as follows. In Chapter 2 we review the published works on the ADI-FDTD method including the theory, numerical dispersion error, dispersion error reduction, splitting error, accurate source

implementation, perfectly matched layer, higher-order schemes, non-Cartesian coordinates, practical applications, envelope scheme, and other unconditionally stable methods.

Chapter 3 covers the theory of ADI-FDTD method. Also, its unconditional stability and numerical dispersion relation are studied in this chapter. The numerical implementation of the ADI-FDTD method is demonstrated in chapter 4. Two numerical experiments are used to verify the accuracy of our developed code and one other experiment shows the practical application of the ADI-FDTD method.

In chapter 5 the theory of absorbing boundary conditions is discussed and specifically explains the Higdon's ABC. Implementation and stability of higher-order Higdon's ABCs in the ADI-FDTD method are studied in this chapter. The COM and its stability are also investigated in this chapter.

Chapter 6 provides the theory, performance, and analytical investigation of CDM. Also, implementing of the CDM in the ADI-FDTD method is introduced in this chapter. The conclusions and future work are provided in chapter 7.

Chapter 2 Literature Review of the ADI-FDTD

Method

Theory of the ADI-FDTD Method

The Alternating Direction Implicit (ADI) scheme for Finite-Difference Time-Domain (FDTD) method was first proposed in [2-1], and [2-2]. It was shown that this method is unconditionally stable both analytically and numerically even if the Courant-Friedrichs-Lewy (CFL) stability limit is violated. Therefore, this method is not restricted by the minimum cell size in the simulation domain. The Alternating Direction Implicit Finite-Difference Time-Domain (ADI-FDTD) method was extended to a full three-dimensional ADI-FDTD method in [2-3], and [2-4]. They showed the unconditional stability analytically and also verified it numerically for the three-dimensional domains. Also they compared the results with the conventional three-dimensional FDTD method and its accuracy was verified.

In [2-11], a generalized derivation of the ADI-FDTD method based on the operator splitting is proposed and its stability is proven. [2-6] investigates some fundamental characteristics of the ADI-FDTD method in one-dimensional cases. They have found that two sub-step methods alternates the dissipation and growth that exactly compensate each other.

Although it is always said that by using the ADI-FDTD method we can save time in comparison with the FDTD method for cases that have very fine structures, [2-5] discusses the true time saving of applying the ADI-FDTD method.

[2-5], [2-7], and [2-8] show how to apply dispersive materials (frequency dependent materials) into the ADI-FDTD method. In [2-32] the concept of DSP algorithms for digital filter design is used to introduce the frequency dependent property of media into the ADI-FDTD method.

Numerical Dispersion Error of the ADI-FDTD Method

Increasing the time-step size of the ADI-FDTD method over the CFL stability limit is the main feature of this method. Now the other question rises is how large the time-step can be made. The large numerical dispersion error created by the ADI-FDTD method is a drawback of the ADI-FDTD method and is a function of the time-step size. In [2-9]-[2-12], the numerical dispersion of the ADI-FDTD method is investigated and the dispersion relation is derived analytically. The effects of spatial and temporal steps on the numerical dispersion are also studied. They have found that the large time-step size results in high numerical dispersion. They have concluded that the time-step size of the ADI-FDTD method is limited by the required accuracy not by stability..

The inconsistency of different numerical dispersion relations of the ADI-FDTD method presented in different works is studied in [2-13]. They have re-derived the numerical dispersion relation by analysis of the amplification factor and verified it with numerical experiments.

Also an analytical relation of numerical dispersion for the two-dimensional ADI-FDTD method is proposed in [2-14]. By comparison with numerical experiments, they claim that their dispersion relation is the correct calculated relation for the two-dimensional ADI-FDTD method.

Dispersion Error Reduction in the ADI-FDTD Method

The previous section reviewed different papers that showed the numerical dispersion error is a drawback in the ADI-FDTD method. In this section we review different papers that introduce different methods to reduce the dispersion error.

In [2-15] a parameter optimized ADI-FDTD method is introduced to minimize the dispersion error for arbitrary incident angles and for different time-step sizes. It is also shown that this method is unconditionally stable if proper parameter values are chosen.

In [2-16] and [2-17] the dispersion error has been reduced by adding anisotropic parameters into the ADI-FDTD formulas. This idea is based on another work on the conventional FDTD method in which artificial anisotropy was introduced to reduce the numerical dispersion. The results show the improvement in dispersion error and for this method the computational overhead is also small.

A class of three-dimensional spatial/temporal operators to reduce the dispersion error for complex electromagnetic structures, e.g. circularly polarized slot-coupled microstrip and dielectric resonator antennas, is introduced in [2-18]. Their results show the reduction in dispersion error even when the time-step size surpasses the CFL stability limit.

Splitting Error, and Reducing Splitting Error in the ADI-FDTD Method

The ADI-FDTD method can be considered as the first iteration to solve the approximate Crank-Nicolson equations. Using this fact, different researchers have tried to decrease the splitting error in the ADI-FDTD method.

The closed form of the truncation error for the two-, and three-dimensional ADI-FDTD method is obtained in [2-19]. The dependence of the truncation error on the square of the time-step multiplied by the spatial derivatives of the field is found to be a unique feature of the ADI-FDTD method. As the time-step size increases, the truncation error term increases and the total accuracy decrease. For the time-step greatly exceeding the CFL stability limit, the Crank-Nicolson scheme shows excellent agreement with FDTD method results in case the ADI-FDTD method does not.

In [2-20] they have tried to use the computational efficiency of the ADI-FDTD method along with the accuracy of Crank-Nicolson FDTD method. Therefore, they have proposed the ADI-FDTD methods that are based on the CN-FDTD formulation but the computational efficiency is the same as the conventional ADI-FDTD method.

In [2-21]-[2-23] they have decreased the splitting error in the ADI-FDTD method by employing higher-order iterations. [2-22] also shows that the iterative ADI-FDTD method is convergent and the convergence rate depends on the CFL stability limit. In [2-23] as a way to save computational resources along with reducing the splitting error, they have only applied the iterative ADI-FDTD method to locations where there are large field variation, e.g. close to conductors, metallic tips, edges, corners, and near-field sources.

Accurate Source Implementation in the ADI-FDTD Method

The other issue of the ADI-FDTD method is source implementation. There may be small asymmetries in the field distribution if the source is not implemented correctly [2-24]-[2-26]. In [2-24] by considering the ADI-FDTD method as an

approximate factorization of the Crank-Nicolson scheme, they have proposed a new method to implement the current source that eliminates the asymmetry and makes the ADI-FDTD method more useful.

The current source condition is derived by starting with the Crank-Nicolson FDTD method and developing to the ADI-FDTD method in [2-16] and [2-17]. They have also illustrated that this new source implementation method is more accurate than the previous source implementation methods.

A new source implementation for the ADI-FDTD method which has no asymmetry up to the numerical noise level is presented in [2-26]. They have concluded that the source can be implemented most accurately if the excitation is directly incorporated within the tri-diagonal matrix and if the time discretization of source is done appropriately within each full time step.

Perfectly Matched Layer (PML) Implementation in the ADI-FDTD Method

PML is a versatile ABC which effectively absorbs any outgoing waves, from any direction and any frequency. Different methods are proposed in [2-27]-[2-32] to implement PML in the ADI-FDTD method. A split field PML medium is introduced in [2-27]. It is also demonstrated that the ADI-FDTD method remains unconditionally stable with the inclusion of PML.

A PML medium with complex frequency shifted constitutive parameters is introduced in [2-28]. The absorbing boundary is implemented using the convolutional PML (CPML). It is demonstrated that the resulting ADI-CPML method is unconditionally stable. The effectiveness of the absorbing medium as a function of the time-step is also demonstrated.

A novel implementation of the PML absorber for the ADI-FDTD method is proposed and implemented in [2-29]. They claim that compared to the conventional PML implementation, the performance of the proposed PML is more efficient for large Courant numbers.

In [2-30] the unconditionally stable formulations of the anisotropic PML (APML) are presented for truncating frequency-dependent media. The formulations are based on the auxiliary differential equation and ADI-FDTD methods.

Unsplit-field and unconditional stable formulations of the PML as truncating media for frequency dispersive first-order Debye media is presented in [2-31]. [2-32] presents the ADI formulations of the nearly perfectly matched layer (NPML) to be applied as absorbing boundary conditions.

High-Order ADI-FDTD Methods

The order of a method is defined based on the order of spatial difference. In [2-33], a fourth-order two-dimensional ADI-FDTD method is developed. The dispersion relation is derived and compared with the conventional two-dimensional ADI-FDTD method. They found that the higher-order two-dimensional ADI-FDTD method has a better accuracy compared to the conventional two-dimensional ADI-FDTD method. In [2-5] the same high-order spatial scheme is also proposed for the three-dimensional ADI-FDTD method and they showed that it slightly improves the associated dispersion error. Considering the complexity and required time for each updating procedure, they concluded that there is no benefit to overall performance compared with the conventional ADI-FDTD method.

In [2-34] an unconditionally stable higher-order ADI-FDTD method for analysis of curvilinear electromagnetic compatibility (EMC) applications is introduced. This method is based on a class of precise spatial/temporal nonstandard forms. They claim that this method suppresses the dispersion errors of the ordinary approach as the time-step increases and therefore can have very accurate results even far beyond the Courant limit.

A complete investigation of the dispersion error of higher-order three-dimensional ADI-FDTD method is provided in [2-35]. They derived the generalized form of the dispersion relations and showed as the higher-order ADI-FDTD method is used the results become more accurate. They also showed that all the higher-order ADI-FDTD methods that use center finite difference scheme are unconditionally stable.

ADI-FDTD Method in Non-Cartesian Co-ordinates

The ADI-FDTD method is modified to be applied in non-Cartesian co-ordinates in [2-36], [2-37], and [2-34]. It is also shown that the ADI-FDTD method in non-Cartesian co-ordinates is unconditionally stable and the time-step size is again restricted by accuracy rather than stability. There is an additional special treatment in [2-36] to overcome the singularity along the vertical axis of cylindrical co-ordinates.

ADI-FDTD Method Practical Applications

Employing the ADI-FDTD method for numerical experiments with very fine structures, e.g. structures with conducting strips, is efficient. The ADI-FDTD method is used to calculate the shielding effectiveness of various enclosures in [2-38]. The enclosures are composed of very thin conductive sheets, which are generally

fabricated using conductive paints or electro-less plating techniques on plastic surfaces. The ADI-FDTD method is used to derive the characteristics of typical and practical microstrip components such as microstrip linear resonators and microstrip low-pass filters [2-39]. These resonators and filters include very narrow gaps and strips which defend the usage of ADI-FDTD method. [2-40] also applies the ADI-FDTD method to conductive materials.

The ADI-FDTD method will be more practical if active and non-linear lumped devices can be included. In [2-41], an algorithm is introduced that could include active and non-linear lumped devices in the ADI-FDTD method. Also some corrections are made to the algorithm to eliminate the instability that occurs in this new algorithm.

The other useful application of ADI-FDTD method can be in periodic boundary conditions [2-42]. However, implementing the ADI-FDTD method in periodic boundary conditions results in a cyclic matrix that removes the simplicity of the tri-diagonal matrix solution. To avoid the complexity of inverting the cyclic matrix directly, the problem is divided into two auxiliary linear systems that can be solved by a tri-diagonal matrix solver. The number of required arithmetic operations will be of the same order as the conventional ADI-FDTD method and this new method keeps the computational efficiency of the ADI-FDTD method.

Envelope ADI-FDTD Method

The ADI-FDTD method can be modified to calculate the envelope rather than the fast-varying fields and as a result, errors can be minimized. This new method is called envelope ADI-FDTD method. The envelope ADI-FDTD method and

conventional ADI-FDTD methods use a cell size limited by the carrier wavelength, in case we are modeling a wave with a high carrier frequency and narrow bandwidth. But the time-step for the envelope ADI-FDTD method can be much larger than the time-step for the conventional ADI-FDTD method because it is simulating the wave envelope, which has a lower frequency.

The envelope ADI-FDTD method is applied in [2-43] because the conventional ADI-FDTD method can not be applied to simulating photonic devices if reasonable accuracy is to be kept. Using the envelope ADI-FDTD method, the simulation time was decreased by retaining the same level of accuracy compared with the conventional FDTD method.

The numerical characteristics of envelope ADI-FDTD method are studied in [2-44]. It is shown that the envelope ADI-FDTD method is unconditionally stable, and dispersion accuracy is better than the conventional ADI-FDTD method. Therefore, it can be used as an efficient electromagnetic analysis tool especially in single frequency or band limited systems.

The problem of instability in implementing the PML in the envelope ADI-FDTD method is studied in [2-45] and is improved by making changes to the Berenger's original split-field perfectly-matched layer equations. As the ADI scheme in time, the alternating characteristic was applied in the split-field PML formulation for the envelope ADI-FDTD method.

Numerical properties of three-dimensional envelope ADI-FDTD method are investigated in [2-46]. The variations of dispersion errors with the propagation direction, ratio of carrier to envelope frequencies, and spatial and temporal steps are

studied. They have found that the envelope ADI-FDTD method has a better accuracy than the conventional ADI-FDTD method for simulations with a high ratio of carrier to envelope frequencies.

In [2-47], they have studied the phase velocity error of a propagating Gaussian pulse for the envelope ADI-FDTD and conventional ADI-FDTD methods. The simulation results show the better performance of the envelope ADI-FDTD method over the ADI-FDTD method in numerical accuracy.

Other Unconditionally Stable Methods

[2-48] presents an unconditionally stable FDTD method based on a D-H formulation and the recently proposed ADI marching scheme. The advantage of the D-H algorithm over the conventional E-H is the possibility to easily implement an unsplit field components formulation of the PML ABC that is independent from the background material used in the FDTD grid. The method, therefore, allows immersing any dielectric in the PML layers without any special consideration, and is amenable for model truncation often used in biomedical simulations. Furthermore, the proposed scheme can be extended to account for frequency dispersive dielectrics.

In [2-49], an ADI technique is applied to the recently developed multiresolution time-domain (MRTD) method, resulting in an unconditionally stable ADI-MRTD method free of the CFL stability limit. The unconditional stability is theoretically proved. Its time-step is determined only by modeling accuracy. The price for having unconditional stability is, however, that the required computation memory becomes almost twice of that for the original MRTD.

A hybrid two-dimensional subgridding scheme, based on a combination of the FDTD and ADI-FDTD methods, is utilized in [2-50]. The ADI-FDTD method is used for a fine grid in the vicinity of metallic etches, while the coarse FDTD grid is used outside this region. The advantage of the ADI-FDTD method is that it can be synchronized with the time marching step employed in the coarse FDTD method, obviating the need for the temporal interpolation of the fields in the process. This helps to render the hybrid ADI-FDTD subgridding scheme more efficient than the conventional FDTD subgridding algorithm in terms of the run time.

Another accurate and efficient unconditionally stable FDTD (US-FDTD) method is proposed in [2-50]. The two key points of the proposed US-FDTD method are: defining the field components at only n and $(n+1)$ time-steps; and arranging the left and right hands of the original updating equations to be as accurate (in respect of time) as possible.

In [2-52], the two unconditionally stable techniques, the ADI and the split-step (SS) schemes, are developed for the pseudo-spectral time-domain (PSTD) algorithm to maintain stability while achieving higher accuracy and efficiency over the FDTD method. The multi-domain strategy is employed to allow for a flexible treatment of internal inhomogeneities.

Two implicit FDTD methods for two-dimensional TE_z wave are proposed in [2-50]. The Approximate-Decoupling Method solves two tri-diagonal matrices and computes only one explicit equation for a full update cycle. The numerical dispersion relation is the same as the conventional ADI-FDTD method. The Cycle-Sweep Method solves two tri-diagonal matrices, and computes two equations explicitly for a

full update cycle. To compare these two methods the cycle-sweep method has much smaller numerical anisotropy than the approximate-decoupling method. The dispersion error is the same along the axes, and larger along the 45° diagonal than the conventional ADI-FDTD method. These methods are strictly non-dissipative and unconditionally stable.

The Crank-Nicolson Approximate-Factorization-Splitting (CNAFS) method, which can be used as an efficient implementation of the Crank-Nicolson method for solving the three-dimensional Maxwell's equations in the time-domain, is presented in [2-54]. This method is unconditionally stable and solves tri-diagonal matrices instead of solving a huge sparse matrix.

[2-55] presents a split-step FDTD method with high-order spatial accuracy. This method is unconditionally stable.

By using piecewise linear JE recursive convolution (PLJERC), the ADI-FDTD method is extended for dispersive media-isotropic plasma in [2-56]

In [2-57], they have proposed a two-dimensional LOD (locally one dimensional)-FDTD which is unconditionally stable. Its solution needs two implicit and two explicit equations in comparison with the conventional ADI-FDTD method which needs two implicit and four explicit equations.

In [2-58], they have modified the recently proposed unconditionally stable D-H ADI-FDTD method which considerably reduces the late-time error induced by the corner cells. An optimal choice of the PML conductivity profile coefficients is also proposed in this work.

Chapter 3 Theory of ADI-FDTD Method

The Maxwell's curl equations for an isotropic medium with permittivity of ε and permeability of μ are

$$\nabla \times H = \varepsilon \frac{\partial E}{\partial t} \quad (3-1)$$

$$\nabla \times E = -\mu \frac{\partial H}{\partial t} \quad (3-2)$$

Each of these two equations can be cast into three scalar partial differential equations in the Cartesian coordinates.

$$\frac{\partial E_x}{\partial t} = \frac{1}{\varepsilon} \left(\frac{\partial H_z}{\partial y} - \frac{\partial H_y}{\partial z} \right) \quad (3-3a)$$

$$\frac{\partial E_y}{\partial t} = \frac{1}{\varepsilon} \left(\frac{\partial H_x}{\partial z} - \frac{\partial H_z}{\partial x} \right) \quad (3-3b)$$

$$\frac{\partial E_z}{\partial t} = \frac{1}{\varepsilon} \left(\frac{\partial H_y}{\partial x} - \frac{\partial H_x}{\partial y} \right) \quad (3-3c)$$

$$\frac{\partial H_x}{\partial t} = \frac{1}{\mu} \left(\frac{\partial E_y}{\partial z} - \frac{\partial E_z}{\partial y} \right) \quad (3-4a)$$

$$\frac{\partial H_y}{\partial t} = \frac{1}{\mu} \left(\frac{\partial E_z}{\partial x} - \frac{\partial E_x}{\partial z} \right) \quad (3-4b)$$

$$\frac{\partial H_z}{\partial t} = \frac{1}{\mu} \left(\frac{\partial E_x}{\partial y} - \frac{\partial E_y}{\partial x} \right) \quad (3-4c)$$

Each field component $F_\alpha(t,x,y,z)$ can be denoted as $F_\alpha^n_{i,j,k} = F_\alpha(n\Delta t, i\Delta x, j\Delta y, k\Delta z)$ in discrete space and time, where $\alpha = x, y, \text{ or } z$; n is the time index; $i, j, \text{ and } k$ are space indexes; Δt is the time-step; and $\Delta x, \Delta y, \text{ and } \Delta z$ are spatial steps along the x -, y -, and z -directions, respectively.

In the Alternating Direction Implicit Finite-Difference Time-Domain (ADI-FDTD) method, electromagnetic-field components are arranged on the grid in the same way as the conventional FDTD method. Applying the ADI scheme requires updating the electric and magnetic fields from time step n to $n+1$ through two procedures. In the first procedure the fields advance from the n^{th} time step to $(n+1/2)^{th}$ time step; in the second procedure the fields advance from the $(n+1/2)^{th}$ time step to $(n+1)^{th}$ time step. The second requirement of the ADI scheme is applying the alternating direction implicit concept in implementation of finite difference approximations. In the first procedure, the first derivatives on the right hand side of equations (3-3) and (3-4) are replaced with the implicit finite difference approximations and the second derivatives are replaced with the explicit finite difference approximations. Therefore, the updating equations will be

First procedure:

$$\frac{E_x|_{i+1/2,j,k}^{n+1/2} - E_x|_{i+1/2,j,k}^n}{\Delta t/2} = \frac{1}{\epsilon} \left[\frac{H_z|_{i+1/2,j+1/2,k}^{n+1/2} - H_z|_{i+1/2,j-1/2,k}^{n+1/2}}{\Delta y} - \frac{H_y|_{i+1/2,j,k+1/2}^n - H_y|_{i+1/2,j,k-1/2}^n}{\Delta z} \right] \quad (3-5a)$$

$$\frac{E_y|_{i,j+1/2,k}^{n+1/2} - E_y|_{i,j+1/2,k}^n}{\Delta t/2} = \frac{1}{\epsilon} \left[\frac{H_x|_{i,j+1/2,k+1/2}^{n+1/2} - H_x|_{i,j+1/2,k-1/2}^{n+1/2}}{\Delta z} - \frac{H_z|_{i+1/2,j+1/2,k}^n - H_z|_{i-1/2,j+1/2,k}^n}{\Delta x} \right] \quad (3-5b)$$

$$\frac{E_z|_{i,j,k+1/2}^{n+1/2} - E_z|_{i,j,k+1/2}^n}{\Delta t/2} = \frac{1}{\varepsilon} \left[\frac{H_y|_{i+1/2,j,k+1/2}^{n+1/2} - H_y|_{i-1/2,j,k+1/2}^{n+1/2}}{\Delta x} - \frac{H_x|_{i,j+1/2,k+1/2}^n - H_x|_{i,j-1/2,k+1/2}^n}{\Delta y} \right] \quad (3-5c)$$

$$\frac{H_x|_{i,j+1/2,k+1/2}^{n+1/2} - H_x|_{i,j+1/2,k+1/2}^n}{\Delta t/2} = \frac{1}{\mu} \left[\frac{E_y|_{i,j+1/2,k+1}^{n+1/2} - E_y|_{i,j+1/2,k}^{n+1/2}}{\Delta z} - \frac{E_z|_{i,j+1,k+1/2}^n - E_z|_{i,j,k+1/2}^n}{\Delta y} \right] \quad (3-6a)$$

$$\frac{H_y|_{i+1/2,j,k+1/2}^{n+1/2} - H_y|_{i+1/2,j,k+1/2}^n}{\Delta t/2} = \frac{1}{\mu} \left[\frac{E_z|_{i+1,j,k+1/2}^{n+1/2} - E_z|_{i,j,k+1/2}^{n+1/2}}{\Delta x} - \frac{E_x|_{i+1/2,j,k+1}^n - E_x|_{i+1/2,j,k}^n}{\Delta z} \right] \quad (3-6b)$$

$$\frac{H_z|_{i+1/2,j+1/2,k}^{n+1/2} - H_z|_{i+1/2,j+1/2,k}^n}{\Delta t/2} = \frac{1}{\mu} \left[\frac{E_x|_{i+1/2,j+1,k}^{n+1/2} - E_x|_{i+1/2,j,k}^{n+1/2}}{\Delta y} - \frac{E_y|_{i+1,j+1/2,k}^n - E_y|_{i,j+1/2,k}^n}{\Delta x} \right] \quad (3-6c)$$

Calculating the electric fields at time step $n+1/2$ needs the values of magnetic fields, which are not computed yet. To address this problem, the equation for calculating $E_x|_{i+1/2,j,k}^{n+1/2}$ is modified by replacing (3-6c) in (3-5a) which results in

$$\begin{aligned} & -\left(\frac{\Delta t^2}{4\mu\varepsilon\Delta y^2}\right)E_x|_{i+1/2,j+1,k}^{n+1/2} + \left(1 + \frac{\Delta t^2}{2\mu\varepsilon\Delta y^2}\right)E_x|_{i+1/2,j,k}^{n+1/2} - \left(\frac{\Delta t^2}{4\mu\varepsilon\Delta y^2}\right)E_x|_{i+1/2,j-1,k}^{n+1/2} = \\ & E_x|_{i+1/2,j,k}^n + \frac{\Delta t}{2\varepsilon\Delta y} \left(H_z|_{i+1/2,j+1/2,k}^n - H_z|_{i+1/2,j-1/2,k}^n \right) \\ & - \frac{\Delta t}{2\varepsilon\Delta z} \left(H_y|_{i+1/2,j,k+1/2}^n - H_z|_{i+1/2,j,k-1/2}^n \right) \\ & - \frac{\Delta t^2}{4\mu\varepsilon\Delta y\Delta x} \left(E_y|_{i+1,j+1/2,k}^n - E_y|_{i,j+1/2,k}^n - E_y|_{i+1,j-1/2,k}^n + E_y|_{i,j-1/2,k}^n \right) \end{aligned} \quad (3-7)$$

The same procedure should be used to obtain the updating equations of other components of the electric field.

In the second procedure, the first derivatives on the right hand side of equations (3-3) and (3-4) are replaced with the explicit finite difference approximations and the second derivatives are replaced with the implicit finite difference approximations. Therefore, the updating equations will be

Second procedure:

$$\frac{E_x|_{i+1/2,j,k}^{n+1} - E_x|_{i+1/2,j,k}^{n+1/2}}{\Delta t/2} = \frac{1}{\varepsilon} \left[\frac{H_z|_{i+1/2,j+1/2,k}^{n+1/2} - H_z|_{i+1/2,j-1/2,k}^{n+1/2}}{\Delta y} - \frac{H_y|_{i+1/2,j,k+1/2}^{n+1} - H_y|_{i+1/2,j,k-1/2}^{n+1}}{\Delta z} \right] \quad (3-8a)$$

$$\frac{E_y|_{i,j+1/2,k}^{n+1} - E_y|_{i,j+1/2,k}^{n+1/2}}{\Delta t/2} = \frac{1}{\varepsilon} \left[\frac{H_x|_{i,j+1/2,k+1/2}^{n+1/2} - H_x|_{i,j+1/2,k-1/2}^{n+1/2}}{\Delta z} - \frac{H_z|_{i+1/2,j+1/2,k}^{n+1} - H_z|_{i-1/2,j+1/2,k}^{n+1}}{\Delta x} \right] \quad (3-8b)$$

$$\frac{E_z|_{i,j,k+1/2}^{n+1} - E_z|_{i,j,k+1/2}^{n+1/2}}{\Delta t/2} = \frac{1}{\varepsilon} \left[\frac{H_y|_{i+1/2,j,k+1/2}^{n+1/2} - H_y|_{i-1/2,j,k+1/2}^{n+1/2}}{\Delta x} - \frac{H_x|_{i,j+1/2,k+1/2}^{n+1} - H_x|_{i,j-1/2,k+1/2}^{n+1}}{\Delta y} \right] \quad (3-8c)$$

$$\frac{H_x|_{i,j+1/2,k+1/2}^{n+1} - H_x|_{i,j+1/2,k+1/2}^{n+1/2}}{\Delta t/2} = \frac{1}{\mu} \left[\frac{E_y|_{i,j+1/2,k+1}^{n+1/2} - E_y|_{i,j+1/2,k}^{n+1/2}}{\Delta z} - \frac{E_z|_{i,j+1,k+1/2}^{n+1} - E_z|_{i,j,k+1/2}^{n+1}}{\Delta y} \right] \quad (3-9a)$$

$$\frac{H_y|_{i+1/2,j,k+1/2}^{n+1} - H_y|_{i+1/2,j,k+1/2}^{n+1/2}}{\Delta t/2} = \frac{1}{\mu} \left[\frac{E_z|_{i+1,j,k+1/2}^{n+1/2} - E_z|_{i,j,k+1/2}^{n+1/2}}{\Delta x} - \frac{E_x|_{i+1/2,j,k+1}^{n+1} - E_x|_{i+1/2,j,k}^{n+1}}{\Delta z} \right] \quad (3-9b)$$

$$\frac{H_z|_{i+1/2,j+1/2,k}^{n+1} - H_z|_{i+1/2,j+1/2,k}^{n+1/2}}{\Delta t/2} = \frac{1}{\mu} \left[\frac{E_x|_{i+1/2,j+1,k}^{n+1/2} - E_x|_{i+1/2,j,k}^{n+1/2}}{\Delta y} - \frac{E_y|_{i+1,j+1/2,k}^{n+1} - E_y|_{i,j+1/2,k}^{n+1}}{\Delta x} \right] \quad (3-9c)$$

Similar to the first procedure, the updating equations of the electric fields of the second procedure must be modified. The updating equations of the magnetic fields are not modified because the required electric fields are already calculated.

3.1 Stability of the ADI-FDTD Method

For a recursive system of form

$$X^{n+1} = \Lambda X^n \quad (3.1-1)$$

the Fourier method can be used to determine its numerical stability [3-1]. In this method, instantaneous values of the electric and magnetic fields are first Fourier-transformed into spatial spectral domain waves, representing a spectrum of spatial sinusoidal modes. Second, the location of eigenvalues of Λ are checked; if all of them lie inside or on the perimeter of the unit circle, the system is defined as stable, otherwise the system is unstable.

Assuming the spatial frequencies to be k_x , k_y , and k_z along the x , y , and z directions, the field components in the spatial spectral domain can be written as

$$E_x \Big|_{i+1/2, j, k}^n = E_x^n e^{-j(k_x(i+1/2)\Delta x + k_y j\Delta y + k_z k\Delta z)} \quad (3.1-2a)$$

$$E_y \Big|_{i, j+1/2, k}^n = E_y^n e^{-j(k_x i\Delta x + k_y(j+1/2)\Delta y + k_z k\Delta z)} \quad (3.1-2b)$$

$$E_z \Big|_{i, j, k+1/2}^n = E_z^n e^{-j(k_x i\Delta x + k_y j\Delta y + k_z(k+1/2)\Delta z)} \quad (3.1-2c)$$

$$H_x \Big|_{i, j+1/2, k+1/2}^n = H_x^n e^{-j(k_x i\Delta x + k_y(j+1/2)\Delta y + k_z(k+1/2)\Delta z)} \quad (3.1-2d)$$

$$H_y \Big|_{i+1/2, j, k+1/2}^n = H_y^n e^{-j(k_x(i+1/2)\Delta x + k_y j\Delta y + k_z(k+1/2)\Delta z)} \quad (3.1-2e)$$

$$H_z \Big|_{i+1/2, j+1/2, k}^n = H_z^n e^{-j(k_x(i+1/2)\Delta x + k_y(j+1/2)\Delta y + k_z k\Delta z)} \quad (3.1-2f)$$

We denote the field vector in the spatial spectral domain as

$$X^n = \begin{bmatrix} E_x^n \\ E_y^n \\ E_z^n \\ H_x^n \\ H_y^n \\ H_z^n \end{bmatrix} \quad (3.1-3)$$

Substituting of (3.1-2) in (3-5)-(3-6) and (3-8)-(3-9), after some manipulation,

Λ in (3.1-1) can be written as [3-2]

$$\Lambda = \begin{bmatrix} \frac{A_1+B_1}{Q_x Q_y Q_z} & \frac{2\mu\epsilon W_x W_y}{Q_x Q_y} & \frac{2\mu\epsilon W_x W_z}{Q_y Q_z} & \frac{-2j\mu W}{Q_x Q_y} & \frac{2j\mu^2 \epsilon W_z}{Q_y Q_z} & \frac{2j\mu D_1}{Q_x Q_y Q_z} \\ \frac{2\mu\epsilon W_y W_x}{Q_z Q_x} & \frac{A_2+B_2}{Q_x Q_y Q_z} & \frac{2\mu\epsilon W_y W_z}{Q_y Q_z} & \frac{2j\mu D_2}{Q_y Q_z} & \frac{-2j\mu W}{Q_y Q_z} & \frac{2j\mu^2 \epsilon W_x}{Q_z Q_x} \\ \frac{2\mu\epsilon W_z W_x}{Q_z Q_x} & \frac{2\mu\epsilon W_z W_y}{Q_x Q_y} & \frac{A_3+B_3}{Q_y Q_z} & \frac{2j\mu^2 \epsilon W_y}{Q_x Q_y} & \frac{2j\mu D_3}{Q_y Q_z} & \frac{-2j\mu W}{Q_z Q_x} \\ \frac{-2j\epsilon W}{Q_x Q_z} & \frac{2j\epsilon D_2}{Q_x Q_y Q_z} & \frac{2j\mu\epsilon^2 W_y}{Q_y Q_z} & \frac{A_1+B_3}{Q_x Q_y Q_z} & \frac{2\mu\epsilon W_x W_y}{Q_y Q_z} & \frac{2\mu\epsilon W_z W_x}{Q_z Q_x} \\ \frac{2j\mu\epsilon^2 W_z}{Q_z Q_x} & \frac{-2j\epsilon W}{Q_x Q_y Q_z} & \frac{2j\epsilon D_3}{Q_y Q_z} & \frac{2\mu\epsilon W_x W_y}{Q_x Q_y Q_z} & \frac{A_2+B_1}{Q_y Q_z} & \frac{2\mu\epsilon W_y W_z}{Q_z Q_x} \\ \frac{2j\epsilon D_1}{Q_x Q_y Q_z} & \frac{2j\mu\epsilon^2 W_x}{Q_y Q_x} & \frac{-2j\epsilon W}{Q_x Q_y Q_z} & \frac{2\mu\epsilon W_z W_x}{Q_x Q_y} & \frac{2\mu\epsilon W_y W_z}{Q_x Q_y Q_z} & \frac{A_3+B_2}{Q_z Q_x} \\ \frac{Q_x Q_y Q_z}{Q_x Q_y Q_z} & \frac{Q_x Q_y}{Q_x Q_y} & \frac{Q_z Q_y}{Q_z Q_y} & \frac{Q_x Q_y}{Q_x Q_y} & \frac{Q_y Q_z}{Q_y Q_z} & \frac{Q_x Q_y Q_z}{Q_x Q_y Q_z} \end{bmatrix} \quad (3.1-4)$$

where

$$W_\alpha = \frac{\Delta t}{\Delta \alpha} \sin\left(\frac{k_\alpha \Delta \alpha}{2}\right), \quad \alpha = x, y, z$$

$$Q_\alpha = 1 + \frac{W_\alpha^2}{\mu\epsilon}, \quad \alpha = x, y, z$$

$$W = W_x W_y W_z$$

$$A_1 = \mu^3 \epsilon^3 + \mu^2 \epsilon^2 (W_x^2 - W_y^2 - W_z^2) + W_x^2 W_y^2 W_z^2$$

$$A_2 = \mu^3 \epsilon^3 + \mu^2 \epsilon^2 (W_y^2 - W_z^2 - W_x^2) + W_x^2 W_y^2 W_z^2$$

$$A_3 = \mu^3 \epsilon^3 + \mu^2 \epsilon^2 (W_z^2 - W_x^2 - W_y^2) + W_x^2 W_y^2 W_z^2$$

$$B_1 = \mu\epsilon (W_x^2 W_y^2 - W_y^2 W_z^2 - W_z^2 W_x^2)$$

$$B_2 = \mu\epsilon (W_y^2 W_z^2 - W_z^2 W_x^2 - W_x^2 W_y^2)$$

$$B_3 = \mu\epsilon (W_z^2 W_x^2 - W_x^2 W_y^2 - W_y^2 W_z^2)$$

$$D_1 = W_y (W_x^2 W_z^2 - \mu^2 \epsilon^2)$$

$$D_2 = W_z (W_y^2 W_x^2 - \mu^2 \epsilon^2)$$

$$D_3 = W_x(W_z^2 W_y^2 - \mu^2 \varepsilon^2)$$

The eigenvalues of Λ can be found [3-2]

$$\lambda_1 = \lambda_2 = 1$$

$$\lambda_3 = \lambda_5 = \frac{\sqrt{R^2 - S^2} + jS}{R} \quad (3.1-5)$$

$$\lambda_4 = \lambda_6 = \lambda_3^* = \frac{\sqrt{R^2 - S^2} - jS}{R}$$

where

$$R = (\mu\varepsilon + W_x^2)(\mu\varepsilon + W_y^2)(\mu\varepsilon + W_z^2)$$

$$S = \sqrt{4\mu\varepsilon(\mu\varepsilon W_x^2 + \mu\varepsilon W_y^2 + \mu\varepsilon W_z^2 + W_x^2 W_y^2 + W_y^2 W_z^2 + W_z^2 W_x^2)(\mu^3 \varepsilon^3 + W_x^2 W_y^2 W_z^2)}$$

The first two eigenvalues obviously have a magnitude of unity. The other four eigenvalues also have magnitudes of unity. This is because $R \geq S$ and the square roots in the numerator of the expressions for λ_3 , λ_4 , λ_5 , and λ_6 become real numbers. Therefore, the ADI-FDTD method is unconditionally stable regardless of the time-step size Δt .

3.2 Numerical Dispersion Relation of the ADI-FDTD Method

To calculate the numerical dispersion relation of the ADI-FDTD method, we assume the fields to be monochromatic waves with an angular frequency of ω

$$E_\alpha^n = E_\alpha e^{j\omega n \Delta t}, \quad \alpha = x, y, z \quad (3.2-1a)$$

$$H_\alpha^n = H_\alpha e^{j\omega n \Delta t}, \quad \alpha = x, y, z \quad (3.2-1b)$$

Replacing (3.2-1) in (3.1-1) results in

$$(e^{j\omega \Delta t} I - \Lambda)X = 0 \quad (3.2-2)$$

To find a nontrivial solution of (3.2-2), the determinant of the coefficient matrix should be zero

$$\det(e^{j\omega\Delta t} I - \Lambda) = 0 \quad (3.2-3)$$

which by substituting (3.1-4) in (3.2-3) the numerical dispersion relation of ADI-FDTD method is [3-3]

$$\sin^2(\omega \Delta t) = \frac{4\mu\varepsilon(\mu\varepsilon W_x^2 + \mu\varepsilon W_y^2 + \mu\varepsilon W_z^2 + W_x^2 W_y^2 + W_y^2 W_z^2 + W_z^2 W_x^2)(\mu^3 \varepsilon^3 + W_x^2 W_y^2 W_z^2)}{(\mu\varepsilon + W_x^2)^2 (\mu\varepsilon + W_y^2)^2 (\mu\varepsilon + W_z^2)^2} \quad (3.2-4)$$

Chapter 4 Numerical Implementation of the ADI-FDTD Method

In order to verify the accuracy of our Alternating Direction Implicit Finite-Difference Time-Domain (ADI-FDTD) code, we perform two numerical experiments and compare the simulation results to the analytical results and simulation results of other established methods or commercial codes. The third numerical experiment demonstrates a practical application of our code.

4.1 Code Verification: Resonant Frequency of Cavity

The first experiment calculates the resonant frequencies of a cavity. The cavity has dimensions of $9\text{mm} \times 6\text{mm} \times 15\text{mm}$ [4-1]. A uniform grid with grid size of $\Delta = 0.6\text{mm}$ is used to discretize the domain (Fig. 4.1-1). The maximum time-step size of the FDTD method is $\Delta t_{\text{FDTD}} = 1.15\text{ps}$ and we use the same time-step size for the ADI-FDTD method ($\Delta t_{\text{ADI-FDTD}} = \Delta t_{\text{FDTD}}$).

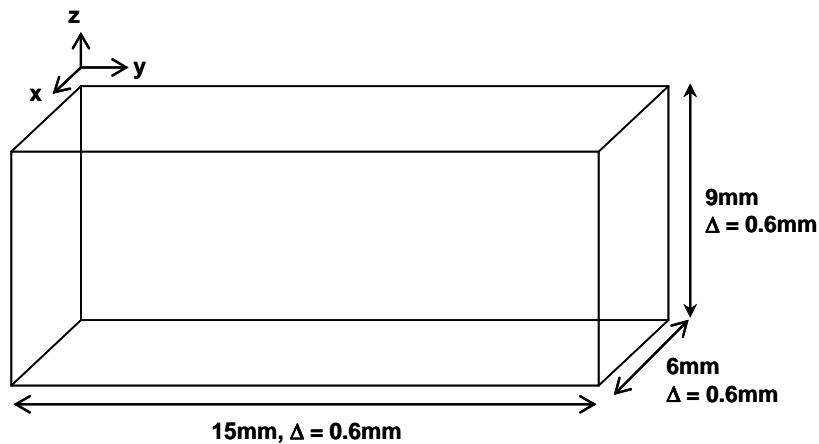


Fig. 4.1-1 Dimensions and grid size of cavity.

The calculated resonant frequencies of the first five modes are shown in Table 4.1-1. The results have been compared with the calculated resonant frequencies using the theory, HFSS software, and the FDTD method. As we see, the ADI-FDTD method gives the same order of errors as the HFSS and FDTD method.

Table 4.1-1 Comparing the calculated resonant frequencies of cavity using HFSS, FDTD, ADI-FDTD, and theory.

Theory (GHz)	HFSS (GHz)	Error (%)	FDTD (GHz)	Error (%)	ADI-FDTD (GHz)	Error (%)
19.433	19.42	0.06	19.44	0.03	19.44	0.03
26.034	26.00	0.13	25.99	0.17	25.99	0.17
26.926	26.89	0.13	26.83	0.35	26.83	0.35
30.046	30.00	0.15	30.10	0.18	29.79	0.85
31.667	31.60	0.21	31.90	0.74	31.69	0.07

Fig. 4.1-2 demonstrates the errors of the first resonant frequency calculated using different time-step sizes which exceed the Courant stability limit.

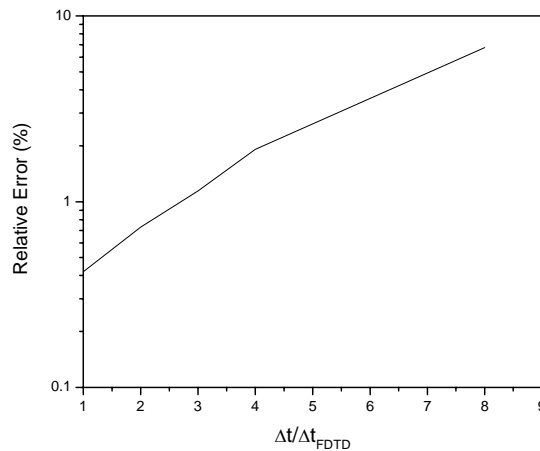


Fig. 4.1-2 Relative errors of the calculated resonant frequencies vs. time-step size.

4.2 Code Verification: Free Space Wave Propagation

This experiment demonstrates the wave propagation in the three-dimensional free space. The simulation domain is a box with dimensions of $12.5\text{mm} \times 12.5\text{mm} \times 12.5\text{mm}$ with grid size of $\Delta = 0.25\text{mm}$. The source is positioned at $(6.25\text{mm}, 6.25\text{mm}, 6.25\text{mm})$ and the monitor point is selected at $(6.25\text{mm}, 7.5\text{mm}, 6.25\text{mm})$ (Fig. 4.1-2). The excitation is a Gaussian pulse

$$f(t) = \exp\left(-\frac{(t-t_d)^2}{\tau^2}\right)$$

with $t_d = 80\text{ps}$ and $\tau = 20\text{ps}$. The 3dB bandwidth of a Gaussian pulse is $f_{-3\text{dB}} = 1/\pi\tau$, which for $\tau = 20\text{ps}$ results in $f_{-3\text{dB}} = 15.9\text{GHz}$ with the wavelength of $\lambda_{-3\text{dB}} = 18.84\text{mm}$. Therefore, the grid size of $\Delta = 0.25\text{mm}$ results in 75 points per wavelength which is much more than the proposed 10 points per wavelength for acceptable dispersion error [4-2].

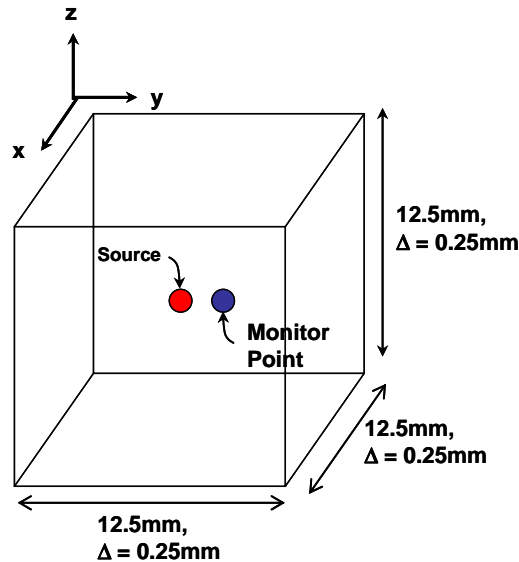


Fig. 4.2-1 Structure of the three-dimensional open-region simulation and the locations of source and monitor points.

A comparison of the recorded values of e_x at monitor points is shown in Fig. 4.2-2. As we see in the Fig. 4.2-2, the simulated electric fields using the ADI-FDTD and FDTD methods are exactly the same.

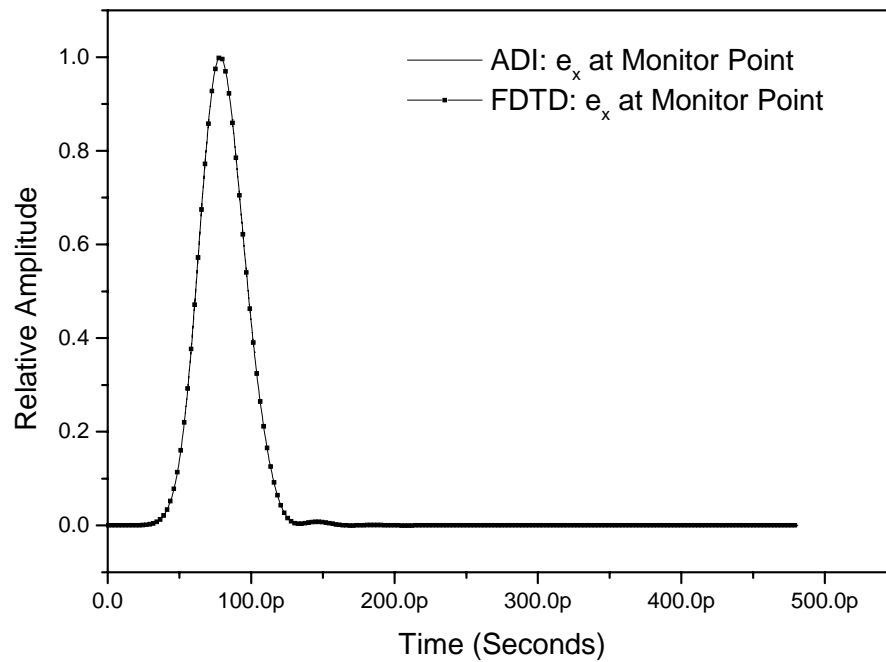


Fig. 4.2-2 Values of e_x calculated using the ADI-FDTD (solid line) and FDTD methods (solid line with squares).

4.3 Antenna Application

In this section, the ADI-FDTD method is applied for a practical application. The application considered is a microstrip-fed rectangular patch antenna similar to [4-

3]. The frequency range of interest is from DC to 20 GHz and the scattering parameters are also measured up to 20 GHz [4-3].

The dimensions of patch antenna are shown in Fig. 4.3-1. The approximate resonant frequency can be calculated using the fact $\lambda/2 \cong 12.45\text{mm}$. This antenna is built on Duroid substrate with $\epsilon_r=2.2$ and thickness of $1/32''$ (0.794mm).

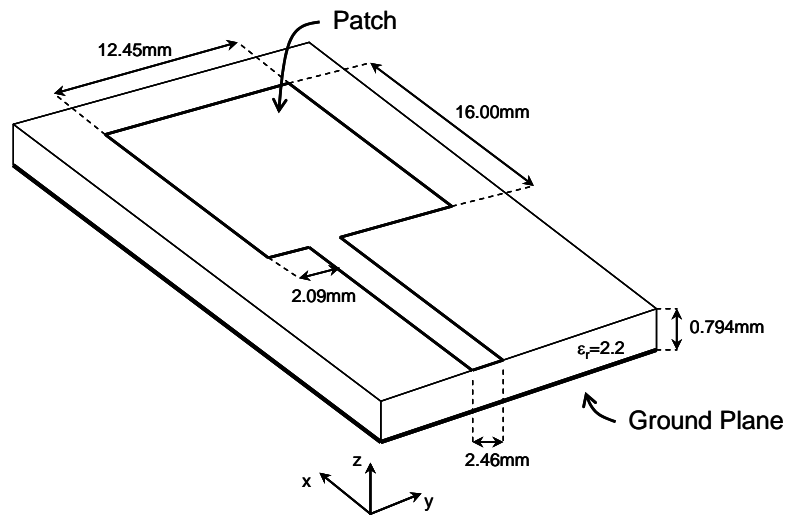


Fig. 4.3-1 Dimensions of patch antenna.

The source plane is a rectangle in the yz plane with the same width as the trace and the same height as the substrate (Fig. 4.3-2). The excitation is a Gaussian pulse

$$f(t) = \exp\left(-\left(\frac{t-t_0}{\tau}\right)^2\right)$$

where $t_0=45\text{ ps}$ and $\tau=15\text{ ps}$.

The simulation domain is terminated by the first order Mur's Absorbing Boundary Conditions (ABC) on 5 sides and only the plane $z=0$ is defined as perfect electric conductor (ground plane of the antenna). The ABC surfaces are several cells

away from the perimeters of antenna and we have considered a greater number of cells in the z -direction above the antenna plane to model the free space above the antenna. Notice that the ABC in the yz plane has been implemented several nodes away from the source plane to eliminate any undesirable effects.

The grid sizes in the x , y , and z directions are $\Delta x = 0.389mm$, $\Delta y = 0.4mm$, and $\Delta z = 0.265mm$. The total number of cells in the x -, y -, and z -directions are 60 , 100 , and 16 , respectively, and the rectangular patch is $32\Delta x \times 40\Delta y$ (Fig. 4.3-2). The cell arrangement in the z -direction is shown in Fig. 4.3-3 (a).

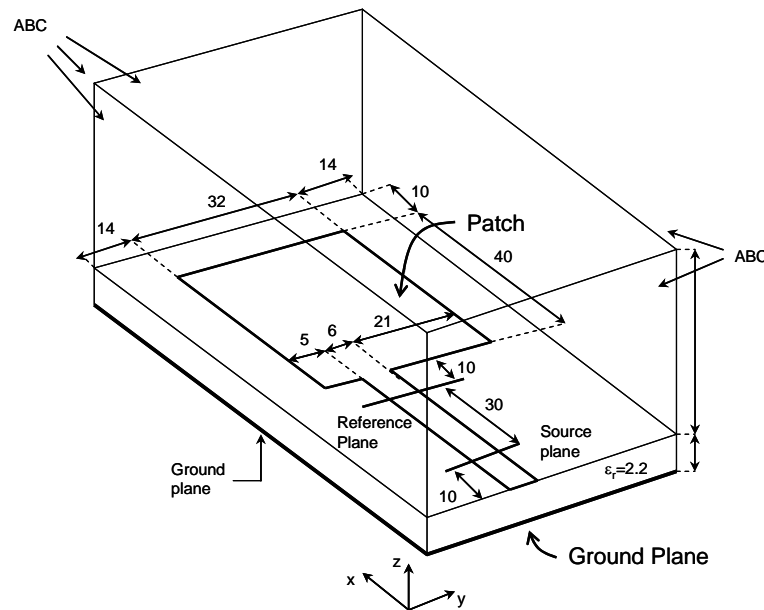


Fig. 4.3-2 Structure simulated by the ADI-FDTD method.

The time-step size is set at the CFL stability limit which is $\Delta t = 0.6403ps$. The reference plane, where the voltage is calculated, is set 10 cells away from the patch antenna. The length of microstrip line from the source to the antenna is $40\Delta y$. To calculate S_{11} , first we consider a long microstrip line, apply the excitation and record the voltage at the reference plane (V_{in}). Next, we excite the microstrip line connected

to antenna and record the voltage (V_{total}). S_{11} , which is defined as the reflected voltage to the incident voltage, is $S_{11} = V_{ref}/V_{in} = (V_{total} - V_{in})/V_{in}$ ($V_{total} = V_{in} + V_{ref}$).

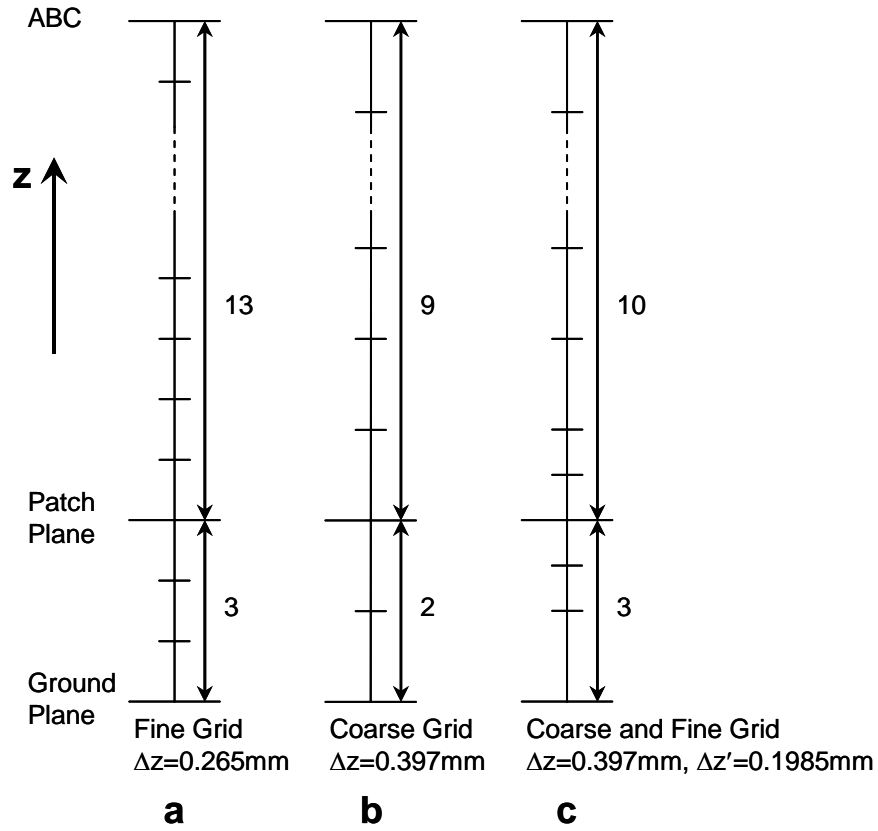


Fig. 4.3-3 Structure of grids in the z-direction.

The calculated scattering parameters are shown in Fig. 4.3-4. The first resonant frequency is $f_c = 7.4624\text{ GHz}$ and is shown in Table 4.3-1.

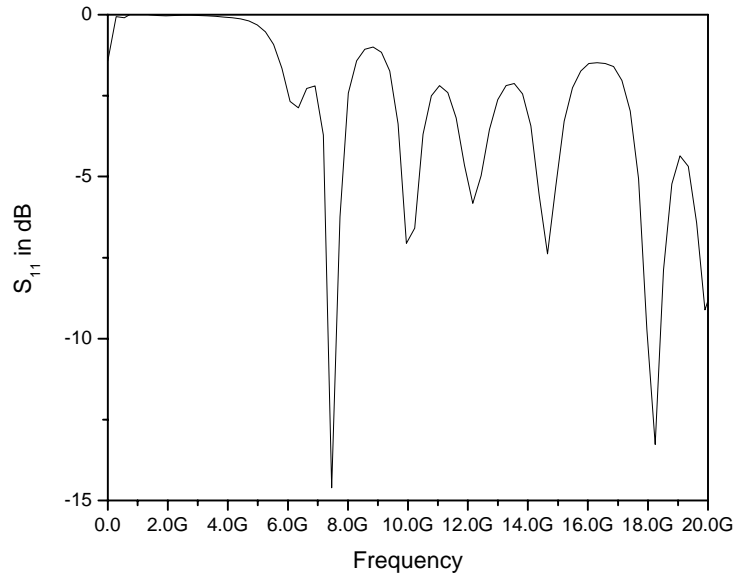


Fig. 4.3-4 S_{11} in dB for fine grid (Fig. 4.3-3 a).

In next simulation we only increase the grid size in the z -direction to $\Delta z = 0.397mm$ and the other parameters are left unchanged (Fig. 4.3-3 b). The time-step size is set at the CFL stability limit which is $\Delta t = 0.7606ps$. The scattering parameters are calculated and shown in Fig. 4.3-5. The first calculated resonant frequency is $f_c = 7.5484 GHz$ and is shown in Table 4.3-1.

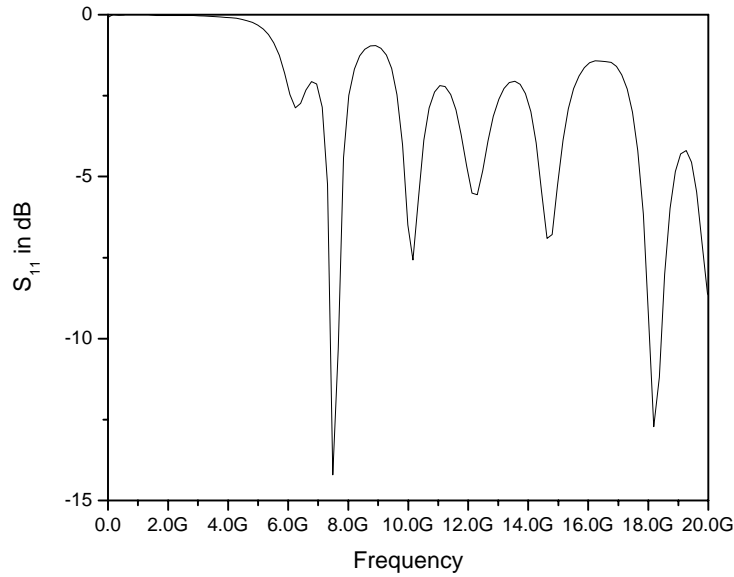


Fig. 4.3-5 S_{11} in dB for coarse grid (Fig. 4.3-3 b).

In this simulation, we refine the grid around the antenna plane in the z -direction as shown in Fig. 4.3-3 c. The two cells adjacent to antenna plane have a grid size of $\Delta z' = \Delta z / 2 = 0.1985mm$ and for the rest of the cells the grid size is $\Delta z = 0.397mm$. The time-step is the same as the coarse grid time-step, which is $\Delta t = 0.7606ps$. The calculated scattering parameters are shown in Fig. 4.3-6. The first calculated resonant frequency is $f_c = 7.489 GHz$ and is shown in Table 4.3-1.

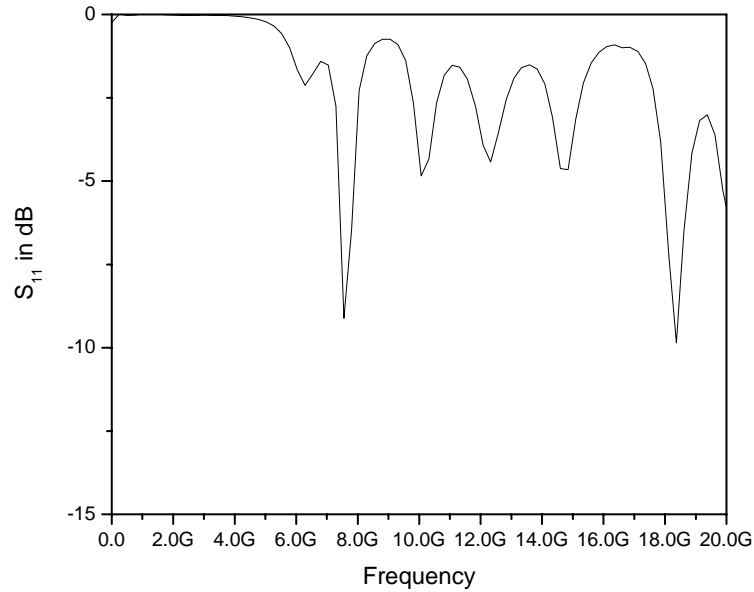


Fig. 4.3-6 S_{11} in dB for a coarse grid in the z-direction which is refined around the antenna plane (Fig. 4.3-3 c).

Table 4.3-1 The first calculated resonant frequency for different grid structures in the z-direction.

Mesh Type	Fine Mesh (Fig. 7-3 a)	Coarse Mesh (Fig. 7-3 b)	Coarse Mesh and Refined Mesh (Fig. 7-3 c)
Resonant Freq. (GHz)	7.4624	7.5484	7.489
Relative Simulation Time	1	0.55	0.62

As we see in Table 4.3-1, by coarsening the grid, the resonant frequency is not very accurate. To get more accurate results, we only refined the grid around the antenna plane which gives more accurate results without increasing the computational cost.

Chapter 5 Absorbing Boundary Condition (ABC)

5.1 Theory

Due to the limitations of memory resources, when using finite difference methods to solve for the fields in open regions, the infinite domain is truncated to a finite one by artificial boundaries that enclose the source of radiation and the objects that interact with the source. On the outer boundaries, an absorbing boundary condition (ABC) is enforced to simulate its extension to infinity. The ABC is not expected to provide the complete annihilation of the outgoing waves; rather it suppresses the spurious reflections of the outgoing numerical waves to an acceptable level.

Based on the theory of one-way wave equations developed by Engquist-Majda [5-1], the two-dimensional wave equation

$$\frac{\partial^2 U}{\partial x^2} + \frac{\partial^2 U}{\partial y^2} - \frac{1}{c^2} \frac{\partial^2 U}{\partial t^2} = 0 \quad (5.1-1)$$

can be written as

$$GU = 0 \quad (5.1-2)$$

and the partial-differential operator G is defined as

$$G \equiv \frac{\partial^2}{\partial x^2} + \frac{\partial^2}{\partial y^2} - \frac{1}{c^2} \frac{\partial^2}{\partial t^2} \equiv D_x^2 + D_y^2 - \frac{1}{c^2} D_t^2 \quad (5.1-3)$$

The operator G can be factored in the following manner

$$G^+ G^- U = 0 \quad (5.1-4)$$

where

$$G^- \equiv D_x - \frac{D_t}{c} \sqrt{1 - S^2} \quad (5.1-5)$$

and

$$G^+ \equiv D_x + \frac{D_t}{c} \sqrt{1 - S^2} \quad (5.1-6)$$

with

$$S \equiv \frac{D_y}{(D_t/c)} \quad (5.1-7)$$

Engquist and Majda demonstrated that the application of G^- to the wave function U , absorbs a plane wave propagating at any angle toward the left boundary.

Thus,

$$G^- U = 0 \quad (5.1-8)$$

completely absorbs the plane wave propagating at any arbitrary angle toward the left grid boundary and

$$G^+ U = 0 \quad (5.1-9)$$

completely absorbs the plane wave propagating at any arbitrary angle toward the right grid boundary.

The square roots in (5.1-5) and (5.1-6) prohibit the exact numerical implementation of (5.1-8) and (5.1-9). Therefore, we need to approximate the square roots to produce the partial-differential equations that can be implemented numerically. Using the first term of the Taylor's series expansion gives

$$\sqrt{1 - S^2} \cong 1 \quad (5.1-10)$$

which, when substituted in (5.1-5) and (5.1-6) gives the corresponding partial-differential equations that can be numerically implemented as a first-order accurate

ABC at the grid boundary. Using the same procedure, $\sqrt{1-S^2}$ can be written as a two-term Taylor series, with the result being the second-order accurate ABC.

5.2 Higdon's ABC

Higdon proposed ([5-2], and [5-3]) a differential annihilator of the plane waves of the form

$$\left[\prod_{l=1}^L \left(\cos \alpha_l \frac{\partial}{\partial t} - c \frac{\partial}{\partial x} \right) \right] U = 0 \quad (5.2-1)$$

This operator absorbs all $2L$ waves coming toward ABC with angles of $\pm\alpha_1, \pm\alpha_2, \dots, \pm\alpha_L$.

The generalized form of the N^{th} order Higdon's ABC is

$$B_N U = \prod_{i=1}^N \left(\partial_x + \frac{\cos \phi_i}{c} \partial_t + \alpha_i \right) U = 0 \quad (5.2-2)$$

where c is the speed of light, ϕ_i is the incident angle for which the boundary condition is perfectly absorptive, and α_i is the damping factor. He showed that the ABCs proposed by Engquist-Majda are special cases of the generalized Higdon's ABC. To discretize (5.2-2) into a difference equation, we use the following operators

$$\partial_x \rightarrow \left(\frac{I - S^{-1}}{\Delta x} \right) \left((1-a)I + aT^{-1} \right) \quad (5.2-3)$$

$$\partial_t \rightarrow \left(\frac{I - T^{-1}}{\Delta t} \right) \left((1-b)I + bS^{-1} \right) \quad (5.2-4)$$

where I is the identity operator, S^{-1} is the space shift operator, and T^{-1} is the time shift operator. The choices of the weighting coefficients a and b give different difference schemes including the forward Euler ($a=0, b=1$), backward Euler

($a=b=0$), and box scheme ($a=b=0.5$), etc. In general, the weighting coefficients are positive real numbers bounded by unity. The shift operators are explicitly expressed as

$$IU(t = n\Delta t, x = m\Delta x, y = l\Delta y) = U(t = n\Delta t, x = m\Delta x, y = l\Delta y) = u_{m,l}^n \quad (5.2-5)$$

$$T^{-i}U(t = n\Delta t, x = m\Delta x, y = l\Delta y) = U(t = (n-i)\Delta t, x = m\Delta x, y = l\Delta y) = u_{m,l}^{n-i} \quad (5.2-6)$$

$$S_x^{-i}U(t = n\Delta t, x = m\Delta x, y = l\Delta y) = U(t = n\Delta t, x = (m-i)\Delta x, y = l\Delta y) = u_{m-i,l}^n \quad (5.2-7)$$

$$S_y^{-i}U(t = n\Delta t, x = m\Delta x, y = l\Delta y) = U(t = n\Delta t, x = m\Delta x, y = (l-i)\Delta y) = u_{m,l-i}^n \quad (5.2-8)$$

$i = 1, 2, 3, \dots$

Substituting the operators (5.2-3) and (5.2-4) into (5.2-2), we have

$$B_N U = \prod_{i=1}^N (I + a_i T^{-1} + b_i S^{-1} + c_i S^{-1} T^{-1}) U = 0 \quad (5.2-9)$$

where

$$a_i = \frac{-(a - h(1-b))}{a - 1 - h(1-b) - \alpha_i \Delta x} \quad (5.2-10)$$

$$b_i = \frac{-(a - 1 + hb)}{a - 1 - h(1-b) - \alpha_i \Delta x} \quad (5.2-11)$$

$$c_i = \frac{-(-a - hb)}{a - 1 - h(1-b) - \alpha_i \Delta x} \quad (5.2-12)$$

$$h = \frac{\cos \phi_i \Delta x}{c \Delta t} \quad (5.2-13)$$

From (5.2-9), the difference formula of the first-order Higdon's ABC (i.e., $N=1$), is a linear and constant coefficient scheme. Furthermore, the difference scheme of the higher-order Higdon's ABC (i.e., $N \geq 2$) is also a linear and constant coefficient formula since it is derived from cascading the first-order formulas.

5.2.1 Implementation of the Higdon's ABC in the ADI-FDTD Method

In this experiment we apply the first-, and third-order Higdon's ABC in the ADI-FDTD method. The simulated structure has dimensions of $5\text{mm} \times 5\text{mm} \times 5\text{mm}$ and grid size of $\Delta = 0.25\text{mm}$ (Fig. 5.2-1). The source is located at $(2.5\text{mm}, 2.5\text{mm}, 2.5\text{mm})$ and monitor point is selected at $(2.5\text{mm}, 3.75\text{mm}, 2.5\text{mm})$ (Fig. 5.2-1). The excitation is a Gaussian pulse

$$f(t) = \exp\left(-\frac{(t-t_d)^2}{\tau^2}\right)$$

with $t_d = 80\text{ps}$ and $\tau = 20\text{ps}$. The results of the first-, and third-order Higdon's ABC simulations are shown in Fig. 5.2-2. As we see in Fig. 5.2-2, and more clearly in Fig. 5.2-3, the third-order Higdon's ABC is unstable.

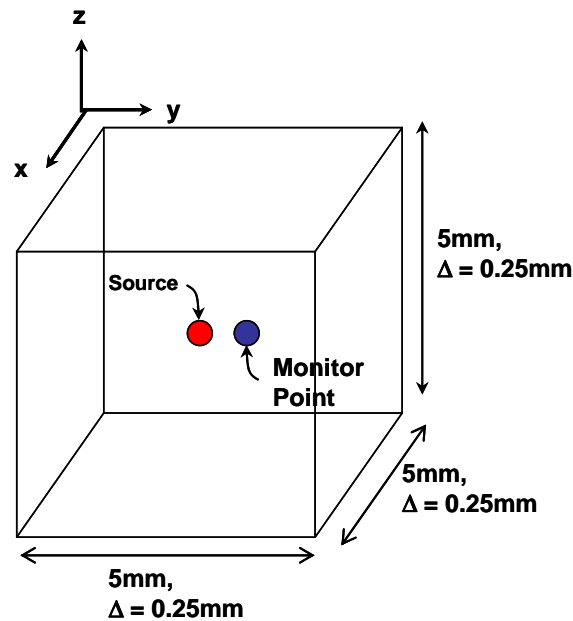


Fig. 5.2-1 Structure of three-dimensional open-region simulation and the locations of source and monitor points.

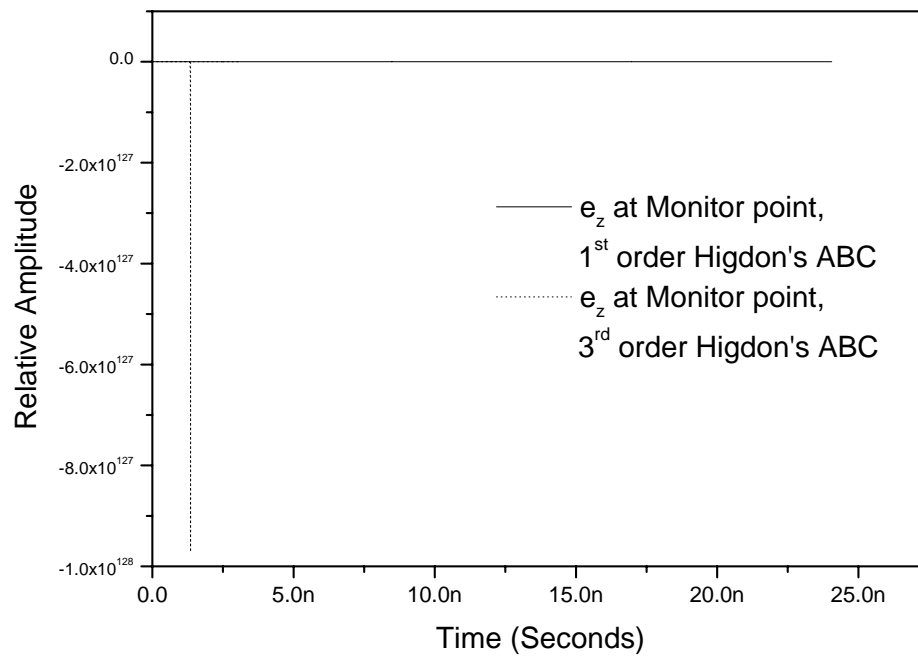


Fig. 5.2-2 Simulation results of the first-, and third-order Higdon's ABCs implemented in the ADI-FDTD method.

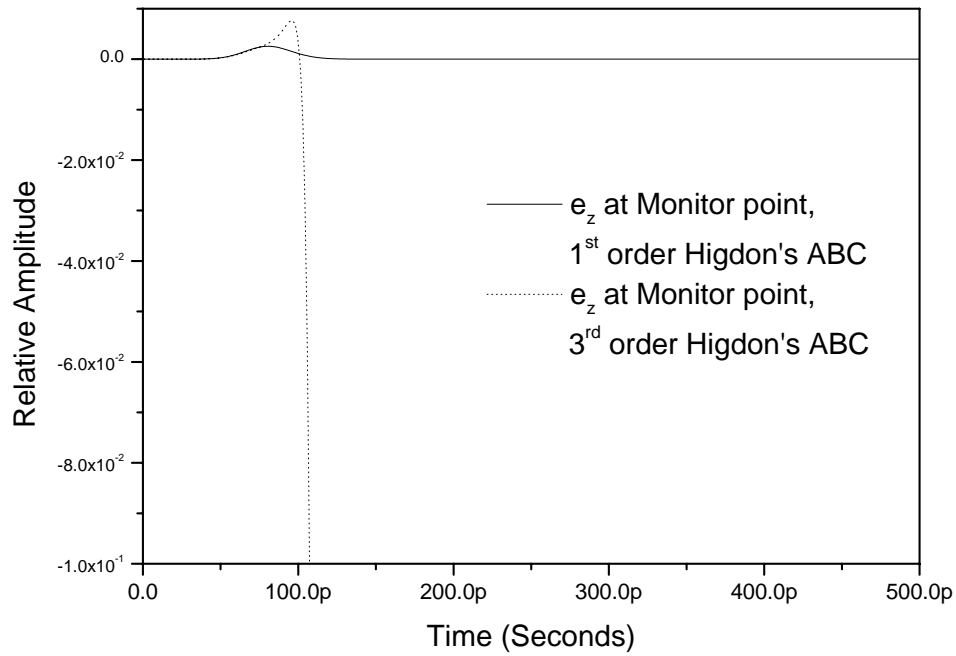


Fig. 5.2-3 Scaled simulation results of the first, and third-order Higdon's ABCs implemented in the ADI-FDTD method.

In [5-4] they have demonstrated that the third-order Higdon's ABC is unconditionally unstable and our simulation results confirm their conclusion.

5.3 Complementary Operators Method (COM)

The ABC is not expected to provide complete annihilation of the outgoing waves and, consequently, an error is introduced in the solution. Since the performance of a particular ABC depends on the location of the mesh-terminating wall, we can measure the error caused by the application of the ABC by expressing the total time-harmonic field as a summation of the outgoing and incoming waves at the artificial boundary. Suppose we have a computational boundary at $x=a$, where the

interior of the domain is the region to the left of the boundary (Fig. 5.3-1). We can express the field at any point to the left of the boundary as

$$U = e^{-jk_x x - jk_y y - jk_z z + j\omega t} + R e^{jk_x x - jk_y y - jk_z z + j\omega t} \quad (5.3-1)$$

Ideally, we would like to have zero reflection from computational boundaries. Therefore, the spurious reflection that is caused by the imperfect absorption of the computational wall is given by the second term in (5.3-1)

$$R e^{jk_x x - jk_y y - jk_z z + j\omega t} \quad (5.3-2)$$

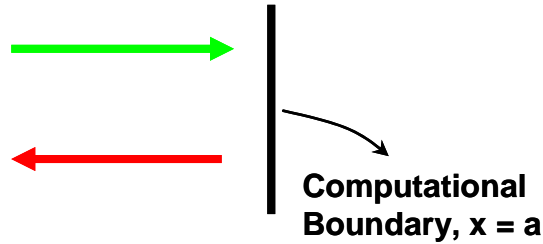


Fig. 5.3-1 Outgoing and incoming waves at the computational boundary.

In [5-5]-[5-7], they define a complementary ABC, which if applied to the same problem results in an error of similar magnitude but opposite in phase to what was obtained with the original ABC (Fig. 5.3-2). Denoting the new solution as U^c , we have

$$U^c = e^{-jk_x x - jk_y y - jk_z z + j\omega t} - R e^{jk_x x - jk_y y - jk_z z + j\omega t} \quad (5.3-3)$$

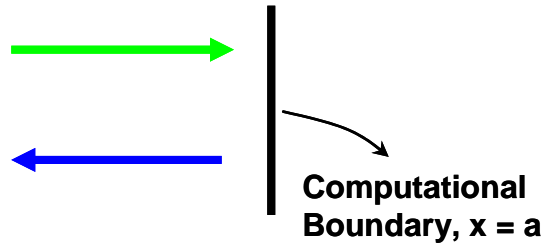


Fig. 5.3-2 Outgoing and complementary incoming waves at the computational boundary.

It follows that the reflection-free solution, or the numerically exact solution, denoted as U^{exact} is the average of the two solutions in (5.3-1) and (5.3-3) (Fig. 5.3-3)

$$U^{exact} = \frac{U + U^c}{2} \tag{5.3-4}$$

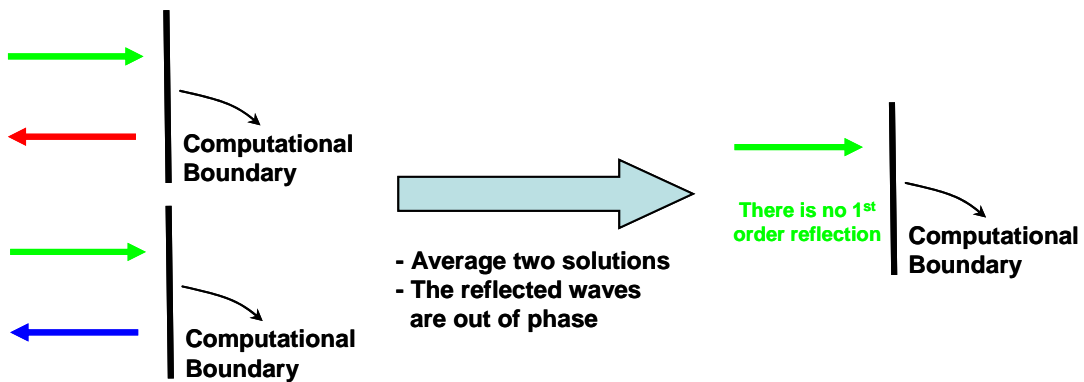


Fig. 5.3-3 Complementary reflections and average of them that cancels the first-order reflection.

Unfortunately, in practical applications, this ideal scenario does not take place because of the presence of the radiating structure, the finiteness of the terminating wall and the remaining mesh-terminating boundaries. All these result in multiple

spurious reflections of higher orders, which all do not cancel when averaging the two solutions as in (5.3-4).

As introduced in (5.2), the generalized form of the N^{th} -order Higdon's ABC is

$$B_N U = \prod_{i=1}^N \left(\partial_x + \frac{\cos \phi_i}{c} \partial_t + \alpha_i \right) U = 0 \quad (5.3-5)$$

The corresponding reflection coefficient R for time-harmonic fields is found by substituting (5.3-1) into (5.3-5)

$$R[B_N] = (-1) \prod_{i=1}^N \frac{-jk_x + j \cos \phi_i k + \alpha_i}{jk_x + j \cos \phi_i k + \alpha_i} \quad (5.3-6)$$

Aside from the added flexibility that $\cos \phi_i$ and α_i introduce, these constants can also be manipulated to lead to complementary pairs. By observation, if we set $\cos \phi_N = \alpha_N = 0$ in (5.3-6), we arrive at the reflection coefficient

$$R[B^c_N] = (+1) \prod_{i=1}^{N-1} \frac{-jk_x + j \cos \phi_i k + \alpha_i}{jk_x + j \cos \phi_i k + \alpha_i} \quad (5.3-7)$$

The corresponding ABC, denoted by B^c_N is readily found to be

$$B^c_N = \partial_x \prod_{i=1}^{N-1} \left(\partial_x + \frac{\cos \phi_i}{c} \partial_t + \alpha_i \right) U = 0 \quad (5.3-8)$$

The new boundary condition in (5.3-8) is precisely the complementary version of the ABC in (5.3-5) of order $N-1$. By observation, we can express the new ABC as ∂_x operation on the original ABC of order $N-1$

$$B^c_N = \partial_x B_{N-1} \quad (5.3-9)$$

While the non-optimality of the complementary operator is clearly evident, since the magnitude of the reflection coefficient of both operators is equivalent, the new operator, nevertheless, provides us with the 180° phase shift that we are seeking.

5.3.1 Implementation of COM in the ADI-FDTD Method

In this experiment we investigate the stability of the second-order COM. We apply the second-order COM on the same structure as Fig. 5.2-1. The excitation is a Gaussian pulse

$$f(t) = \exp\left(-\frac{(t-t_d)^2}{\tau^2}\right)$$

with $t_d = 80ps$ and $\tau = 20ps$. Fig. 5.3-4 shows the simulation results of two operators of the second-order COM. As we see in Fig. 5.3-4, and more clearly in Fig. 5.3-5, the Higdon's operator is stable but the complementary operator is unstable.

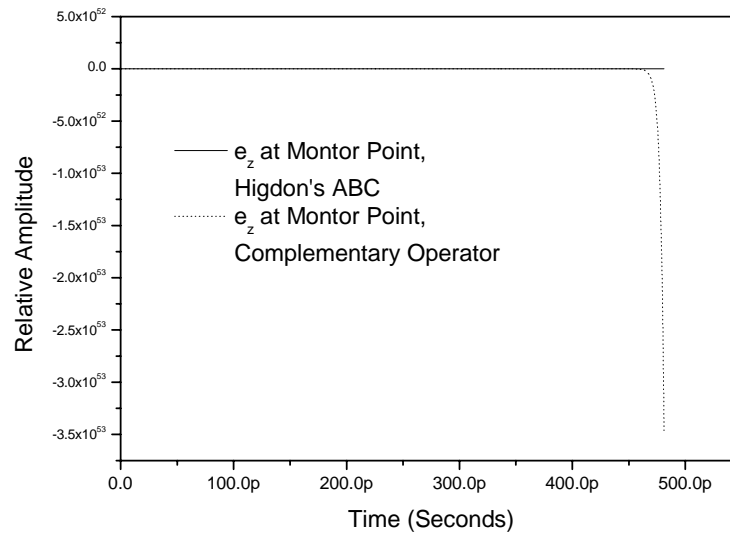


Fig. 5.3-4 Simulation results of the second-order COM implemented in the ADI-FDTD method.

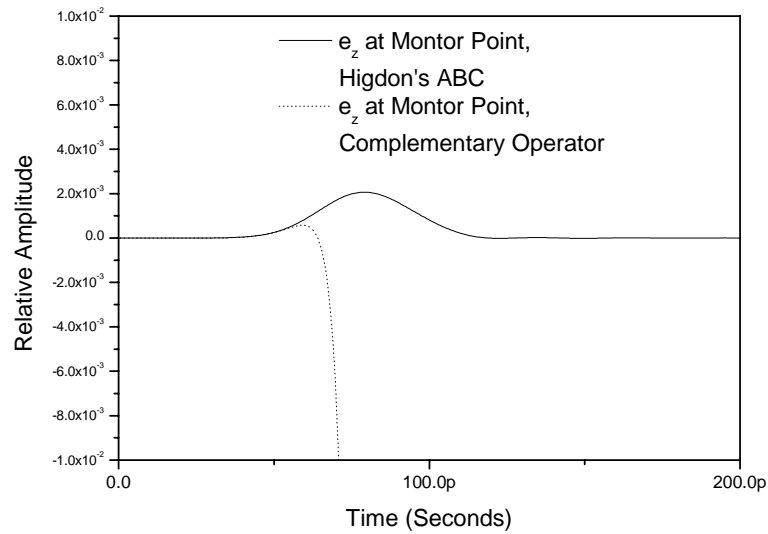


Fig. 5.3-5 Scaled simulation results of the second-order COM implemented in the ADI-FDTD method.

5.3.2 Analytical Investigation of Instability of the COM Using the Z-transform

Here, we use the Z-transform method to analytically investigate the stability of ABCs [5-4]. Consider a linear time-invariant (LTI) system given by the transfer function

$$H(z) = \frac{N(z)}{(z-p_1)(z-p_2)\dots(z-p_n)} \quad (5.3.2-1)$$

where p_1, p_2, \dots, p_n denote the poles of $H(z)$, and $N(z)$ is a polynomial. The system $H(z)$ is asymptotically stable if and only if $|p_i| < 1$ for $i=1,2,\dots,n$. Based on the LTI system theory, the system is marginally stable if and only if $|p_i| \leq 1$ for all non-repeated poles, and $|p_i| < 1$ for all repeated poles.

The Higdon's ABC is a linear combination of the interior nodes' values at the current and previous time steps. We define a system in which the output is the ABC value and inputs are the values of the interior nodes. It is clear that this system is an LTI system.

Suppose that u_m^n (m is the spatial index and n is the time index) is the ABC value or output of the system and u_{m-i}^{n-k} $i=1,2,..$ and $k=1,2,..$ are the interior nodes' values or the inputs of the system. Denoting the Z-transform operation by Z , we apply the Z-transform on the ABC value. We have

$$Y(z) \equiv Z(u_m^n) \tag{5.3.2-2}$$

Next, we apply the Z-transform on the ABC values, but at the previous time steps. Using the Z-transform properties, we have

$$\begin{aligned} Z(u_m^{n-1}) &= z^{-1}Y(z) \\ Z(u_m^{n-2}) &= z^{-2}Y(z) \\ &\dots \\ Z(u_m^{n-L}) &= z^{-L}Y(z) \end{aligned} \tag{5.3.2-3}$$

Applying the Z-transform on the internal nodes' values of time step n , we have

$$\begin{aligned} X_1(z) &= Z(u_{m-1}^n) \\ X_2(z) &= Z(u_{m-2}^n) \\ &\dots \\ X_N(z) &= Z(u_{m-N}^n) \end{aligned} \tag{5.3.2-4}$$

Note that L is the number of previous time steps and N is the number of internal nodes used to calculate the value of absorbing boundary condition.

The value of each node represents the numerical solution of the wave equation at that node. Also, we know that the ABCs are not perfect and there is some reflection from the ABC. Therefore, the values of different interior nodes can be written as

$$\begin{aligned}
u_m^n &= \left(e^{j\omega n \Delta t} e^{-jk_x m \Delta x} + \rho e^{j\omega n \Delta t} e^{+jk_x m \Delta x} \right) \\
u_{m-1}^n &= \left(e^{j\omega n \Delta t} e^{-jk_x (m-1) \Delta x} + \rho e^{j\omega n \Delta t} e^{+jk_x (m-1) \Delta x} \right) \\
u_{m-2}^n &= \left(e^{j\omega n \Delta t} e^{-jk_x (m-2) \Delta x} + \rho e^{j\omega n \Delta t} e^{+jk_x (m-2) \Delta x} \right) \\
&\dots \\
u_{m-N}^n &= \left(e^{j\omega n \Delta t} e^{-jk_x (m-N) \Delta x} + \rho e^{j\omega n \Delta t} e^{+jk_x (m-N) \Delta x} \right)
\end{aligned} \tag{5.3.2-5}$$

where k_x is the wave number in the x -direction (ABC for propagating waves along the x -direction), and ρ is the reflection coefficient.

Using the linearity property of the Z -transform, equations (5.3.2-2) to (5.3.2-5), and after some algebraic manipulation, the Z -transform of interior nodes values can be expressed as a combination of $X_1(z)$ and $Y(z)$ [5-4].

$$\begin{aligned}
X_2(z) &= 2 \cos(k_x \Delta x) X_1(z) - Y(z) \\
X_3(z) &= [1 + 2 \cos(2k_x \Delta x)] X_1(z) - 2 \cos(k_x \Delta x) Y(z) \\
X_4(z) &= 4 \cos(k_x \Delta x) 2 \cos(2k_x \Delta x) X_1(z) - [1 + 2 \cos(2k_x \Delta x)] Y(z)
\end{aligned} \tag{5.3.2-6}$$

The ABC can be expressed as a weighted polynomial of the space- and time-shift operators

$$BU = \left(-I + \sum_{i=0}^I \sum_{k=0}^K \beta_{i,k} S^{-i} T^{-k} \right) U = -u_m^n + \sum_{i=0}^I \sum_{k=0}^K \beta_{i,k} u_{m-i}^{n-k} = 0 \tag{5.3.2-7}$$

By applying the Z -transform on (5.3.2-7) and using (5.3.2-2)-(5.3.2-6), we can calculate the transfer function of the system.

$$H(z) = \frac{Y(z)}{X_1(z)} \quad (5.3.2-8)$$

Here, we use the Z-transform to investigate the instability of the second-order COM. The second-order Higdon's ABC is given by

$$B_2 U = \prod_{i=1}^2 \left(\partial_x + \frac{\cos \phi_i}{c} \partial_t + \alpha_i \right) U = 0 \quad (5.3.2-9)$$

or in difference form can be written as

$$B_2 U = \prod_{i=1}^2 \left(I + a_i T^{-1} + b_i S^{-1} + c_i S^{-1} T^{-1} \right) U = 0 \quad (5.3.2-10)$$

which after some manipulation is

$$\left(\begin{array}{l} I + (a_1 + a_2) T^{-1} + (b_1 + b_2) S^{-1} + (c_1 + c_2 + a_1 b_2 + a_2 b_1) S^{-1} T^{-1} + (a_1 a_2) T^{-2} + \\ (b_1 b_2) S^{-2} + (a_1 c_2 + a_2 c_1) S^{-1} T^{-2} + (b_1 c_2 + b_2 c_1) S^{-2} T^{-1} + (c_1 c_2) S^{-2} T^{-2} \end{array} \right) U = 0 \quad (5.3.2-11)$$

The second-order complementary operator is given by

$$B_2^c U = \partial_x \left(\partial_x + \frac{\cos \phi_i}{c} \partial_t + \alpha_i \right) U = 0 \quad (5.3.2-12)$$

By observation, the complementary operator is equal to the second-order Higdon's ABC when $a_2 = -1$, $b_2 = 1$, $c_2 = -1$. Therefore, its difference form is

$$\left(\begin{array}{l} I + (a_1 - 1) T^{-1} + (b_1 + 1) S^{-1} + (c_1 - 1 + a_1 - b_1) S^{-1} T^{-1} + (-a_1) T^{-2} + \\ (b_1) S^{-2} + (-a_1 - c_1) S^{-1} T^{-2} + (-b_1 + c_1) S^{-2} T^{-1} + (-c_1) S^{-2} T^{-2} \end{array} \right) U = 0 \quad (5.3.2-13)$$

Expressed as nodal fields, the complementary operator becomes

$$\begin{aligned} u_m^n + (a_1 - 1) u_m^{n-1} + (b_1 + 1) u_{m-1}^n + (c_1 - 1 + a_1 - b_1) u_{m-1}^{n-1} + (-a_1) u_m^{n-2} + \\ (b_1) u_{m-2}^n + (-a_1 - c_1) u_{m-1}^{n-2} + (-b_1 + c_1) u_{m-2}^{n-1} + (-c_1) u_{m-2}^{n-2} = 0 \end{aligned} \quad (5.3.2-14)$$

Applying the Z-transform to (5.3.2-14), and using the properties of (5.3.2-2)-(5.3.2-6), the transfer function of the complementary operator is

$$H_c(z) = \frac{Y_c(z)}{X_1(z)} = \frac{b_1 + 1 + 2b \cos(k_x \Delta x) + (-b_1 - 1 + 2(-b_1 + c_1) \cos(k_x \Delta x))z^{-1} - 2c_1 \cos(k_x \Delta x)z^{-2}}{(1 - b_1) + (a_1 - 1 + b_1 - c_1)z^{-1} + (c_1 - a_1)z^{-2}} \quad (5.3.2-15)$$

The poles of (5.3.2-15) are obtained by solving for the roots of the equation

$$(1 - b_1) + (a_1 - 1 + b_1 - c_1)z^{-1} + (c_1 - a_1)z^{-2} = 0 \quad (5.3.2-16)$$

giving the two roots

$$z_1 = 1$$

$$z_2 = \frac{c_1 - a_1}{1 - b_1}$$

From the system theory we know that an input with a DC term causes instability in a system having a pole at $z=1$. Therefore, the second-order COM excited with a Gaussian pulse, which has a DC term, is unstable.

Chapter 6 Complementary Derivatives Method

6.1 CDM Theory

In this section, and without loss of generality, we introduce the Complementary Derivatives Method (CDM) on the classical Finite-Difference Time-Domain (FDTD) method based on the Yee scheme [6-1], [6-2]. The arrangement of electric and magnetic fields along the x -axis is shown in Fig. 6.1-1. The updating equations are based on discretizing the derivative operators in time and space. The first-order time derivative is discretized using the central difference scheme, achieving second-order accuracy. The same procedure is used for space derivatives, similarly achieving second-order accuracy if the grid size remains unchanged. To this end, let us construct a computational domain composed of two regions with boundary x_0 as the interface between the regions (shown by dashed line in Fig. 6.1-1). In this case we assume that the cell size changes from Δ to $\Delta^R = \Delta'$ at the interface. Using Taylor series expansion, we express the magnetic fields on both sides of the interface as

$$H\left(x_0 + \frac{\Delta'}{2}\right) = H(x_0) + (\Delta'/2)H'(x_0) + \frac{(\Delta'/2)^2}{2}H''(x_0) + O(3) \quad (6.1-1)$$

$$H\left(x_0 - \frac{\Delta}{2}\right) = H(x_0) - (\Delta/2)H'(x_0) + \frac{(\Delta/2)^2}{2}H''(x_0) - O(3) \quad (6.1-2)$$

By subtracting (6.1-1) from (6.1-2), and after several algebraic manipulations we can write the derivative of $H'(x_0)$ as

$$H'(x_0) = \frac{H(x_0 + \Delta'/2) - H(x_0 - \Delta/2)}{(\Delta' + \Delta)/2} - \frac{\Delta' - \Delta}{4}H''(x_0) + O(2) \quad (6.1-3)$$

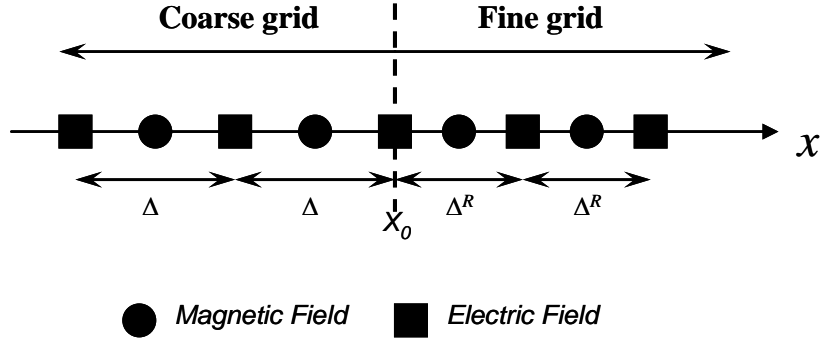


Fig. 6.1-1 Arrangement of E -fields and H -fields along the x -axis in the FDTD domain based on the Yee scheme. The grid size changes from Δ to Δ^R at the grid boundary.

Next, we construct a second domain in which the grid size changes from Δ to $\Delta^R = \Delta''$. Using identical procedure, the derivative of the magnetic field, $H'(x_0)$, for the new cell size can be written as

$$H'(x_0) = \frac{H(x_0 + \Delta''/2) - H(x_0 - \Delta/2)}{(\Delta'' + \Delta)/2} - \frac{\Delta'' - \Delta}{4} H''(x_0) + O(2) \quad (6.1-4)$$

As we see in (6.1-3) and (6.1-4), the truncation error is first order. The arithmetic average of (6.1-3) and (6.1-4) gives

$$H'(x_0) = \frac{H(x_0 + \Delta'/2) - H(x_0 - \Delta/2)}{\Delta' + \Delta} + \frac{H(x_0 + \Delta''/2) - H(x_0 - \Delta/2)}{\Delta'' + \Delta} - \frac{1}{2} \left(\frac{\Delta' - \Delta}{4} + \frac{\Delta'' - \Delta}{4} \right) H''(x_0) + O(2) \quad (6.1-5)$$

As a sufficient condition for canceling the first-order truncation error, the third term on the right-hand side of (6.1-5) should be zero. This results in the following identity

$$\Delta = \frac{\Delta' + \Delta''}{2} \quad (6.1-6)$$

We define complementary derivatives as the two derivatives defined at the interface of two different computational domains of the same structure. Both domains have identical grid size, henceforth referred to as the common grid size, on one side of the interface (to the left when considering Fig. 6.1-1). On the other side of the interface, the grid sizes are different subject to the condition that their arithmetic mean is equal to the common grid size. Averaging the two complementary derivatives at the interface achieves second-order accuracy.

The above procedure requires two separate simulations. For obvious reasons, this can be computationally unattractive. A single simulation implementation of CDM is possible as explained next.

Let us consider a computational domain with two different grid sizes separated by an interface as shown in Fig. 6.1-2. A second-order accurate E -field interpolation at the interface ($x=x_0$) is obtained using the symmetric H -fields at $x=x_0-\Delta/2$ and $x=x_0+\Delta/2$ as

$$H'(x_0) = \frac{H(x_0 + \Delta/2) - H(x_0 - \Delta/2)}{\Delta} + O(2) \quad (6.1-7)$$

Here, we assumed that there is an H -field node at $x=x_0+\Delta/2$. In the case where an H -field node does not coincide with the location $x=x_0+\Delta/2$, we make use of the H -fields at two nodes that exist, at $x=x_0+(\Delta/2-\delta_L)$ and $x=x_0+(\Delta/2+\delta_R)$. To see how this is accomplished, we express the derivative at x_0 using two different differencing schemes. The first expression for the derivative uses the points $x=x_0-\Delta/2$ and $x=x_0+(\Delta/2-\delta_L)$, resulting in

$$H'(x_0) = \frac{H(x_0 + \Delta/2 - \delta_L) - H(x_0 - \Delta/2)}{\Delta - \delta_L} + \frac{\delta_L}{2} H''(x_0) + O(2) \quad (6.1-8)$$

The second expression for the H -field derivatives uses the points $x=x_0-\Delta/2$ and $x=x_0+(\Delta/2+\delta_R)$, resulting in

$$H'(x_0) = \frac{H(x_0 + \Delta/2 + \delta_R) - H(x_0 - \Delta/2)}{\Delta + \delta_R} - \frac{\delta_R}{2} H''(x_0) + O(2) \quad (6.1-9)$$

The arithmetic mean of (6.1-8) and (6.1-9) gives

$$H'(x_0) = \frac{H(x_0 + \Delta/2 - \delta_L) - H(x_0 - \Delta/2)}{2(\Delta - \delta_L)} + \frac{H(x_0 + \Delta/2 + \delta_R) - H(x_0 - \Delta/2)}{2(\Delta + \delta_R)} + \frac{1}{4}(\delta_L - \delta_R)H''(x_0) + O(2) \quad (6.1-10)$$

To cancel the first-order truncation error, the third term of the right-hand side of (6.1-10) should be zero. To achieve this, we require that

$$\delta_L = \delta_R \quad (6.1-11)$$

Numerical implementation of the CDM can be achieved by simply determining the number of the two FDTD cells that are used to calculate the complementary derivatives. If we assume that one of the H -fields is in cell k_1 and the other one is in cell k_2 (as measured from the interface), δ_L and δ_R , as defined in Fig. 6.1-2, can be written as

$$\delta_L = \frac{\Delta}{2} - (2k_1 + 1)\frac{\Delta'}{2} \quad (6.1-12)$$

$$\delta_R = (2k_2 + 1)\frac{\Delta'}{2} - \frac{\Delta}{2} \quad (6.1-13)$$

Note that k_1 and k_2 do not necessarily represent adjacent cells. Enforcing (6.1-11), we have

Suppose that the grid size in the x -direction changes from Δ_x to $\Delta_x^R = \Delta_x'$ at x_0 and the grid size in the y -direction changes from Δ_y to $\Delta_y^R = \Delta_y'$ at y_0 (Fig. 6.1-3).

Discretizing (6.1-16) at (x_0, y_0) using the central difference scheme results in

$$f_t(x_0, y_0, z_0, t) = \alpha \left(\frac{f(x_0 + \Delta_x'/2, y_0, z_0, t) - f(x_0 - \Delta_x/2, y_0, z_0, t)}{(\Delta_x' + \Delta_x)/2} - \frac{\Delta_x' - \Delta_x}{4} \frac{\partial^2 f}{\partial x^2} \Big|_{x_0} \right) \\ + \beta \left(\frac{f(x_0, y_0 + \Delta_y'/2, z_0, t) - f(x_0, y_0 - \Delta_y/2, z_0, t)}{(\Delta_y' + \Delta_y)/2} - \frac{\Delta_y' - \Delta_y}{4} \frac{\partial^2 f}{\partial y^2} \Big|_{y_0} \right) \\ + O(2) \quad (6.1-17)$$

Similar to the one-dimensional case, we assume there is another domain in which the grid size in the x -direction changes from Δ_x to $\Delta_x^R = \Delta_x''$ at x_0 and the grid size in the y -direction changes from Δ_y to $\Delta_y^R = \Delta_y''$ at y_0 (Fig. 6.1-3). Discretization of (6.1-16) at (x_0, y_0) gives

$$f_t^c(x_0, y_0, z_0, t) = \alpha \left(\frac{f(x_0 + \Delta_x''/2, y_0, z_0, t) - f(x_0 - \Delta_x/2, y_0, z_0, t)}{(\Delta_x'' + \Delta_x)/2} - \frac{\Delta_x'' - \Delta_x}{4} \frac{\partial^2 f}{\partial x^2} \Big|_{x_0} \right) \\ + \beta \left(\frac{f(x_0, y_0 + \Delta_y''/2, z_0, t) - f(x_0, y_0 - \Delta_y/2, z_0, t)}{(\Delta_y'' + \Delta_y)/2} - \frac{\Delta_y'' - \Delta_y}{4} \frac{\partial^2 f}{\partial y^2} \Big|_{y_0} \right) \\ + O(2) \quad (6.1-18)$$

Arithmetic average of (6.1-17) and (6.1-18) gives

$$\begin{aligned}
& \frac{f_t + f_t^c}{2} = \\
& \alpha \left[\frac{f(x_0 + \Delta'_x/2, y_0, z_0, t) - f(x_0 - \Delta_x/2, y_0, z_0, t)}{\Delta'_x + \Delta_x} \right. \\
& \quad \left. + \frac{f(x_0 + \Delta''_x/2, y_0, z_0, t) - f(x_0 - \Delta_x/2, y_0, z_0, t)}{\Delta''_x + \Delta_x} \right. \\
& \quad \left. - \frac{1}{2} \left(\frac{\Delta'_x - \Delta_x}{4} + \frac{\Delta''_x - \Delta_x}{4} \right) \frac{\partial^2 f}{\partial x^2} \Big|_{x_0} \right] \\
& + \beta \left[\frac{f(x_0, y_0 + \Delta'_y/2, z_0, t) - f(x_0, y_0 - \Delta_y/2, z_0, t)}{\Delta'_y + \Delta_y} \right. \\
& \quad \left. + \frac{f(x_0, y_0 + \Delta''_y/2, z_0, t) - f(x_0, y_0 - \Delta_y/2, z_0, t)}{\Delta''_y + \Delta_y} \right. \\
& \quad \left. - \frac{1}{2} \left(\frac{\Delta'_y - \Delta_y}{4} + \frac{\Delta''_y - \Delta_y}{4} \right) \frac{\partial^2 f}{\partial y^2} \Big|_{y_0} \right] \\
& + O(2)
\end{aligned} \tag{6.1-19}$$

The truncation error can be improved to the second-order if the relation between grid sizes in the x -direction is

$$\Delta_x = \frac{\Delta'_x + \Delta''_x}{2} \tag{6.1-20}$$

and the relation between grid sizes in the y -direction is

$$\Delta_y = \frac{\Delta'_y + \Delta''_y}{2} \tag{6.1-21}$$

We can use the same procedure to implement the CDM even if the grid sizes are changing in the three directions. But in Maxwell's equations, each updating equation of the electric-field (magnetic-field) components uses the magnetic-field (electric-field) components that lie on a plane. In other words, a two-dimensional grid is needed to update each electric-, or magnetic-field components. Therefore, implementing CDM is required for at most two directions in the Maxwell's equations.

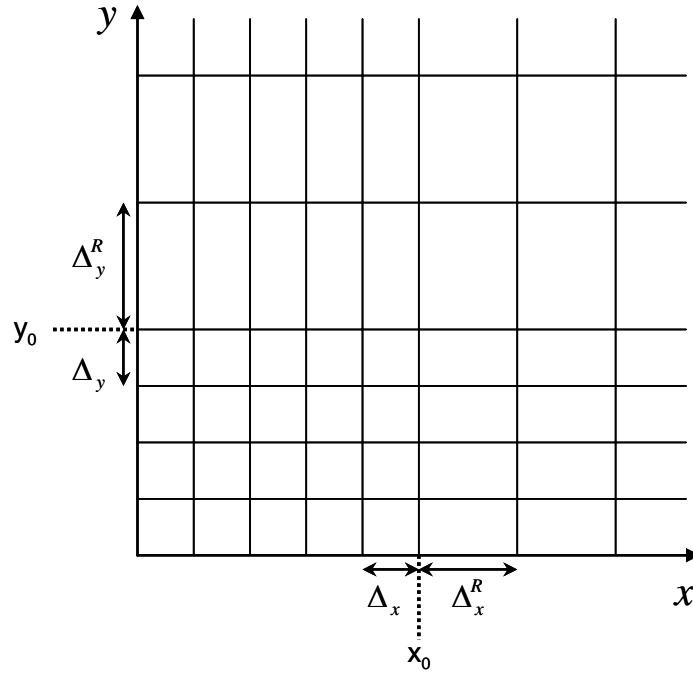


Fig. 6.1-3 Two-dimensional discretized structure. The grid size in the x -direction changes from Δ_x to Δ_x^R at x_0 and in the y -direction changes from Δ_y to Δ_y^R at y_0 .

6.2 Numerical Experiments

6.2.1 One-dimensional Experiments

To explain the concept of CDM, two simple one-dimensional experiments are presented in this section. First, we consider a one-dimensional domain of length $750mm$ with a uniform grid size of $\Delta=125\mu m$. This case will be considered as the reference. The second-order Higdon's absorbing boundary condition [6-3] is applied at both ends of the computational domain to isolate any terminal reflections. The source is positioned $250mm$ from the left domain boundary; the monitor point is at

375mm from the left domain boundary, 125mm from the source (Fig. 6.2.1-1). The excitation is a differentiated Gaussian pulse, given by

$$f(t) = \frac{-2}{\tau}(t-t_d)\exp\left(-\frac{(t-t_d)^2}{\tau^2}\right) \quad (6.2.1-1)$$

where $t_d=100ps$ and $\tau=20ps$. The simulation results of the relative amplitude of E_z for this reference case are shown in Fig. 6.2.1-3 by a solid line.

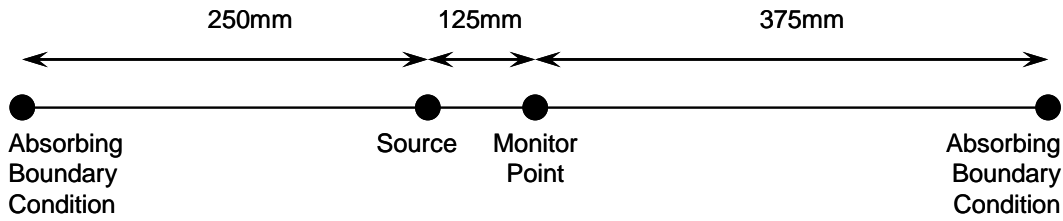


Fig. 6.2.1-1 One-dimensional reference structure. The grid size is uniform ($\Delta=125\mu m$) throughout the domain.

In the next step, we increase the grid size only on the left side of grid boundary to $\Delta = 250\mu m$ (left domain boundary to source is 250mm, source to monitor point is 125mm, monitor point to grid boundary is 125mm. See Fig. 6.2.1-2). The grid size on the right side of the grid boundary is the same as before $\Delta' = 125\mu m$ and the domain size is left unchanged (grid boundary to left domain boundary is 250mm. See Fig. 6.2.1-2).

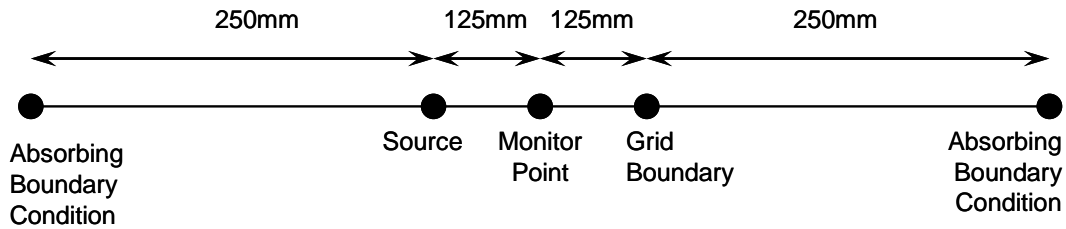


Fig. 6.2.1-2 Simulated structure with different grid sizes. The grid size on the left side of the grid boundary is $\Delta=250\mu\text{m}$ and on the right side of the grid boundary is $\Delta'=125\mu\text{m}$.

The simulation results of the structure depicted in Fig. 6.2.1-2 are shown in Fig. 6.2.1-3. The line with diamonds shows the results with the different grid size; and the line with circles illustrates the results when CDM is applied to cancel the first-order truncation errors. Since the grid size reduction factor is $1/2$, the H -fields of the first and second cells have been used as complementary derivatives. As we see in Fig. 6.2.1-3, the application of CDM significantly reduces reflection from the grid boundary.

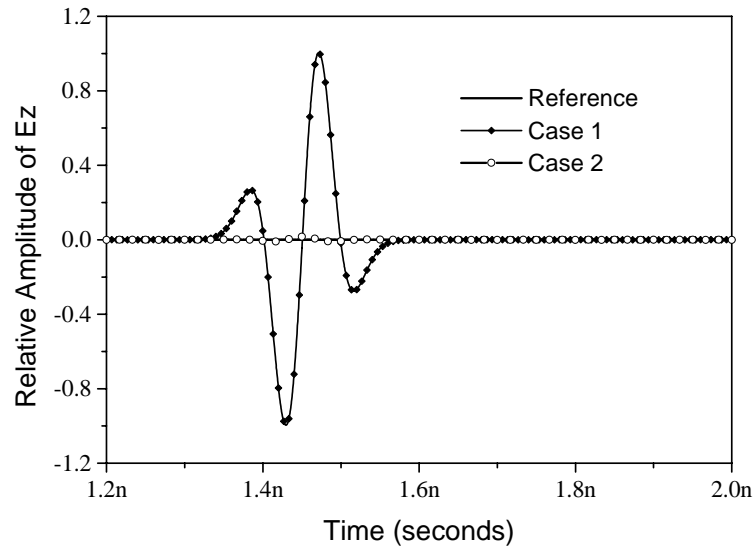


Fig. 6.2.1-3 One-Dimensional FDTD simulation results using different grid size scenarios; Reference: Standard Yee scheme applied to a domain with a uniform cell size of $\Delta = 125\mu\text{m}$. Case 1: Standard Yee scheme applied to two domains with different grid sizes of $\Delta = 250\mu\text{m}$ and $\Delta' = 125\mu\text{m}$. Case 2: CDM applied to two domains with different grid sizes of $\Delta = 250\mu\text{m}$ and $\Delta' = 125\mu\text{m}$.

In the second numerical experiment of this section we examine the case, in which there are different sets of complementary derivatives. Here, the one-dimensional FDTD domain is 340mm long with the grid size of $\Delta=50\mu\text{m}$, and the second-order Higdon's absorbing boundary condition [6-3] is applied at both ends of the computational domain to isolate any terminal reflections. The source is positioned 120mm from the left domain boundary and a monitor point is selected 50mm away from the source (Fig. 6.2.1-4). The same excitation as the previous experiment is

used. The simulation results for this reference case are shown in Fig. 6.2.1-7 by a solid line.

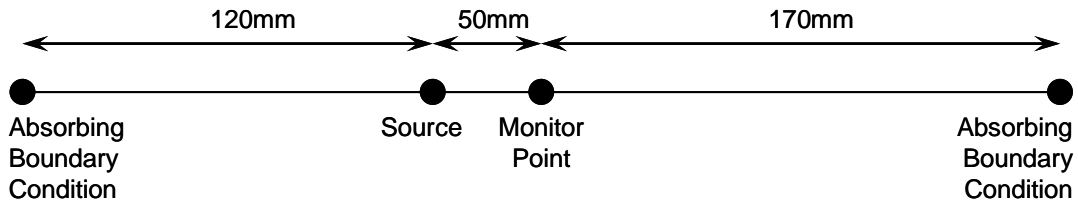


Fig. 6.2.1-4 Simulated structure as reference. The grid size is $\Delta=50\mu m$ on the entire domain.

Next, we increase the grid size on the left side of the grid boundary to $\Delta = 200\mu m$ (Fig. 6.2.1-5). The grid size on the right side of the grid boundary remains the same $\Delta' = 50\mu m$ and the domain size is left unchanged (grid boundary to left domain boundary is $120mm$. See Fig. 6.2.1-5).

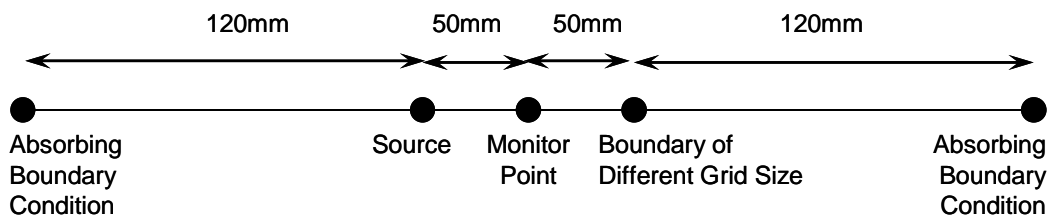


Fig. 6.2.1-5 Simulated structure with different grid sizes. The grid size on the left side of the grid boundary is $\Delta = 200\mu m$ and on the right side of the grid boundary is $\Delta' = 50\mu m$.

In this experiment, the grid size reduction factor is $\alpha=1/4$. Figs. 6.2.1-6 (a) and 6.2.1-6 (b) show the two different sets of points that can be used as complementary derivatives for a grid size reduction factor of $\alpha=1/4$.

The simulation results of the structure depicted in Fig. 6.2.1-5 are shown in Fig. 6.2.1-7. The dotted line with squares shows the results of different grid sizes. The line with crosses illustrates the simulation results of different grid sizes when CDM is applied (Fig. 6.2.1-6 (a)). The line with circles illustrates the simulation results of different grid sizes when CDM is applied (Fig. 6.2.1-6 (b)). As we see in Fig. 6.2.1-7, when CDM is applied a significant reduction in the grid boundary reflection is achieved.

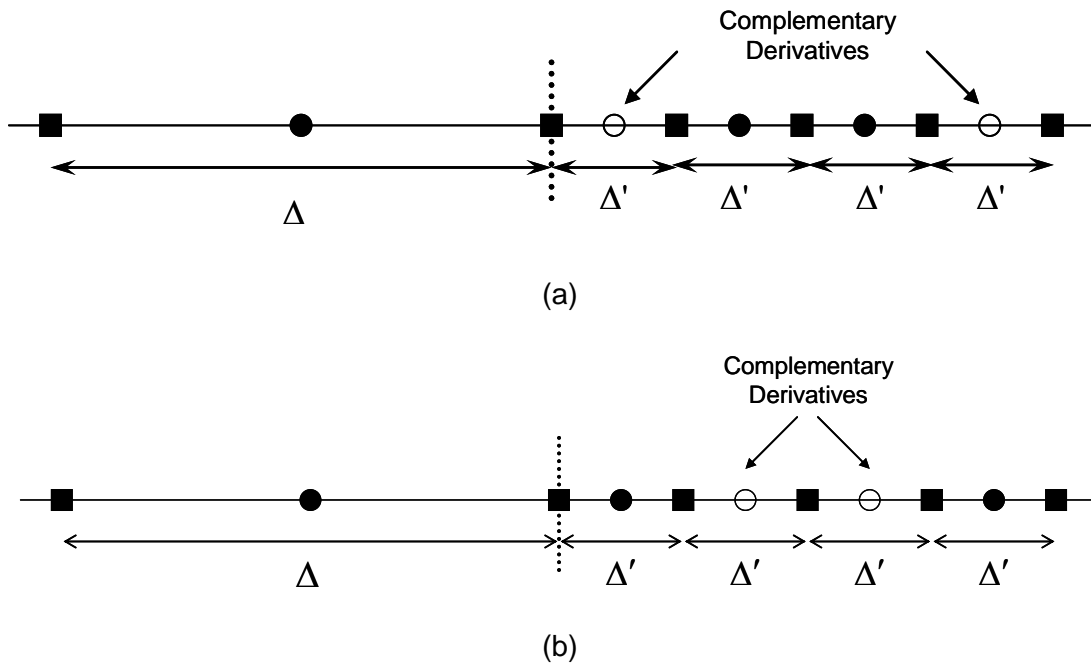


Fig. 6.2.1-6 Two different sets of complementary derivatives for a grid size reduction factor of $\alpha=1/4$.

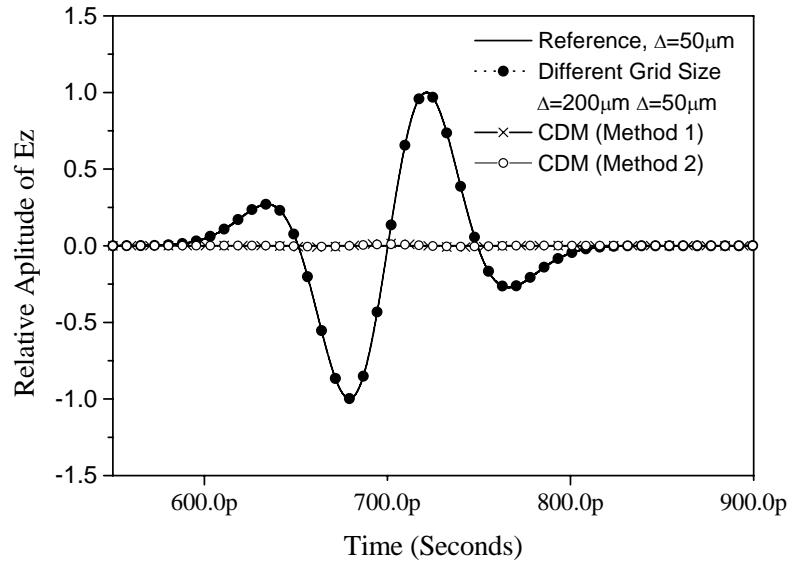


Fig. 6.2.1-7 One-dimensional FDTD simulation results using different grid size scenarios. Reference: Standard Yee scheme applied to a domain with a uniform cell size of $\Delta = 50\mu\text{m}$. Different Grid size: Standard Yee scheme applied to two domains with different grid sizes of $\Delta = 200\mu\text{m}$ and $\Delta' = 50\mu\text{m}$. CDM, Method 1: CDM (Method 1, Fig. 6.2.1-6 (a)) is applied to two domains with different grid sizes of $\Delta = 200\mu\text{m}$ and $\Delta' = 50\mu\text{m}$. CDM, Method 2: CDM (Method 2, Fig. 6.2.1-6 (b)) is applied to two domains with different grid sizes of $\Delta = 200\mu\text{m}$ and $\Delta' = 50\mu\text{m}$.

6.2.2 Two-dimensional Experiments

Here, the CDM is applied to the problem of a partially filled parallel plate waveguide of dimensions $420\text{mm} \times 30\text{mm}$. First, we consider a uniform grid size in the entire computational domain of the guide with $\Delta x = \Delta y = 1\text{mm}$ (Fig. 6.2.2-1). The

numerical results obtained from this case will be considered as the reference solution (E^{ref}). The z -polarized source is positioned at $(180mm, 15mm)$ and the monitor point is selected at $(200mm, 15mm)$. The second-order Higdon's absorbing boundary condition [6-3] is applied on boundaries at $x=0$ and $x=420mm$. The parallel plate waveguide is partially filled by a material of $\epsilon_r=10$ and the width of $50mm$ (Fig. 6.2.2-1). The rest of waveguide is empty ($\epsilon_r=1$). The excitation is a modulated Gaussian pulse

$$f(t) = \sin(2\pi f_m t) \exp\left(-\frac{(t-t_d)^2}{\tau^2}\right)$$

with $t_d = 480ps$, $\tau = 160ps$, and $f_m = 10GHz$.

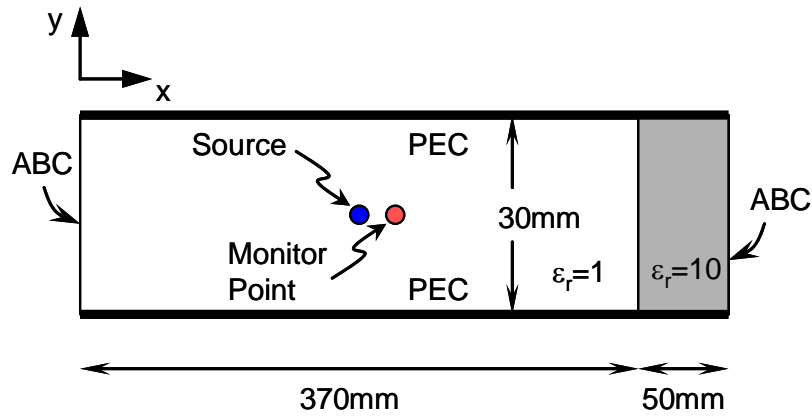


Fig. 6.2.2-1 Simulated structure as reference. The grid size is uniform ($\Delta x=\Delta y=1mm$) throughout the computational domain.

Next, we solve the same problem, but decrease the cell size to the right of the interface positioned at $x=220mm$ (Fig. 6.2.2-2) to $\Delta x' = 0.5, 0.25$ and $0.125mm$, corresponding to reduction ratios of $1:2, 1:4$ and $1:8$, respectively. The cell size in the

y-direction, locations of the source and monitor point, and excitation pulse are unchanged.

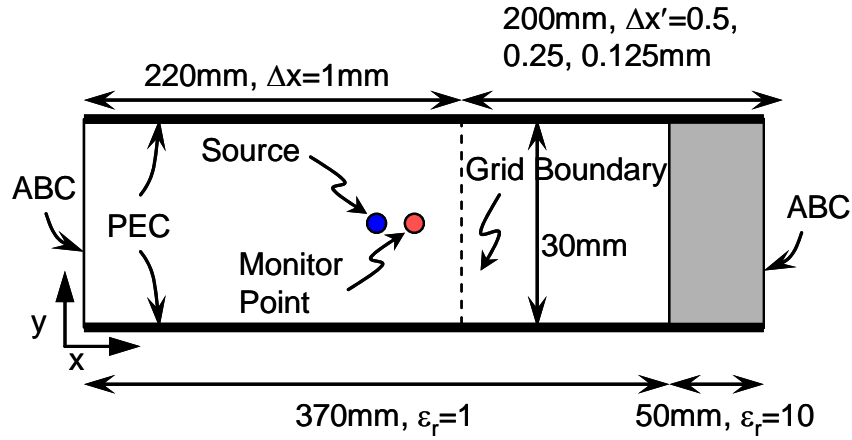


Fig. 6.2.2-2 Simulated structure with different grid sizes. The grid size in the y-direction is uniform ($\Delta y=1mm$) on the entire domain. The grid size in the x-direction changes from $\Delta x = 1mm$ to $\Delta x' = 0.5, 0.25, \text{ and } 0.125mm$.

We define the normalized error as

$$Normalized\ Error = 100 \times \left| \frac{E^{ref} - E}{\max(E^{ref})} \right| \quad (6.2.2-1)$$

In Fig. 6.2.2-3, we show the *Normalized Error* as a function of time for the cases with and without the application of CDM. A significant reduction of error in the *E*-field is observed when CDM is applied. Most importantly, it is observed that the error resulting from the application of CDM is practically independent of the mesh reduction ratio.

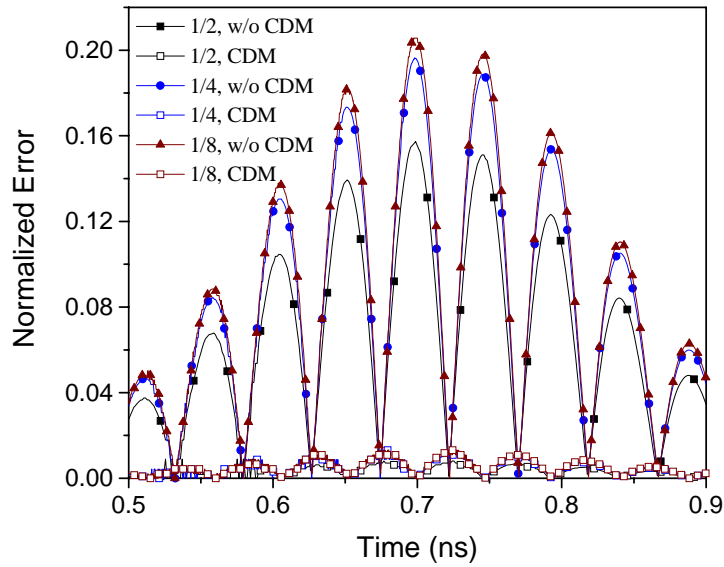


Fig. 6.2.2-3 Normalized error in the E -field as obtained using the standard FDTD interpolation scheme with and without CDM.

In the next experiment we simulate a dielectric slab-loaded rectangular waveguide [6-4]. A dielectric slab-loaded waveguide is a rectangular waveguide which is partially loaded with a slab of dielectric material. The dielectric slab is located vertically on the right side of the rectangular waveguide as shown in Fig. 6.2.2-4. The relative permittivity and permeability of the dielectric slab are $\epsilon_r = 11.7$ and $\mu_r = 1$, respectively. The side lengths for the rectangular waveguide along the x - and y -coordinates are $b = 10.29\text{mm}$ and $a = 20\text{mm}$, and the unfilled empty rectangular region is of width $d = 13.98\text{mm}$.

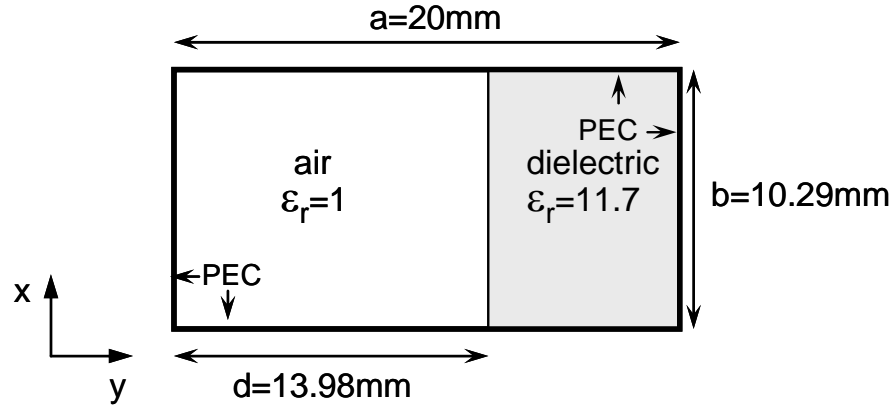


Fig. 6.2.2-4 Dielectric slab-loaded rectangular waveguide.

First, we consider a uniform grid size in the interior region of the rectangular waveguide with $\Delta x = \Delta y = 0.1942\text{mm}$ which results in 54 cells in the x -direction and 104 cells in the y -direction (Fig. 6.2.2-5). The perfect electric conductor boundary condition at the waveguide walls is simulated by appropriately truncating cells at the axial components of the electric field, E_z .

Initially, there is no excitation inside the waveguide region; all spatial magnetic and electric field components are assumed to be zero. A Gaussian pulse is then used to excite the axial z components of the electric field. The peak is placed at the center cell of the waveguide at (x_c, y_c) . The excitation pulse is given by

$$G(x, y, t = 0) = Ae^{-\frac{(x-x_c)^2 + (y-y_c)^2}{2\tau^2}} \quad (6.2.2-2)$$

Although any arbitrary field can be assigned to the cells inside the waveguide region, the Gaussian pulse is used as the initial assigned field because of its capability to excite all possible spatial frequency harmonics inside the rectangular waveguide.

The cutoff frequencies are obtained by first recording the temporal variation of the fields at the $(i=5, j=5)$ for $N=16384$ time steps, and then applying the FFT algorithm to convert the time domain data to the frequency domain. The first calculated cutoff frequency is $f_c = 17.47 \text{ GHz}$ (Table 6.2.2-1).

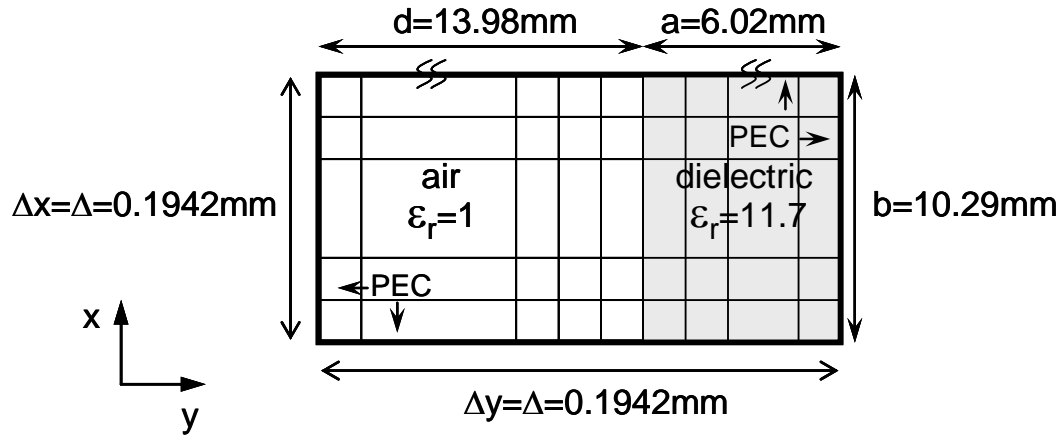


Fig. 6.2.2-5 Discretized structure using a uniform grid size of $\Delta x = \Delta y = \Delta = 0.1942 \text{ mm}$.

Next, we increase the spatial grid size to $\Delta x = \Delta y = \Delta = 0.6657 \text{ mm}$ which results in 17 cells in the x -direction and 31 cells in the y -direction (Fig. 6.2.2-6). The boundary condition at waveguide walls is simulated the same manner as the first experiment, i.e. by appropriately truncating cells at the axial components of the electric field, E_z .

Again, one-fourth of a Gaussian pulse with its peak placed at center is injected on the waveguide cross section to excite the waveguide. Using the same procedure to calculate the cutoff frequency results at $f_c = 16.82 \text{ GHz}$ (Table 6.2.2-1).

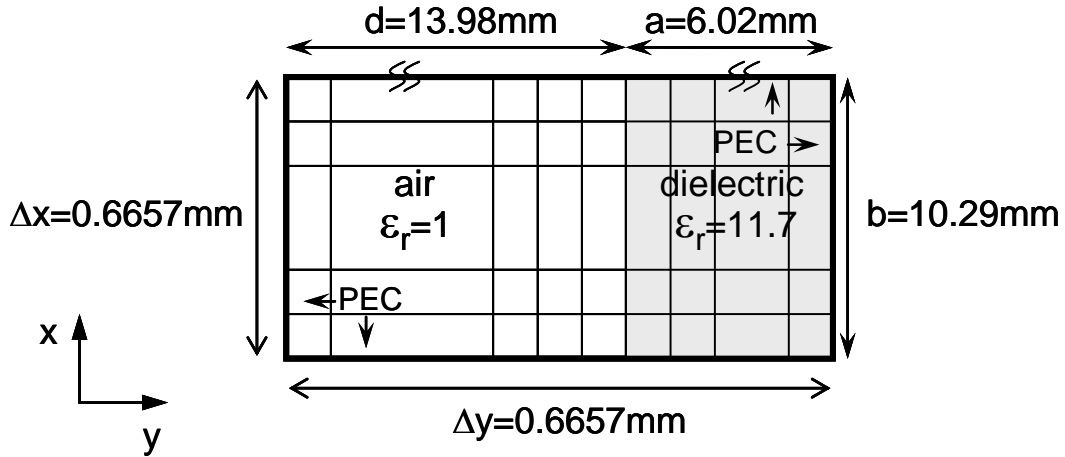


Fig. 6.2.2-6 Discretized structure using a uniform grid size of $\Delta x = \Delta y = \Delta = 0.6657\text{mm}$.

The structure of Fig. 6.2.2-6 is then refined at the vicinity of boundary between air and dielectric to improve the simulation results (Fig. 6.2.2-7). In the refined structure we reduce the grid size to half of the original grid size in the y -direction ($\Delta y = 0.6657\text{mm}$, $\Delta y' = 0.33285\text{mm}$) for 6 cells adjacent to the grid boundary in the y and $-y$ -directions. Using the same excitation and procedure to calculate the cutoff frequency results at $f_c = 16.91\text{GHz}$ (Table 6.2.2-1). In the next simulation we apply the CDM and the calculated cutoff frequency is $f_c = 17.13\text{GHz}$ (Table 6.2.2-1).

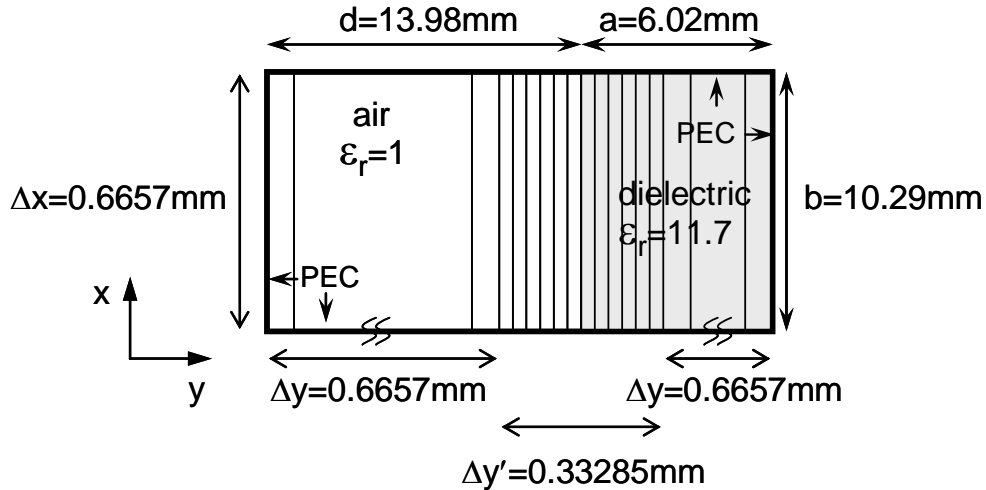


Fig. 6.2.2-7 Structure is discretized uniformly in the x -direction with $\Delta x = 0.6657\text{mm}$. In the y -direction, the original grid size of $\Delta y = 0.6657\text{mm}$ is refined to $\Delta y' = 0.33285\text{mm}$ in the vicinity of the grid boundary.

To verify the results of the first cutoff frequency and accuracy of different experiments, analytical expressions are utilized. The partially loaded dielectric slab rectangular waveguide can be analyzed in terms of normal modes of propagation based on the longitudinal-section magnetic (LSM) and longitudinal-section electric (LSE) modes. The axial and transverse components of the electric and magnetic field distribution are expressed in terms of either a magnetic-type or an electric-type vector potential. The vector potentials are selected in the transverse plane normal to the air and dielectric interface. The potentials are expanded in terms of a set of rectangular orthogonal functions. Enforcing the perfectly conducting and the air/dielectric media interface boundary conditions, the following analytical expressions for the cutoff frequencies for the two types of normal modes can be obtained. For LSE modes, the magnetic-type vector potential, Π_h , is given by

$$\Pi_h = a_y \Psi_h(x, y) e^{-j\beta z} \quad (6.2.2-3)$$

$$\Psi_h(x, y) = A \sin(hy) \cos\left(\frac{m\pi x}{b}\right) \quad 0 < y < d \quad (6.2.2-4)$$

$$\Psi_h(x, y) = B \sin(p(a-y)) \cos\left(\frac{m\pi x}{b}\right) \quad d < y < a \quad (6.2.2-5)$$

where m is an integer, and the parameters p and h are obtained from the following of transcendental equations

$$h \tan[p(a-d)] = -p \tan(hd) \quad (6.2.2-6)$$

$$p^2 = h^2 + (\varepsilon_r - 1)k^2 \quad (6.2.2-7)$$

Similarly for LSM modes, the electric-type vector potential, Π_e is given by

$$\Pi_e = a_y \Psi_e(x, y) e^{-j\beta z} \quad (6.2.2-8)$$

$$\Psi_e(x, y) = A \cos(hy) \sin\left(\frac{m\pi x}{b}\right) \quad 0 < y < d \quad (6.2.2-9)$$

$$\Psi_e(x, y) = B \cos(p(a-y)) \sin\left(\frac{m\pi x}{b}\right) \quad d < y < a \quad (6.2.2-10)$$

where m is an integer, and the parameters p and h are obtained from the following of transcendental equations

$$-p \tan[p(a-d)] = h\varepsilon_r \tan(hd) \quad (6.2.2-11)$$

$$p^2 = h^2 + (\varepsilon_r - 1)k^2 \quad (6.2.2-12)$$

The LSE mode and LSM mode cutoff frequencies are given by

$$f_c = \frac{c_0}{2\pi} \left[h^2 + \left(\frac{m\pi}{b} \right)^2 \right]^{1/2} \quad (6.2.2-13)$$

The first cutoff frequency for the TM polarization obtained from this analytical solution is compared with the cutoff frequencies calculated from previous experiments (Table 6.2.2-1). As we see, a non-uniform grid decreases the simulation time significantly and the CDM, which has the slight computational cost, improves the accuracy.

Table 6.2.2-1 Simulated cutoff frequencies and the analytical result.

Gridding Type	CDM	Grid Size (mm)	Total Simulation Time (sec.)	Cutoff Frequency (GHz)	Error Percentage (%)
Theory	N/A	N/A	N/A	17.68	N/A
Fine Mesh	N/A	0.1942	118	17.47	1.1878
Coarse Mesh	N/A	0.6657	3	16.82	4.8643
Coarse Mesh + Refined Mesh	No	0.6657	11	16.91	4.3552
Coarse Mesh + Refined Mesh	Yes	0.6657	12	17.13	3.1109

6.2.3 Three-dimensional Experiments

In this experiment we demonstrate the performance of CDM in a three-dimensional simulation domain. The simulation domain is a box with dimensions of $140mm \times 390mm \times 140mm$ (Fig. 6.2.3-1). We set the second order Higdon's absorbing boundary condition on the outer surfaces of our domain. The source is located at $(70mm, 50mm, 70mm)$; the monitor point is at $(70mm, 55mm, 70mm)$. The excitation is a Gaussian pulse

$$f(t) = \exp\left(-\frac{(t-t_d)^2}{\tau^2}\right)$$

with $t_d = 80ps$ and $\tau = 20ps$. The grid size is $\Delta = 0.5mm$ and the simulation result is called reference.

In the next step, we increase the grid size on the left side of grid boundary (in the y-direction) to $1mm$. The grid size on the right side of the grid boundary and all measurements are unchanged.

In Fig. 6.2.3-2, we show the *Normalized Error* (6.2.2-1) as a function of time for cases with and without the application of CDM. A significant reduction of reflection is observed.

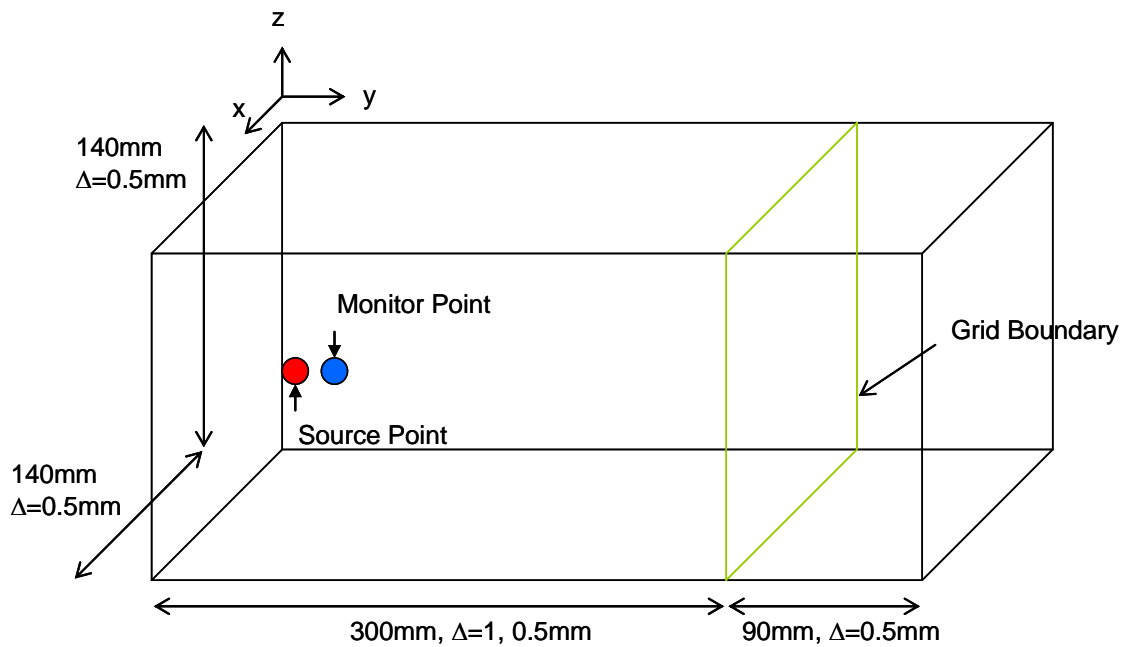


Fig. 6.2.3-1 Structure of the three-dimensional simulation domain.

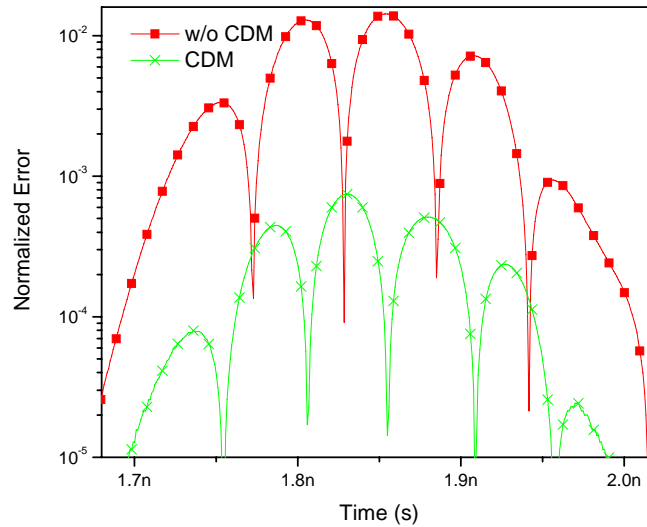


Fig. 6.2.3-2 Normalized error in the E-field as obtained using the standard FDTD interpolation scheme with and without CDM.

The next simulation compares the performance of CDM in the three-dimensional structures to analytical solutions. The simulated structure is a waveguide with an infinitely thin slot-line as center conductor (Fig. 6.2.3-3) [6-5]. This structure gives rise to the field singularities at the edges of the center conductor. The fields very close to the center conductor change rapidly and, therefore, a fine grid should be used to resolve these variations. This structure supports a TEM mode, therefore the impedance is well defined and can be used as an indicator of accuracy. As mentioned in [6-5], the dimensions are chosen such that the slot geometry corresponds to measurements typically used with Monolithic Millimeter-wave Integrated Circuits (MMIC's). For this structure, the characteristic impedance of the TEM mode can be derived analytically by conformal mapping and is $Z_c=94.2\Omega$ [6-5].

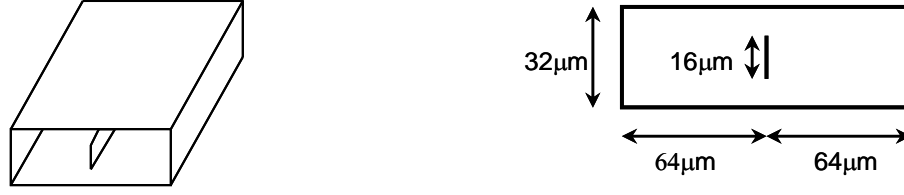


Fig. 6.2.3-3 Cross section of the waveguide with an infinitely thin slot-line as the center conductor. The exact impedance is $Z_c = 94.2\Omega$.

The cross section of the waveguide is $32\mu m \times 128\mu m$. The infinitely thin conducting slot has a height of $16\mu m$ and is located exactly in the center of the waveguide (Fig. 6.2.3-3). The structure is discretized uniformly in all directions with $\Delta x = \Delta y = \Delta z = 8\mu m$ (Fig. 6.2.3-4). The Perfect Electric Conductor (PEC) boundary condition is applied on waveguide's walls. The excitation is a Gaussian pulse

$$f(t) = \exp\left(-\frac{(t-t_d)^2}{\tau^2}\right)$$

where $t_d = 3ps$, $\tau = 1ps$ and is injected between the strip-line and the short face of the waveguide during simulation. Results are obtained by recording the temporal variations of voltage and current. Using the relation

$$V(t) = -\int \vec{E} \cdot d\vec{l} \quad (6.2.3-1)$$

the voltage between the waveguide and the center conductor is calculated by using the calculated electric fields in the y -direction (Fig. 6.2.3-4). The Ampere's law

$$I = \oint \vec{H} \cdot d\vec{l} \quad (6.2.3-2)$$

is used to calculate the current in the center conductor from the magnetic fields in the x - and y -directions. The FFT is then applied to convert the time domain data to the

frequency domain. The calculated characteristic impedance is $Z_c=72.35\Omega$ (Table 6.2.3-1).

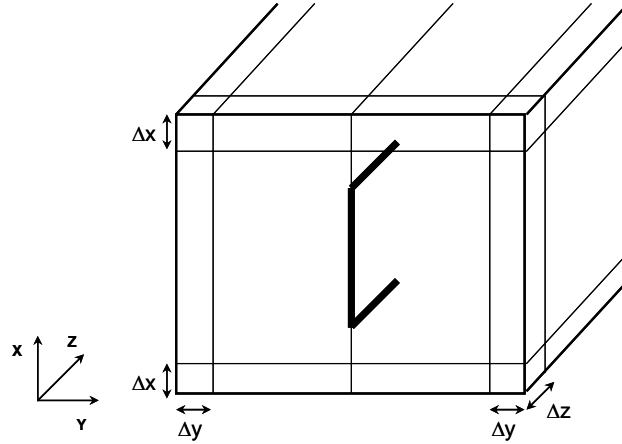


Fig. 6.2.3-4 Discretized structure of the waveguide with infinitely thin slot-line as center conductor.

In the next simulations, the grid sizes in the x - and y -directions are reduced to $4\mu m$, $2\mu m$, and $1\mu m$ but the grid size in the z -direction is kept unchanged at $\Delta z = 8\mu m$. The calculated characteristic impedances and the percentage of errors for each case are shown in Table 6.2.3-1.

Next, a non-uniform grid is used to resolve the structure more precisely. The coarse grid size of $\Delta x = \Delta y = 4\mu m$ is reduced to $\Delta x' = \Delta y' = 1\mu m$ around the strip-line conductor; $\Delta z = 8\mu m$ is unchanged (Fig. 6.2.3-5). The calculated characteristic impedance for the non-uniform grid is $Z_c=90.18\Omega$ (Table 6.2.3-1). As we compare it with uniform grid size of $\Delta x = \Delta y = 4\mu m$, the error percentage is reduced by approximately 7.75%. If we apply the CDM in the FDTD simulation of this structure, the calculated characteristic impedance is $Z_c=90.62\Omega$ (Table 6.2.3-1), which is an

improvement over the case without CDM. The calculated characteristic impedances are summarized in Table 6.2.3-1.

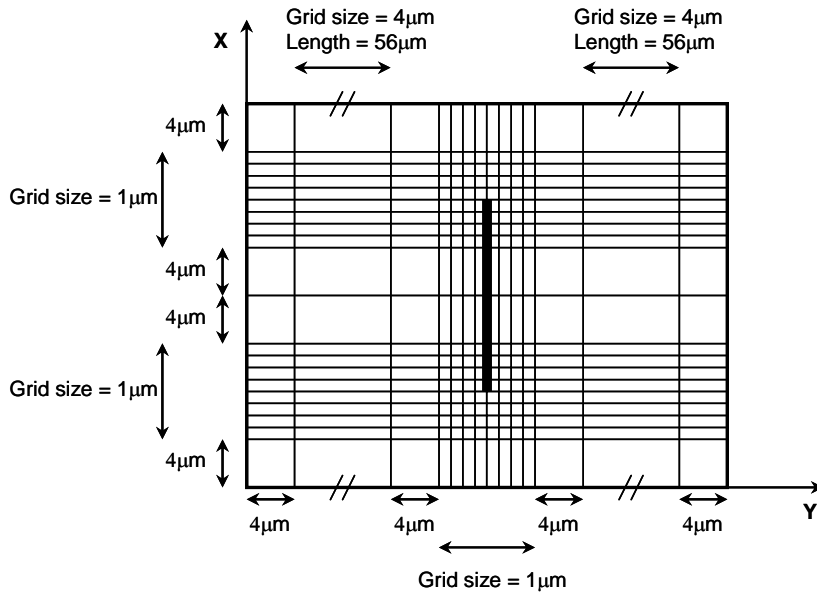


Fig. 6.2.3-5 Discretized structure of slot-line waveguide.

Table 6.2.3-1 Error in the calculated characteristic impedance using the uniform and non-uniform grids with and without CDM.

Method, Gridding Type	CDM	Main Grid Size (μm)	Characteristic Impedance (Ω)	Error Percentage (%)
Mode Matching, N/A	N/A	N/A	94.2	N/A
FDTD, Uniform	N/A	8	72.35	23.20
FDTD, Uniform	N/A	4	82.88	12.02
FDTD, Uniform	N/A	2	88.40	6.16
FDTD, Uniform	N/A	1	91.92	2.42
FDTD, Non-uniform	No	4	90.18	4.27
FDTD, Non-uniform	Yes	4	90.62	3.80

6.3 Analytical Investigation of CDM

6.3.1 Fundamental Modes of Propagation in the Numerical Solution: Advection Equation

In this section, using the same procedure as [6-7], we find the fundamental modes of propagation in numerical solution of the advection equation. Consider the one-dimensional advection equation

$$\frac{\partial U}{\partial t} + c \frac{\partial U}{\partial x} = 0 \quad (6.3.1-1)$$

If we use the finite-difference semi-discretization scheme, in which only the spatial derivative is approximated with a central difference, we have

$$\frac{du_n}{dt} = -c \left(\frac{u_{n+1} - u_{n-1}}{2\Delta} \right) \quad (6.3.1-2)$$

where the grid in the x -direction is uniform (Fig. 6.3.1-1) and

$$\{u_n(t)\} \cong \{U(x_n, t)\} \quad (6.3.1-3)$$

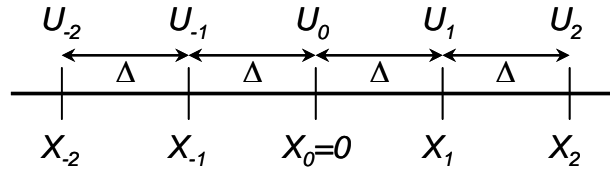


Fig. 6.3.1-1 Uniform grid.

Throughout this chapter we suppose that $\{u_n(t)\}$ are in L_2 space or square integrable, which means that L_2 norms

$$\left(\int_{-\infty}^{\infty} |u_n|^2 dt \right)^{1/2} \quad (6.3.1-4)$$

are finite. Therefore, the Fourier transforms $\{\hat{u}_n(\Omega)\}$ of the semi-discrete numerical solutions $\{u_n(t)\}$ exist and are defined as

$$\hat{u}_n(\Omega) = \int_{-\infty}^{\infty} u_n(t) e^{-i\Omega t} dt \quad (6.3.1-5)$$

Using the Fourier transform makes the investigation of properties of $\{\hat{u}(n)\}$ easier.

The Fourier-transform of (6.3.1-2) is

$$i\Omega \hat{u}_n = -c \left(\frac{\hat{u}_{n+1} - \hat{u}_{n-1}}{2\Delta} \right) \quad (6.3.1-6)$$

or

$$\hat{u}_{n+1} + 2i \left(\frac{\Omega\Delta}{c} \right) \hat{u}_n - \hat{u}_{n-1} = 0 \quad (6.3.1-7)$$

The solution of this recurrence equation can be achieved by seeking ‘fundamental’ solutions. Fundamental solutions are defined as the solutions that have a ratio

$$\frac{\hat{u}_{n+1}}{\hat{u}_n} \equiv \hat{E}(\Omega) \quad (6.3.1-8)$$

that is independent of n . It is worthy to note that $\hat{E}(\Omega)$ is a frequency domain representation of the standard space-shift operator E defined by the identity

$$u_{n+1} \equiv Eu_n \quad (6.3.1-9)$$

in the time domain. Substituting (6.3.1-8) into (6.3.1-7) results in

$$\left(\hat{E} + 2i \left(\frac{\Omega\Delta}{c} \right) - \hat{E}^{-1} \right) \hat{u}_n = 0 \quad (6.3.1-10)$$

Therefore, $\hat{E}(\Omega)$ must satisfy the characteristic equation

$$\hat{E}^2 + 2i\left(\frac{\Omega\Delta}{c}\right)\hat{E} - 1 = 0 \quad (6.3.1-11)$$

The roots of (6.3.1-11) are

$$\hat{E}_1(\Omega) = -i\left(\frac{\Omega\Delta}{c}\right) + \sqrt{1 - \left(\frac{\Omega\Delta}{c}\right)^2} \quad (6.3.1-12)$$

$$\hat{E}_2(\Omega) = -i\left(\frac{\Omega\Delta}{c}\right) - \sqrt{1 - \left(\frac{\Omega\Delta}{c}\right)^2} \quad (6.3.1-13)$$

which are called the ‘characteristic ratios’.

Therefore, the numerical solution of (6.3.1-2) can be expressed as

$$\{u_n(t)\} = \{p_n(t)\} + \{q_n(t)\} \quad (6.3.1-14)$$

which has two fundamental solutions. These two different fundamental solutions describe different propagation properties. One solution has the characteristic ratio of

$$\frac{\hat{p}_{n+1}(\Omega)}{\hat{p}_n(\Omega)} = \hat{E}_1(\Omega) = -i\left(\frac{\Omega\Delta}{c}\right) + \sqrt{1 - \left(\frac{\Omega\Delta}{c}\right)^2} \quad (6.3.1-15)$$

and describes the rightward propagating wave. It has a positive phase velocity [6-5] of

$$c_1(\Omega) = \frac{\Omega\Delta}{\arcsin(\Omega\Delta/c)} \quad (6.3.1-16)$$

and positive group velocity [6-5] of

$$v_1(\Omega) = c\sqrt{1 - \left(\frac{\Omega\Delta}{c}\right)^2} \quad (6.3.1-17)$$

The other solution has the characteristic ratio of

$$\frac{\hat{q}_{n+1}(\Omega)}{\hat{q}_n(\Omega)} = \hat{E}_2(\Omega) = -i\left(\frac{\Omega\Delta}{c}\right) - \sqrt{1 - \left(\frac{\Omega\Delta}{c}\right)^2} \quad (6.3.1-18)$$

and describes the leftward propagating wave. It has a positive phase velocity [6-5] of

$$c_2(\Omega) = \frac{\Omega\Delta}{\pi - \arcsin(\Omega\Delta/c)} \quad (6.3.1-19)$$

and negative group velocity [6-5] of

$$v_2(\Omega) = -c\sqrt{1 - \left(\frac{\Omega\Delta}{c}\right)^2} \quad (6.3.1-20)$$

6.3.2 Reflection from Grid Boundary: Standard Treatment of the Grid Boundary in Advection Equation

The reflection coefficient from the interface of two grids with different sizes is calculated in [6-5]. Since the same procedure is used to calculate the reflection coefficient from grid boundary when the CDM is applied, we briefly review the procedure discussed in [6-5].

Suppose that a non-uniform grid is used for discretizing the domain (Fig. 6.3.2-1) and the grid size changes from Δ to Δ' at interface $X_0=0$.

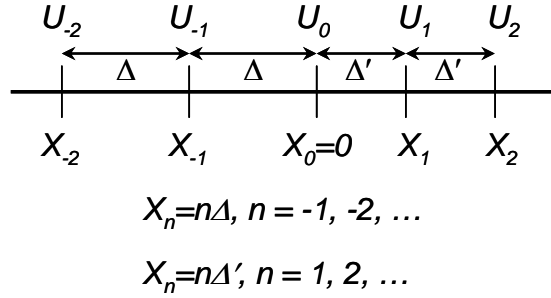


Fig. 6.3.2-1 Non-uniform grid.

Again, the finite-difference semi-discretization is used to approximate equation (6.3.1-2).

$$\frac{du_n}{dt} = -c \left(\frac{u_{n+1} - u_{n-1}}{2\Delta} \right), \text{ for } n = -1, -2, \dots \quad (6.3.2-1)$$

$$\frac{du_n}{dt} = -c \left(\frac{u_{n+1} - u_{n-1}}{2\Delta'} \right), \text{ for } n = 1, 2, \dots \quad (6.3.2-2)$$

At the interface $X_0=0$, the spatial derivative can be approximated as

$$\frac{du_0}{dt} = -c \left(\frac{u_1 - u_{-1}}{\Delta + \Delta'} \right) \quad (6.3.2-3)$$

We refer to (6.3.2-3) as the standard treatment of grid boundary. The CDM, which is a modified treatment of grid boundary, is described in section 6.3.3.

The numerical solution of the non-uniform grid in Fig. 6.3.2-1 can potentially have four fundamental solutions, which are the forward and backward solutions in $X < 0$, and forward and backward solutions in $X > 0$. If there is a wave propagating from left to right, reflection can only occur at the interface and only three fundamental solutions will exist (Fig. 6.3.2-2).

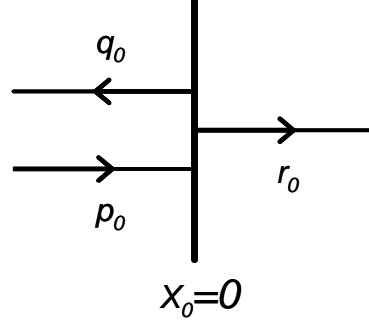


Fig. 6.3.2-2 Wave is propagating from left to right. In addition to the rightward waves in $X < 0$ and $X > 0$, there is a reflection from the interface in $X < 0$.

Let \hat{p}_0 , \hat{q}_0 , and \hat{r}_0 denote the fundamental solutions at the interface. The continuity at the interface $X_0=0$ gives

$$\hat{p}_0(\Omega) + \hat{q}_0(\Omega) = \hat{u}_0(\Omega) = \hat{r}_0(\Omega) \quad (6.3.2-4)$$

Also, we suppose that \hat{E}_1 , and \hat{E}_2 are the characteristic ratios corresponding to the solutions of $\{\hat{p}_n\}$, $\{\hat{q}_n\}$ to the left of origin defined by (6.3.1-15) and (6.3.1-18), respectively, and \hat{F} is the characteristic ratio of the solution of $\{\hat{r}_n\}$ to the right of origin given by

$$\frac{\hat{r}_{n+1}(\Omega)}{\hat{r}_n(\Omega)} = \hat{F}(\Omega) = -i \left(\frac{\Omega \Delta'}{c} \right) + \sqrt{1 - \left(\frac{\Omega \Delta'}{c} \right)^2} \quad (6.3.2-5)$$

The reflection coefficient is defined as

$$\rho(\Omega) = \frac{\hat{q}_0(\Omega)}{\hat{p}_0(\Omega)} \quad (6.3.2-6)$$

Using (6.3.2-4) and (6.3.2-6), the transmitted wave can be calculated as

$$\hat{r}_0(\Omega) = \hat{u}_0(\Omega) = (1 + \rho(\Omega))\hat{p}_0(\Omega) \quad (6.3.2-7)$$

To calculate the reflection coefficient, we express \hat{u}_1 and \hat{u}_{-1} in terms of \hat{p}_0 and \hat{q}_0 as

$$\hat{u}_1 = \hat{F}\hat{u}_0 = \hat{F}(\hat{p}_0 + \hat{q}_0) \quad (6.3.2-8)$$

$$\hat{u}_{-1} = \hat{E}_1^{-1}\hat{p}_0 + \hat{E}_2^{-1}\hat{q}_0 = -(\hat{E}_2\hat{p}_0 + \hat{E}_1\hat{q}_0) \quad (6.3.2-9)$$

The Fourier-transform of the semi-discretization equation at the interface $X_0=0$ (6.3.2-3) can be written as

$$i\Omega\hat{u}_0 = -c\left(\frac{\hat{u}_1 - \hat{u}_{-1}}{\Delta + \Delta'}\right) \quad (6.3.2-10)$$

By substituting (6.3.2-4), (6.3.2-8) and (6.3.2-9) into (6.3.2-10), we have

$$i\Omega(\hat{p}_0 + \hat{q}_0) = -c\left(\frac{\hat{F}(\hat{p}_0 + \hat{q}_0) + (\hat{E}_2\hat{p}_0 + \hat{E}_1\hat{q}_0)}{\Delta + \Delta'}\right) \quad (6.3.2-11)$$

which results in

$$\rho(\Omega) \equiv \frac{\hat{q}_0}{\hat{p}_0} = \frac{\sqrt{1 - \left(\frac{\Omega\Delta}{c}\right)^2} - \sqrt{1 - \left(\frac{\Omega\Delta'}{c}\right)^2}}{\sqrt{1 - \left(\frac{\Omega\Delta}{c}\right)^2} + \sqrt{1 - \left(\frac{\Omega\Delta'}{c}\right)^2}} \quad (6.3.2-12)$$

The reflection coefficient becomes particularly interesting if we apply group velocities. If $(\Omega\Delta/c) \leq 1$ and $(\Omega\Delta'/c) \leq 1$, the reflection coefficient can be written as

$$\rho = \frac{v_L - v_R}{v_L + v_R} \quad (6.3.2-13)$$

where v_L and v_R are the group velocities of waves propagating rightward in the left-side and right-side of the origin, respectively, which are

$$v_L = c \sqrt{1 - \left(\frac{\Omega \Delta}{c}\right)^2} \quad (6.3.2-14)$$

$$v_R = c \sqrt{1 - \left(\frac{\Omega \Delta'}{c}\right)^2} \quad (6.3.2-15)$$

6.3.3 Reflection from Grid Boundary: CDM Treatment of the Grid Boundary in Advection Equation

In this section, we calculate the reflection coefficient when the CDM is implemented at the interface. When the CDM is applied to the interface of two grids with different sizes, the semi-discretization approximation at the interface is modified from (6.3.2-3) to

$$\frac{du_0}{dt} = -c \left(\frac{1}{2} \frac{u'_1 - u_{-1}}{\Delta' + \Delta} + \frac{1}{2} \frac{u''_1 - u_{-1}}{\Delta'' + \Delta} \right) \quad (6.3.3-1)$$

(Fig. 6.3.3-1).

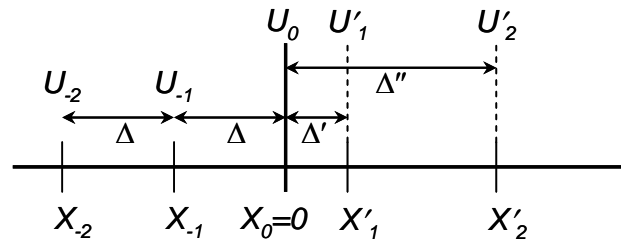


Fig. 6.3.3-1 Implementing the CDM on a non-uniform grid.

Using the same argument as in section 6.3.2, only three fundamental solutions exist (Fig. 6.3.2-2). The same procedure as in section 6.3.2 is used to calculate the

reflection coefficient. First, suppose that \hat{p}_0 , \hat{q}_0 , and \hat{r}_0 denote the fundamental solutions at the interface. The continuity at the interface $X_0=0$ gives

$$\hat{p}_0(\Omega) + \hat{q}_0(\Omega) = \hat{u}_0(\Omega) = \hat{r}_0(\Omega) \quad (6.3.3-2)$$

We assume that \hat{E}_1 , and \hat{E}_2 are the characteristic ratios corresponding to the solutions of $\{\hat{p}_n\}$, $\{\hat{q}_n\}$ to the left of the origin as defined by (6.3.1-15) and (6.3.1-18), respectively. Also, suppose that $\hat{F}_{\Delta'}$ and $\hat{F}_{\Delta''}$ are the characteristic ratios of rightward propagating solutions to the right of the origin with grid sizes of Δ' and Δ'' , respectively, given by

$$\hat{F}_{\Delta'}(\Omega) = -i\left(\frac{\Omega\Delta'}{c}\right) + \sqrt{1 - \left(\frac{\Omega\Delta'}{c}\right)^2} \quad (6.3.3-3)$$

$$\hat{F}_{\Delta''}(\Omega) = -i\left(\frac{\Omega\Delta''}{c}\right) + \sqrt{1 - \left(\frac{\Omega\Delta''}{c}\right)^2} \quad (6.3.3-4)$$

The reflection coefficient is defined as before

$$\rho(\Omega) = \frac{\hat{q}_0(\Omega)}{\hat{p}_0(\Omega)} \quad (6.3.3-5)$$

To calculate the reflection coefficient, we express \hat{u}'_1 , \hat{u}''_1 and \hat{u}_{-1} in terms of \hat{p}_0 , \hat{q}_0 as

$$\hat{u}'_1 = \hat{F}_{\Delta'}\hat{u}_0 = \hat{F}_{\Delta'}(\hat{p}_0 + \hat{q}_0) \quad (6.3.3-6)$$

$$\hat{u}''_1 = \hat{F}_{\Delta''}\hat{u}_0 = \hat{F}_{\Delta''}(\hat{p}_0 + \hat{q}_0) \quad (6.3.3-7)$$

$$\hat{u}_{-1} = \hat{E}_1^{-1}\hat{p}_0 + \hat{E}_2^{-1}\hat{q}_0 = -(\hat{E}_2\hat{p}_0 + \hat{E}_1\hat{q}_0) \quad (6.3.3-8)$$

The Fourier-transform of the modified semi-discretization equation at the interface $X_0=0$ using the CDM (6.3.3-1) can be written as

$$-i\Omega\hat{u}_0 = -c\left(\frac{1}{2}\frac{\hat{u}'_1 - \hat{u}_{-1}}{\Delta' + \Delta} + \frac{1}{2}\frac{\hat{u}''_1 - \hat{u}_{-1}}{\Delta'' + \Delta}\right) \quad (6.3.3-9)$$

By substituting (6.3.3-2), (6.3.3-6), (6.3.3-7) and (6.3.3-8) into (6.3.3-9), we have

$$-i\Omega(\hat{p}_0 + \hat{q}_0) = -c\left(\frac{1}{2}\frac{\hat{F}_{\Delta'}(\hat{p}_0 + \hat{q}_0) + (\hat{E}_2\hat{p}_0 + \hat{E}_1\hat{q}_0)}{\Delta + \Delta'} + \frac{1}{2}\frac{\hat{F}_{\Delta''}(\hat{p}_0 + \hat{q}_0) + (\hat{E}_2\hat{p}_0 + \hat{E}_1\hat{q}_0)}{\Delta + \Delta''}\right) \quad (6.3.3-10)$$

which results in

$$\rho(\Omega) = \frac{\hat{q}_0}{\hat{p}_0} = -\frac{i\Omega + \frac{1}{2}\frac{c}{\Delta + \Delta'}(\hat{E}_2 + \hat{F}_{\Delta'}) + \frac{1}{2}\frac{c}{\Delta + \Delta''}(\hat{E}_2 + \hat{F}_{\Delta''})}{i\Omega + \frac{1}{2}\frac{c}{\Delta + \Delta'}(\hat{E}_1 + \hat{F}_{\Delta'}) + \frac{1}{2}\frac{c}{\Delta + \Delta''}(\hat{E}_1 + \hat{F}_{\Delta''})}$$

or

$$\rho(\Omega) \equiv \frac{\hat{q}_0}{\hat{p}_0} = \frac{\frac{1}{\Delta + \Delta'}\left(\sqrt{1 - \left(\frac{\Omega\Delta}{c}\right)^2} - \sqrt{1 - \left(\frac{\Omega\Delta'}{c}\right)^2}\right) + \frac{1}{\Delta + \Delta''}\left(\sqrt{1 - \left(\frac{\Omega\Delta}{c}\right)^2} - \sqrt{1 - \left(\frac{\Omega\Delta''}{c}\right)^2}\right)}{\frac{1}{\Delta + \Delta'}\left(\sqrt{1 - \left(\frac{\Omega\Delta}{c}\right)^2} + \sqrt{1 - \left(\frac{\Omega\Delta'}{c}\right)^2}\right) + \frac{1}{\Delta + \Delta''}\left(\sqrt{1 - \left(\frac{\Omega\Delta}{c}\right)^2} + \sqrt{1 - \left(\frac{\Omega\Delta''}{c}\right)^2}\right)} \quad (6.3.3-11)$$

The reflection coefficient becomes particularly interesting if we, again, apply group velocities. If $(\Omega\Delta/c) \leq 1$, $(\Omega\Delta'/c) \leq 1$ and $(\Omega\Delta''/c) \leq 1$, the reflection coefficient can be written as

$$\rho = \frac{\frac{1}{\Delta + \Delta'}(v_L - v'_R) + \frac{1}{\Delta + \Delta''}(v_L - v''_R)}{\frac{1}{\Delta + \Delta'}(v_L + v'_R) + \frac{1}{\Delta + \Delta''}(v_L + v''_R)} \quad (6.3.3-12)$$

where v_L , v'_R , and v''_R are the group velocities of waves propagating rightward in the left-side of the origin, in the right-side of the origin with grid size of Δ' , and in the right-side of the origin with grid size of Δ'' , respectively, which are

$$v_L = c\sqrt{1 - \left(\frac{\Omega\Delta}{c}\right)^2} \quad (6.3.3-13)$$

$$v'_R = c \sqrt{1 - \left(\frac{\Omega \Delta'}{c}\right)^2} \quad (6.3.3-14)$$

$$v''_R = c \sqrt{1 - \left(\frac{\Omega \Delta''}{c}\right)^2} \quad (6.3.3-15)$$

6.3.4 Fundamental Modes of Propagation in the Numerical Solution: Leap-Frog Scheme of the Wave Equation

In this section, we investigate the fundamental modes of propagation of numerical solution of the wave equation using the leap-frog scheme. Consider the one-dimensional wave equation

$$\frac{\partial^2 U}{\partial t^2} - c^2 \frac{\partial^2 U}{\partial x^2} = 0 \quad (6.3.4-1)$$

The following equations are solved when the leap-frog scheme is used to solve the wave equation

$$\frac{\partial U}{\partial t} = c \frac{\partial V}{\partial x} \quad (6.3.4-2)$$

$$\frac{\partial V}{\partial t} = c \frac{\partial U}{\partial x} \quad (6.3.4-3)$$

If we use the finite-difference semi-discretization to approximate these equations, we have

$$\frac{du_j}{dt} = c \frac{v_{j+\frac{1}{2}} - v_{j-\frac{1}{2}}}{\bar{h}_j} \quad (6.3.4-4)$$

$$\frac{dv_{j+\frac{1}{2}}}{dt} = c \frac{u_{j+1} - u_j}{h_j} \quad (6.3.4-5)$$

where

$$h_j = X_{j+1} - X_j \quad (6.3.4-6)$$

$$\bar{h}_j = \frac{h_j + h_{j-1}}{2} \quad (6.3.4-7)$$

$\{u_j(t)\} \cong \{U(x_j, t)\}$, and $\{v_{j+1/2}(t)\} \cong \{V(x_{j+1/2}, t)\}$ (Fig. 6.3.4-1).

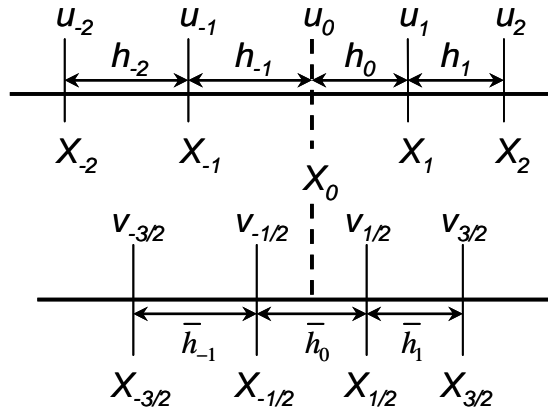


Fig. 6.3.4-1 Leap-frog scheme to solve the wave equation.

We suppose that $\{u_j(t)\}$ and $\{v_{j+1/2}(t)\}$ are in L_2 space, which means that L_2 norms

$$\left(\int_{-\infty}^{\infty} |u_j|^2 dt \right)^{1/2} \quad (6.3.4-8)$$

$$\left(\int_{-\infty}^{\infty} \left| v_{j+\frac{1}{2}} \right|^2 dt \right)^{1/2} \quad (6.3.4-9)$$

are finite. Therefore, the Fourier transforms $\hat{u}_j(\Omega)$ and $\hat{v}_{j+1/2}(\Omega)$ of the semi-discrete numerical solutions $\{u_j(t)\}$ and $\{v_{j+1/2}(t)\}$ exist and are defined as

$$\hat{u}_j(\Omega) = \int_{-\infty}^{\infty} u_j(t) e^{-i\Omega t} dt \quad (6.3.4-10)$$

$$\hat{v}_{j+\frac{1}{2}}(\Omega) = \int_{-\infty}^{\infty} v_{j+\frac{1}{2}}(t) e^{-i\Omega t} dt \quad (6.3.4-11)$$

The Fourier-transforms of (6.3.4-4) and (6.3.4-5) are

$$i\Omega \hat{u}_j = c \frac{\hat{v}_{j+\frac{1}{2}} - \hat{v}_{j-\frac{1}{2}}}{\bar{h}_j} \quad (6.3.4-12)$$

$$i\Omega \hat{v}_{j+\frac{1}{2}} = c \frac{\hat{u}_{j+1} - \hat{u}_j}{h_j} \quad (6.3.4-13)$$

or

$$\hat{v}_{j+\frac{1}{2}} - i \frac{\Omega}{c} \bar{h}_j \hat{u}_j - \hat{v}_{j-\frac{1}{2}} = 0 \quad (6.3.4-14)$$

$$\hat{v}_{j+\frac{1}{2}} = \frac{\hat{u}_{j+1} - \hat{u}_j}{i \frac{\Omega}{c} h_j} \quad (6.3.4-15)$$

Use (6.3.4-15) to calculate $\hat{v}_{j+1/2}$ and $\hat{v}_{j-1/2}$, and substitute them into (6.3.4-14).

After some manipulation, we have

$$\frac{1}{i \frac{\Omega}{c} h_j} \hat{u}_{j+1} - \left(\frac{1}{i \frac{\Omega}{c} h_j} + i \frac{\Omega}{c} \bar{h}_j + \frac{1}{i \frac{\Omega}{c} h_{j-1}} \right) \hat{u}_j + \frac{1}{i \frac{\Omega}{c} h_{j-1}} \hat{u}_{j-1} = 0 \quad (6.3.4-16)$$

First, we suppose that the grid is uniform, $h_j = \bar{h}_j = \Delta$, for all j 's (Fig. 6.3.4-2). Therefore (6.3.4-16) can be written as

$$\frac{1}{i\frac{\Omega}{c}\Delta}\hat{u}_{j+1} - \left(\frac{2}{i\frac{\Omega}{c}\Delta} + i\frac{\Omega}{c}\Delta \right)\hat{u}_j + \frac{1}{i\frac{\Omega}{c}\Delta}\hat{u}_{j-1} = 0 \quad (6.3.4-17)$$

or

$$\hat{u}_{j+1} - \left(2 - \frac{\Omega^2}{c^2}\Delta^2 \right)\hat{u}_j + \hat{u}_{j-1} = 0 \quad (6.3.4-18)$$

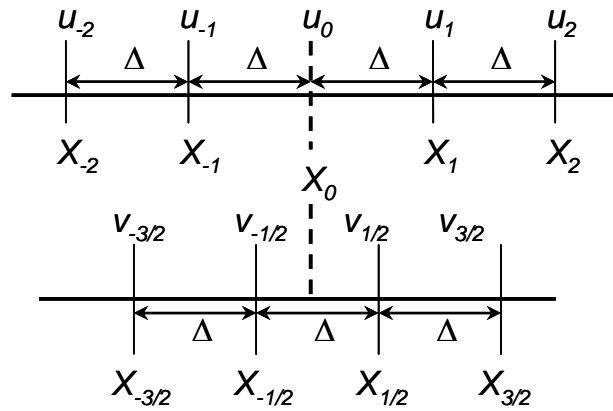


Fig. 6.3.4-2 Leap-frog scheme to solve the wave equation. A uniform grid is used.

The fundamental solutions of this recurrence equation can be found by substituting

$$\frac{\hat{u}_{j+1}}{\hat{u}_j} \equiv \hat{E}(\Omega)$$

in (6.3.4-18). The characteristic equation is

$$\hat{E}^2 - \left(2 - \frac{\Omega^2}{c^2}\Delta^2 \right)\hat{E} + 1 = 0 \quad (6.3.4-19)$$

and its characteristic ratios are

$$\hat{E}_1 = 1 - \frac{1}{2} \frac{\Omega^2}{c^2} \Delta^2 + \sqrt{\frac{1}{4} \frac{\Omega^4}{c^4} \Delta^4 - \frac{\Omega^2}{c^2} \Delta^2} \quad (6.3.4-20)$$

$$\hat{E}_2 = 1 - \frac{1}{2} \frac{\Omega^2}{c^2} \Delta^2 - \sqrt{\frac{1}{4} \frac{\Omega^4}{c^4} \Delta^4 - \frac{\Omega^2}{c^2} \Delta^2} \quad (6.3.4-21)$$

Therefore, we can conclude that the numerical solution of (6-3-4.1) can be expressed as

$$\{u_j(t)\} = \{p_j(t)\} + \{q_j(t)\} \quad (6.3.4-22)$$

which has two fundamental solutions. These two different fundamental solutions describe different propagation properties. One solution, which has the characteristic ratio of

$$\frac{\hat{p}_{j+1}(\Omega)}{\hat{p}_j(\Omega)} = \hat{E}_1(\Omega) = 1 - \frac{1}{2} \frac{\Omega^2}{c^2} \Delta^2 + \sqrt{\frac{1}{4} \frac{\Omega^4}{c^4} \Delta^4 - \frac{\Omega^2}{c^2} \Delta^2} \quad (6.3.4-23)$$

describes the rightward propagating wave. The other solution has the characteristic ratio of

$$\frac{\hat{q}_{j+1}(\Omega)}{\hat{q}_j(\Omega)} = \hat{E}_2(\Omega) = 1 - \frac{1}{2} \frac{\Omega^2}{c^2} \Delta^2 - \sqrt{\frac{1}{4} \frac{\Omega^4}{c^4} \Delta^4 - \frac{\Omega^2}{c^2} \Delta^2} \quad (6.3.4-24)$$

describes the leftward propagating wave.

6.3.5 Reflection from Grid Boundary: Standard Treatment of Grid Boundary in the Wave Equation

Here, we calculate the reflection coefficient from the interface of two grids with different sizes. Suppose the grid size changes from Δ to Δ' at interface $X_0=0$ (Fig. 6.3.5-1).

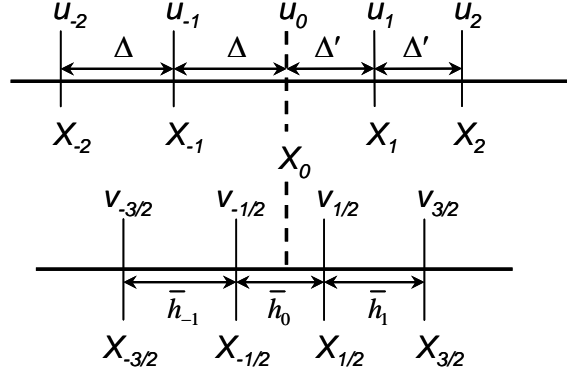


Fig. 6.3.5-1 Non-uniform grid in leap-frog scheme.

Using the same argument as in section 6.3.2, only three fundamental solutions exist (Fig. 6.3.2-2). The same procedure as section 6.3.2 is also used to calculate the reflection coefficient. First, suppose \hat{p}_0 , \hat{q}_0 , and \hat{r}_0 denote the fundamental solutions at the interface. The continuity at the interface $X_0=0$ gives

$$\hat{p}_0(\Omega) + \hat{q}_0(\Omega) = \hat{u}_0(\Omega) = \hat{r}_0(\Omega) \quad (6.3.5-1)$$

We assume that \hat{E}_1 , and \hat{E}_2 are the characteristic ratios corresponding to solutions \hat{p}_j , \hat{q}_j to the left of the origin as defined by (6.3.4-23) and (6.3.4-24), respectively. Also, suppose $\hat{F}_{\Delta'}$ is the characteristic ratio of the rightward propagating solution to the right of the origin with a grid size of Δ' , given by

$$\hat{F}_{\Delta'}(\Omega) = 1 - \frac{1}{2} \frac{\Omega^2}{c^2} \Delta'^2 + \sqrt{\frac{1}{4} \frac{\Omega^4}{c^4} \Delta'^4 - \frac{\Omega^2}{c^2} \Delta'^2} \quad (6.3.5-2)$$

The reflection coefficient, as defined before is

$$\rho(\Omega) = \frac{\hat{q}_0(\Omega)}{\hat{p}_0(\Omega)} \quad (6.3.5-3)$$

To calculate the reflection coefficient, we express \hat{u}_1 and \hat{u}_{-1} in terms of \hat{p}_0 and \hat{q}_0 as

$$\hat{u}_1 = \hat{F}\hat{u}_0 = \hat{F}(\hat{p}_0 + \hat{q}_0) \quad (6.3.5-4)$$

$$\hat{u}_{-1} = \hat{E}_1^{-1}\hat{p}_0 + \hat{E}_2^{-1}\hat{q}_0 = -(\hat{E}_2\hat{p}_0 + \hat{E}_1\hat{q}_0) \quad (6.3.5-5)$$

The Fourier-transform of the semi-discretization approximation (6.3.4-16) at the interface $X_0=0$ can be written as

$$\frac{1}{i\frac{\Omega}{c}h_0}\hat{u}_1 - \left(\frac{1}{i\frac{\Omega}{c}h_0} + i\frac{\Omega}{c}\bar{h}_0 + \frac{1}{i\frac{\Omega}{c}h_{-1}} \right)\hat{u}_0 + \frac{1}{i\frac{\Omega}{c}h_{-1}}\hat{u}_{-1} = 0$$

or

$$\frac{1}{h_0}\hat{u}_1 - \left(\frac{1}{h_0} - \frac{\Omega^2}{c^2}\bar{h}_0 + \frac{1}{h_{-1}} \right)\hat{u}_0 + \frac{1}{h_{-1}}\hat{u}_{-1} = 0 \quad (6.3.5-6)$$

By substituting (6.3.5-1), (6.3.5-4) and (6.3.5-5) into (6.3.5-6), we have

$$\frac{1}{h_0}\hat{F}(\hat{p}_0 + \hat{q}_0) - \left(\frac{1}{h_0} - \frac{\Omega^2}{c^2}\bar{h}_0 + \frac{1}{h_{-1}} \right)(\hat{p}_0 + \hat{q}_0) + \frac{1}{h_{-1}}(E_2\hat{p}_0 + E_1\hat{q}_0) = 0 \quad (6.3.5-7)$$

which results in

$$\rho(\Omega) = \frac{\hat{q}_0}{\hat{p}_0} = -\frac{\frac{\hat{E}_2 - 1}{h_{-1}} + \frac{\Omega^2}{c^2}\bar{h}_0 + \frac{\hat{F} - 1}{h_0}}{\frac{\hat{E}_1 - 1}{h_{-1}} + \frac{\Omega^2}{c^2}\bar{h}_0 + \frac{\hat{F} - 1}{h_0}} \quad (6.3.5-8)$$

6.3.6 Reflection from Grid Boundary: CDM Treatment of Grid Boundary in the Wave Equation

In this section, we calculate the reflection coefficient when the CDM is implemented at the interface (Fig. 6.3.6-1). At the interface of two grids with different sizes, the semi-discretization approximation (6.3.4-4) is modified to

$$\frac{du_0}{dt} = c \left(\frac{1}{2} \frac{v'_1 - v_{-\frac{1}{2}}}{\bar{h}'_0} + \frac{1}{2} \frac{v''_1 - v_{-\frac{1}{2}}}{\bar{h}''_0} \right) \quad (6.3.6-1)$$

If we take the Fourier-transform of (6.3.6-1), we have

$$i\Omega \hat{u}_0 = c \left(\frac{1}{2} \frac{\hat{v}'_1 - \hat{v}_{-\frac{1}{2}}}{\bar{h}'_0} + \frac{1}{2} \frac{\hat{v}''_1 - \hat{v}_{-\frac{1}{2}}}{\bar{h}''_0} \right)$$

or

$$\frac{1}{2\bar{h}'_0} \hat{v}'_1 + \frac{1}{2\bar{h}''_0} \hat{v}''_1 - i \frac{\Omega}{c} \hat{u}_0 - \frac{1}{2\bar{h}'_0} \hat{v}_{-\frac{1}{2}} - \frac{1}{2\bar{h}''_0} \hat{v}_{-\frac{1}{2}} = 0 \quad (6.3.6-2)$$

The Fourier-transforms of the following finite-difference semi-discretization approximations

$$\frac{dv'_1}{dt} = c \frac{u'_1 - u_0}{h_1} \quad (6.3.6-3)$$

$$\frac{dv''_1}{dt} = c \frac{u''_1 - u_0}{h_2} \quad (6.3.6-4)$$

$$\frac{dv_{-\frac{1}{2}}}{dt} = c \frac{u_0 - u_{-1}}{h_0} \quad (6.3.6-5)$$

are

$$i\Omega\hat{v}'_{\frac{1}{2}} = c \frac{\hat{u}'_1 - \hat{u}_0}{h_1} \quad (6.3.6-6)$$

$$i\Omega\hat{v}''_{\frac{1}{2}} = c \frac{\hat{u}''_1 - \hat{u}_0}{h_2} \quad (6.3.6-7)$$

$$i\Omega\hat{v}_{-\frac{1}{2}} = c \frac{\hat{u}_0 - \hat{u}_{-1}}{h} \quad (6.3.6-8)$$

Substituting (6.3.6-6), (6.3.6-7), and (6.3.6-8) into (6.3.6-2) results in

$$\frac{c}{2\bar{h}'_0} \frac{1}{i \frac{\Omega}{c} h_1} (\hat{u}'_1 - \hat{u}_0) + \frac{c}{2\bar{h}''_0} \frac{1}{i \frac{\Omega}{c} h_2} (\hat{u}''_1 - \hat{u}_0) - i\Omega\hat{u}_0 - \frac{c}{2} \left(\frac{1}{\bar{h}'_0} + \frac{1}{\bar{h}''_0} \right) \frac{1}{i \frac{\Omega}{c} h} (\hat{u}_0 - \hat{u}_{-1}) = 0 \quad (6.3.6-9)$$

which is the Fourier-transform of the CDM treatment of the interface.

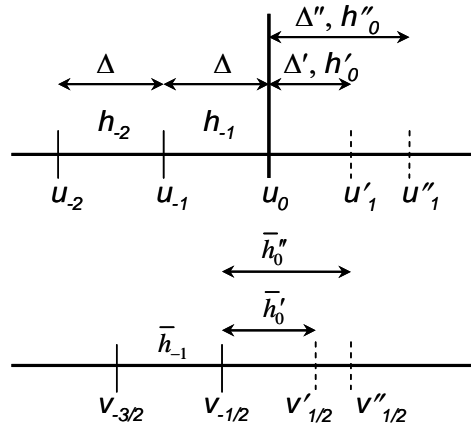


Fig. 6.3.6-1 Implementing CDM on a non-uniform grid.

Using the same argument as in section 6.3.2, only three fundamental solutions exist (Fig. 6.3.2-2). The same procedure as in section 6.3.2 is used to calculate the reflection coefficient. First, suppose \hat{p}_0 , \hat{q}_0 , and \hat{r}_0 denote the fundamental solutions at the interface. The continuity at the interface $X_0=0$ gives

$$\hat{p}_0(\Omega) + \hat{q}_0(\Omega) = \hat{u}_0(\Omega) = \hat{r}_0(\Omega) \quad (6.3.6-10)$$

We assume \hat{E}_1 , and \hat{E}_2 are the characteristic ratios corresponding to solutions \hat{p}_j , \hat{q}_j to the left of the origin defined by (6.3.4-23) and (6.3.4-24), respectively. Also, suppose that $\hat{F}_{\Delta'}$, and $\hat{F}_{\Delta''}$ are the characteristic ratios of the rightward propagating solutions to the right of the origin with grid sizes of Δ' and Δ'' , respectively, given by:

$$\hat{F}_{\Delta'}(\Omega) = 1 - \frac{1}{2} \frac{\Omega^2}{c^2} \Delta'^2 + \sqrt{\frac{1}{4} \frac{\Omega^4}{c^4} \Delta'^4 - \frac{\Omega^2}{c^2} \Delta'^2} \quad (6.3.6-11)$$

$$\hat{F}_{\Delta''}(\Omega) = 1 - \frac{1}{2} \frac{\Omega^2}{c^2} \Delta''^2 + \sqrt{\frac{1}{4} \frac{\Omega^4}{c^4} \Delta''^4 - \frac{\Omega^2}{c^2} \Delta''^2} \quad (6.3.6-12)$$

The reflection coefficient is defined as before

$$\rho(\Omega) = \frac{\hat{q}_0(\Omega)}{\hat{p}_0(\Omega)} \quad (6.3.6-13)$$

To calculate the reflection coefficient, we express \hat{u}'_1 , \hat{u}''_1 and \hat{u}_{-1} in terms of \hat{p}_0 and \hat{q}_0 as

$$\hat{u}'_1 = \hat{F}_{\Delta'} \hat{u}_0 = \hat{F}_{\Delta'} (\hat{p}_0 + \hat{q}_0) \quad (6.3.6-14)$$

$$\hat{u}''_1 = \hat{F}_{\Delta''} \hat{u}_0 = \hat{F}_{\Delta''} (\hat{p}_0 + \hat{q}_0) \quad (6.3.6-15)$$

$$\hat{u}_{-1} = \hat{E}_1^{-1} \hat{p}_0 + \hat{E}_2^{-1} \hat{q}_0 = -(\hat{E}_2 \hat{p}_0 + \hat{E}_1 \hat{q}_0) \quad (6.3.6-16)$$

By substituting (6.3.6-10), (6.3.6-14), (6.3.6-15) and (6.3.6-16) into (6.3.6-9),

we have

$$-i\Omega(\hat{p}_0 + \hat{q}_0) = -c \left(\frac{1}{2} \frac{\hat{F}_{\Delta'} (\hat{p}_0 + \hat{q}_0) + (\hat{E}_2 \hat{p}_0 + \hat{E}_1 \hat{q}_0)}{\Delta + \Delta'} + \frac{1}{2} \frac{\hat{F}_{\Delta''} (\hat{p}_0 + \hat{q}_0) + (\hat{E}_2 \hat{p}_0 + \hat{E}_1 \hat{q}_0)}{\Delta + \Delta''} \right) \quad (6.3.6-17)$$

which results in

$$\rho(\Omega) = \frac{\hat{q}_0}{\hat{p}_0} = - \frac{\frac{\hat{F}_{\Delta'} - 1}{h_1 \bar{h}_0'} + \frac{\hat{F}_{\Delta''} - 1}{h_2 \bar{h}_0''} + 2 \frac{\Omega^2}{c^2} + \frac{\hat{E}_2 - 1}{h_{-1}} \left(\frac{1}{\bar{h}_0'} + \frac{1}{\bar{h}_0''} \right)}{\frac{\hat{F}_{\Delta'} - 1}{h_1 \bar{h}_0'} + \frac{\hat{F}_{\Delta''} - 1}{h_2 \bar{h}_0''} + 2 \frac{\Omega^2}{c^2} + \frac{\hat{E}_1 - 1}{h_{-1}} \left(\frac{1}{\bar{h}_0'} + \frac{1}{\bar{h}_0''} \right)} \quad (6.3.6-18)$$

6.3.7 Results

To show the performance of CDM for the advection equation, we have compared the reflection coefficients from the interface of two grids with different sizes for the CDM and each individual complementary part of the CDM (Fig. 6.3.7-1). The frequency of the propagating wave is $1GHz$ and the grid size to the left of origin (Fig. 6.3.3-1) is $\Delta = \lambda/20$. The two complementary parts have grid sizes of $\Delta' = \Delta - \gamma \times \Delta$ (refined grid) and $\Delta'' = \Delta + \gamma \times \Delta$ (coarsened grid) for $0 < \gamma < 1$, which satisfy the complementary condition of $\Delta = (\Delta' + \Delta'')/2$. As we see in Fig. 6.3.7-1, the CDM has significantly reduced the reflection coefficient.

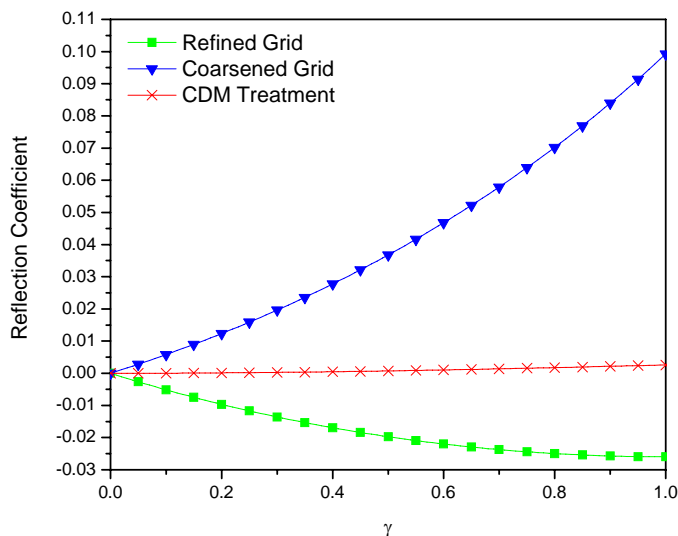


Fig. 6.3.7-1 Reflection coefficient of the advection equation at grid boundary; refined mesh, coarsened mesh, and the CDM treatment of grid boundary.

The performance of CDM for the wave equation is also demonstrated by plotting the reflection coefficients from the interface of two grids with different sizes for the CDM and each individual complementary part of CDM (Fig. 6.3.7-2). The frequency of the propagating wave is $1GHz$ and the grid size to the left of the origin (Fig. 6.3.4-1) is $\Delta=\lambda/20$. The two complementary parts have the grid sizes of $\Delta'=\Delta-\gamma\times\Delta$ (refined grid) and $\Delta''=\Delta+\gamma\times\Delta$ (coarsened grid) for $0<\gamma<1$, which satisfy the complementary condition of $\Delta=(\Delta'+\Delta'')/2$. As we see in Fig. 6.3.7-2, the CDM significantly reduces the reflection coefficient.

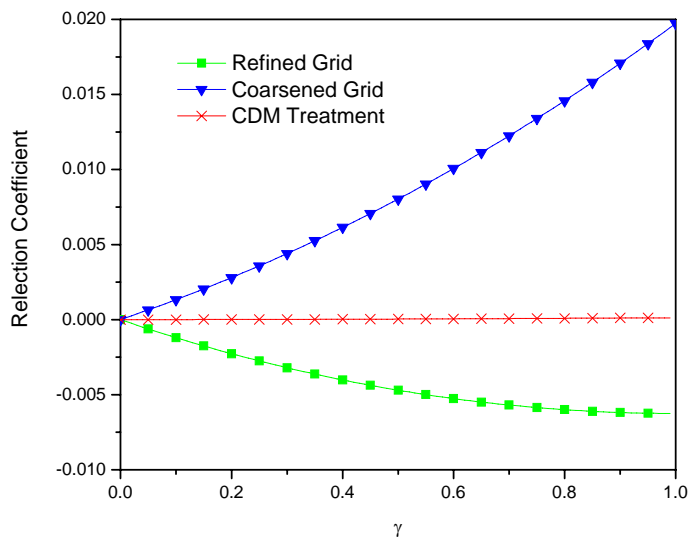


Fig. 6.3.7-2 Reflection coefficient of the wave equation at grid boundary; refined mesh, coarsened mesh, and the CDM treatment of grid boundary.

6.4 Implementing the CDM in the ADI-FDTD Method

We consider a two-dimensional domain which is discretized uniformly in the x -direction with the grid size of Δx and discretized non-uniformly in the y -direction, which the grid size changes from Δy to $\Delta y'$ at $j=j_0$ (Fig. 6.4-1). Using the same field positioning of the Yee scheme [6-2], the e_x lies on the interface of two domains with different grid sizes. The truncation error will be of the first order if the h_z field values of domains with different grid sizes are used to calculate the e_x .

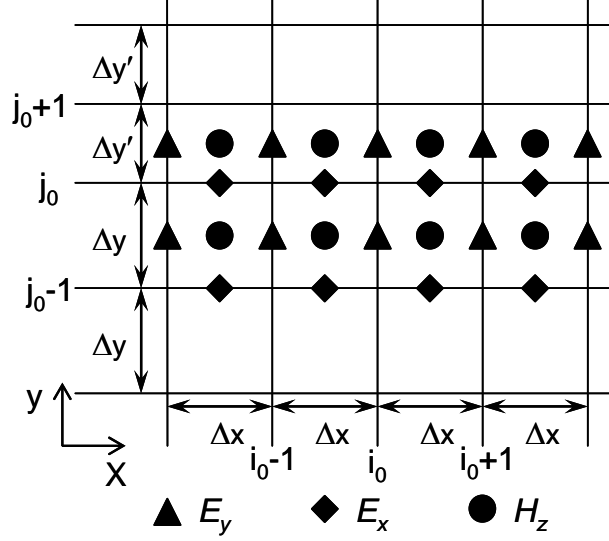


Fig. 6.4-1 Two-dimensional discretized domain. The grid is uniform in the x -direction with the grid size of Δx . The grid size is non-uniform in the y -direction and changes from Δy to $\Delta y'$ at $j=j_0$.

The updating equations for the ADI-FDTD method when uniform grids are used in the both x - and y -direction are

First Procedure (uniform grid in the x - and y -direction):

$$E_x|_{i+1/2,j}^{n+1/2} = E_x|_{i+1/2,j}^n + \frac{\Delta t/2}{\epsilon \Delta y} \left(H_z|_{i+1/2,j+1/2}^n - H_z|_{i+1/2,j-1/2}^n \right) \quad (6.4-1)$$

$$E_y|_{i,j+1/2}^{n+1/2} = E_y|_{i,j+1/2}^n - \frac{\Delta t/2}{\epsilon \Delta x} \left(H_z|_{i+1/2,j+1/2}^{n+1/2} - H_z|_{i-1/2,j+1/2}^{n+1/2} \right) \quad (6.4-2)$$

$$H_z|_{i+1/2,j+1/2}^{n+1/2} = H_z|_{i+1/2,j+1/2}^n + \frac{\Delta t/2}{\mu \Delta y} \left(E_x|_{i+1/2,j+1}^n - E_x|_{i+1/2,j}^n \right) - \frac{\Delta t/2}{\mu \Delta x} \left(E_y|_{i+1,j+1/2}^{n+1/2} - E_y|_{i,j+1/2}^{n+1/2} \right) \quad (6.4-3)$$

Second Procedure (uniform grid in the x - and y -direction)

$$E_x|_{i+1/2,j}^{n+1} = E_x|_{i+1/2,j}^{n+1/2} + \frac{\Delta t/2}{\epsilon\Delta y} \left(H_z|_{i+1/2,j_0+1/2}^{n+1} - H_z|_{i+1/2,j-1/2}^{n+1} \right) \quad (6.4-4)$$

$$E_y|_{i,j+1/2}^{n+1} = E_y|_{i,j+1/2}^{n+1/2} - \frac{\Delta t/2}{\epsilon\Delta x} \left(H_z|_{i+1/2,j+1/2}^{n+1/2} - H_z|_{i-1/2,j+1/2}^{n+1/2} \right) \quad (6.4-5)$$

$$H_z|_{i+1/2,j+1/2}^{n+1} = H_z|_{i+1/2,j+1/2}^{n+1/2} + \frac{\Delta t/2}{\mu\Delta y} \left(E_x|_{i+1/2,j+1}^{n+1} - E_x|_{i+1/2,j}^{n+1} \right) - \frac{\Delta t/2}{\mu\Delta x} \left(E_y|_{i+1,j+1/2}^{n+1/2} - E_y|_{i,j+1/2}^{n+1/2} \right) \quad (6.4-6)$$

As we see, equations (6.4-2) and (6.4-3) are implicit. We substitute (6.4-2) into (6.4-3) and it results in (6.4-3)'. Therefore, in the first procedure, E_x , H_z , and E_y are updated consecutively using (6.4-1), (6.4-3)', and (6.4-2).

$$\begin{aligned} & - \left(\frac{\Delta t^2}{4\mu\epsilon\Delta x^2} \right) H_z|_{i-1/2,j+1/2}^{n+1/2} + \left(1 + 2 \frac{\Delta t^2}{4\mu\epsilon\Delta x^2} \right) H_z|_{i+1/2,j+1/2}^{n+1/2} \\ & - \left(\frac{\Delta t^2}{4\mu\epsilon\Delta x^2} \right) H_z|_{i+3/2,j+1/2}^{n+1/2} = H_z|_{i+1/2,j+1/2}^n \quad (6.4-3)' \\ & - \frac{\Delta t}{2\mu\Delta x} \left(E_y|_{i+1,j+1/2}^n - E_y|_{i,j+1/2}^n \right) + \frac{\Delta t}{2\mu\Delta y} \left(E_x|_{i+1/2,j+1}^n - E_x|_{i+1/2,j}^n \right) \end{aligned}$$

In the second procedure, (6.4-4) and (6.4-6) are implicit. We substitute (6.4-4) into (6.4-6) and it results (6.4-6)'. Therefore, in the second procedure, E_y , H_z , and E_x are updated consecutively using (6.4-5), (6.4-6)', and (6.4-4).

$$\begin{aligned} & - \left(\frac{\Delta t^2}{4\mu\epsilon\Delta y^2} \right) H_z|_{i+1/2,j-1/2}^{n+1} + \left(1 + 2 \frac{\Delta t^2}{4\mu\epsilon\Delta y^2} \right) H_z|_{i+1/2,j+1/2}^{n+1} \\ & - \left(\frac{\Delta t^2}{4\mu\epsilon\Delta y^2} \right) H_z|_{i+1/2,j+3/2}^{n+1} = H_z|_{i+1/2,j+1/2}^{n+1/2} \quad (6.4-6)' \\ & - \frac{\Delta t}{2\mu\Delta x} \left(E_y|_{i+1,j+1/2}^{n+1/2} - E_y|_{i,j+1/2}^{n+1/2} \right) + \frac{\Delta t}{2\mu\Delta y} \left(E_x|_{i+1/2,j+1}^{n+1/2} - E_x|_{i+1/2,j}^{n+1/2} \right) \end{aligned}$$

Next, we suppose the grid size changes from Δy to $\Delta y'$ at $j=j_0$ (Fig. 6.4-1). Except for the following equations, the same updating equations as uniform grids should be used.

First Procedure (uniform grid in the x -direction, non-uniform grid in the y -direction without CDM)

1- Equation (6.4-1) at $j=j_0$ should be modified to

$$E_x|_{i+1/2, j_0}^{n+1/2} = E_x|_{i+1/2, j_0}^n + \frac{\Delta t/2}{\varepsilon(\Delta y + \Delta y')/2} \left(H_z|_{i+1/2, j_0+1/2}^n - H_z|_{i+1/2, j_0-1/2}^n \right) \quad (6.4-7)$$

Second Procedure (uniform grid in the x -direction, non-uniform grid in the y -direction without CDM)

1- Equation (6.4-4) at $j=j_0$ should be modified to

$$E_x|_{i+1/2, j_0}^{n+1} = E_x|_{i+1/2, j_0}^{n+1/2} + \frac{\Delta t/2}{\varepsilon(\Delta y + \Delta y')/2} \left(H_z|_{i+1/2, j_0+1/2}^{n+1} - H_z|_{i+1/2, j_0-1/2}^{n+1} \right) \quad (6.4-8)$$

2- Equation (6.4-6)' at $j=j_0-1$ should be modified to

$$\begin{aligned} & - \left(\frac{\Delta t^2}{4\mu\varepsilon\Delta y^2} \right) H_z|_{i+1/2, j_0-3/2}^{n+1} + \left(1 + \frac{\Delta t^2}{4\mu\varepsilon\Delta y^2} + \frac{\Delta t^2}{4\mu\varepsilon\Delta y(\Delta y + \Delta y')/2} \right) H_z|_{i+1/2, j_0-1/2}^{n+1} \\ & - \left(\frac{\Delta t^2}{4\mu\varepsilon\Delta y(\Delta y + \Delta y')/2} \right) H_z|_{i+1/2, j_0+1/2}^{n+1} = H_z|_{i+1/2, j_0-1/2}^{n+1} \\ & - \frac{\Delta t}{2\mu\Delta x} \left(E_y|_{i+1, j_0-1/2}^{n+1/2} - E_y|_{i, j_0-1/2}^{n+1/2} \right) + \frac{\Delta t}{2\mu\Delta y} \left(E_x|_{i+1/2, j_0}^{n+1/2} - E_x|_{i+1/2, j_0-1}^{n+1/2} \right) \end{aligned} \quad (6.4-9)$$

3- Equation (6.4-6)' at $j=j_0$ should be modified to

$$\begin{aligned} & - \left(\frac{\Delta t^2}{4\mu\varepsilon\Delta y'(\Delta y + \Delta y')/2} \right) H_z|_{i+1/2, j_0-1/2}^{n+1} \\ & + \left(1 + \frac{\Delta t^2}{4\mu\varepsilon\Delta y'^2} + \frac{\Delta t^2}{4\mu\varepsilon\Delta y'(\Delta y + \Delta y')/2} \right) H_z|_{i+1/2, j_0+1/2}^{n+1} \\ & - \left(\frac{\Delta t^2}{4\mu\varepsilon\Delta y'^2} \right) H_z|_{i+1/2, j_0+3/2}^{n+1} = H_z|_{i+1/2, j_0+1/2}^{n+1} \\ & - \frac{\Delta t}{2\mu\Delta x} \left(E_y|_{i+1, j_0+1/2}^{n+1/2} - E_y|_{i, j_0+1/2}^{n+1/2} \right) + \frac{\Delta t}{2\mu\Delta y'} \left(E_x|_{i+1/2, j_0+1}^{n+1/2} - E_x|_{i+1/2, j_0}^{n+1/2} \right) \end{aligned} \quad (6.4-10)$$

Next, we apply the CDM for updating the e_x values. Except for the following equations, the same updating equations as uniform grids should be used.

First Procedure (uniform grid in the x -direction, non-uniform grid in the y -direction with CDM)

1- Equation (6.4-1) at $j=j_0$ should be modified to

$$\varepsilon \frac{E_x|_{i+1/2, j_0}^{n+1/2} - E_x|_{i+1/2, j_0}^n}{\Delta t/2} = \frac{\frac{H_z|_{i+1/2, j_0+(2k_1-1)/2}^n - H_z|_{i+1/2, j_0-1/2}^n}{\frac{\Delta y}{2} + (2k_1-1)\frac{\Delta y'}{2}} + \frac{H_z|_{i+1/2, j_0+(2k_2-1)/2}^n - H_z|_{i+1/2, j_0-1/2}^n}{\frac{\Delta y}{2} + (2k_2-1)\frac{\Delta y'}{2}}}{2}$$

or

$$E_x|_{i+1/2, j_0}^{n+1/2} = E_x|_{i+1/2, j_0}^n + \frac{1}{2} \frac{\Delta t/2}{\varepsilon \left(\frac{\Delta y}{2} + (2k_1-1)\frac{\Delta y'}{2} \right)} \left(H_z|_{i+1/2, j_0+(2k_1-1)/2}^n - H_z|_{i+1/2, j_0-1/2}^n \right) + \frac{1}{2} \frac{\Delta t/2}{\varepsilon \left(\frac{\Delta y}{2} + (2k_2-1)\frac{\Delta y'}{2} \right)} \left(H_z|_{i+1/2, j_0+(2k_2-1)/2}^n - H_z|_{i+1/2, j_0-1/2}^n \right) \quad (6.4-11)$$

Second Procedure (uniform grid in the x -direction, non-uniform grid in the y -direction with CDM)

1- Equation (6.4-4) at $j=j_0$ should be modified to

$$\varepsilon \frac{E_x|_{i+1/2, j_0}^{n+1} - E_x|_{i+1/2, j_0}^{n+1/2}}{\Delta t/2} = \frac{H_z|_{i+1/2, j_0+(2k_1-1)/2}^{n+1} - H_z|_{i+1/2, j_0-1/2}^{n+1}}{\frac{\Delta y}{2} + (2k_1-1)\frac{\Delta y'}{2}} + \frac{H_z|_{i+1/2, j_0+(2k_2-1)/2}^{n+1} - H_z|_{i+1/2, j_0-1/2}^{n+1}}{\frac{\Delta y}{2} + (2k_2-1)\frac{\Delta y'}{2}}$$

2

or

$$E_x|_{i+1/2, j_0}^{n+1} = E_x|_{i+1/2, j_0}^{n+1/2} + \frac{1}{2} \frac{\Delta t/2}{\varepsilon \left(\frac{\Delta y}{2} + (2k_1-1)\frac{\Delta y'}{2} \right)} \left(H_z|_{i+1/2, j_0+(2k_1-1)/2}^{n+1} - H_z|_{i+1/2, j_0-1/2}^{n+1} \right) + \frac{1}{2} \frac{\Delta t/2}{\varepsilon \left(\frac{\Delta y}{2} + (2k_2-1)\frac{\Delta y'}{2} \right)} \left(H_z|_{i+1/2, j_0+(2k_2-1)/2}^{n+1} - H_z|_{i+1/2, j_0-1/2}^{n+1} \right) \quad (6.4-12)$$

2- Equation (6.4-6)' at $j=j_0-1$ should be modified to

$$-\left(\frac{\Delta t^2}{4\mu\varepsilon\Delta y^2} \right) H_z|_{i+1/2, j_0-3/2}^{n+1} + \left(1 + \frac{\Delta t^2}{4\mu\varepsilon\Delta y^2} + \alpha \frac{\Delta t}{2\mu\Delta y} + \beta \frac{\Delta t}{2\mu\Delta y} \right) H_z|_{i+1/2, j_0-1/2}^{n+1} - \left(\alpha \frac{\Delta t}{2\mu\Delta y} \right) H_z|_{i+1/2, j_0+(2k_1-1)/2}^{n+1} - \left(\beta \frac{\Delta t}{2\mu\Delta y} \right) H_z|_{i+1/2, j_0+(2k_2-1)/2}^{n+1} = H_z|_{i+1/2, j_0-1/2}^{n+1/2} - \frac{\Delta t}{2\mu\Delta x} \left(E_y|_{i+1, j_0-1/2}^{n+1/2} - E_y|_{i, j_0-1/2}^{n+1/2} \right) + \frac{\Delta t}{2\mu\Delta y} \left(E_x|_{i+1/2, j_0}^{n+1/2} - E_x|_{i+1/2, j_0-1}^{n+1/2} \right) \quad (6.4-13)$$

3- Equation (6.4-6)' at $j=j_0$ should be modified to

$$\left(-\alpha \frac{\Delta t}{2\mu\Delta y'} - \beta \frac{\Delta t}{2\mu\Delta y'} \right) H_z|_{i+1/2, j_0-1/2}^{n+1} + \left(1 + \frac{\Delta t^2}{4\mu\varepsilon\Delta y'^2} \right) H_z|_{i+1/2, j_0+1/2}^{n+1} - \left(\frac{\Delta t^2}{4\mu\varepsilon\Delta y'^2} \right) H_z|_{i+1/2, j_0+3/2}^{n+1} + \alpha \frac{\Delta t}{2\mu\Delta y'} H_z|_{i+1/2, j_0+(2k_1-1)/2}^{n+1} + \beta \frac{\Delta t}{2\mu\Delta y'} H_z|_{i+1/2, j_0+(2k_2-1)/2}^{n+1} = H_z|_{i+1/2, j_0+1/2}^{n+1/2} - \frac{\Delta t}{2\mu\Delta x} \left(E_y|_{i+1, j_0+1/2}^{n+1/2} - E_y|_{i, j_0+1/2}^{n+1/2} \right) + \frac{\Delta t}{2\mu\Delta y'} \left(E_x|_{i+1/2, j_0+1}^{n+1/2} - E_x|_{i+1/2, j_0}^{n+1/2} \right) \quad (6.4-14)$$

where

$$\alpha = \frac{1}{2} \frac{\Delta t}{2\varepsilon \left(\frac{\Delta y}{2} + (2k_1-1)\frac{\Delta y'}{2} \right)} \quad (6.4-15)$$

$$\vec{h} = \vec{h}_1 + \alpha \vec{h}_2 \quad (6.4-26)$$

where

$$\alpha = \frac{\vec{v}_2^T \vec{h}_1}{1 - \vec{v}_2^T \vec{h}_2} \quad (6.4-27)$$

Instead of solving (6.4-17), the auxiliary problems in (6.4-24) and (6.4-25) can be efficiently solved. Since \vec{v}_1 is a constant vector, we solve (6.4-25) once and store the solution for future usage. In each implicit update, only (6.4-24) needs to be solved and this requires $(5n-4)$ operations. By noticing the form of \vec{v}_2 , evaluating (6.4-27) requires eight arithmetic operations. The operation count, in addition to Gaussian elimination, which is introduced by (6.4-26) and (6.4-27), is $(2n + 8)$. Therefore, for each implicit update the total operation count of the ADI-FDTD method with CDM is $7n+4$. Therefore, the efficiency of the ADI-FDTD method is well preserved.

6.4.1 Numerical Experiments

Here, we apply the CDM in the ADI-FDTD method to simulate a two-dimensional structure having dimensions of $60mm \times 60mm$. First, we consider a uniform grid in the entire computational domain with the grid size of $\Delta x = \Delta y = 1mm$ (Fig. 6.4.1-1). A z -polarized current source is positioned at $(30mm, 28mm)$ and the monitor point is selected at $(30mm, 30mm)$. Since we look at a very short time interval to extract the reflection from the interface and to remove the complexity of implementing of ABC, we used perfect electric conductor (PEC) as the terminating planes. The temporal excitation is a Gaussian pulse, given by

$$f(t) = \exp\left(-\frac{(t-t_0)^2}{\tau^2}\right)$$

with $t_0=250ps$ and $\tau=50ps$. The numerical results obtained for this case will be considered as the reference solution (H_z^{ref}).

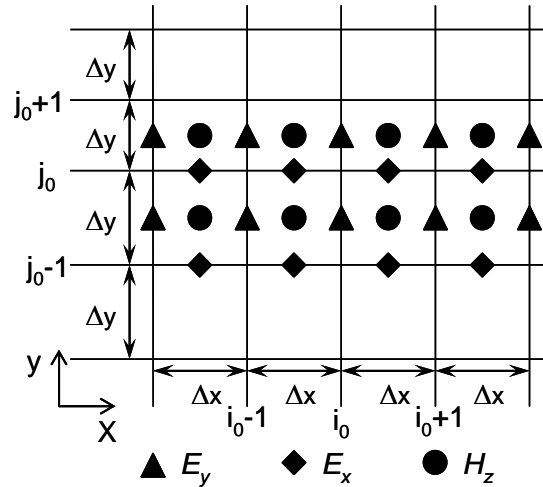


Fig. 6.4.1-1 Simulated structure as reference. The grid size is uniform ($\Delta x = \Delta y = 1mm$) throughout the computational domain.

Next, we solve the same problem, but this time we decrease the grid size in the y-direction from $\Delta y = 1mm$ to $\Delta y' = 0.5, 0.25$ and $0.125mm$ corresponding to reduction ratios of 1:2, 1:4 and 1:8 as shown in Fig. 6.4.1-2. The grid size in the x-direction, the locations of the source and monitor point, and the excitation pulse are left unchanged.

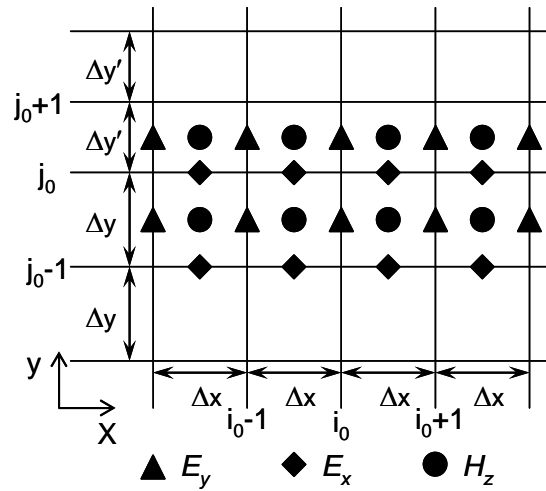


Fig. 6.4.1-2 Simulated structure with different grid sizes. The grid size in the y -direction changes from $\Delta y=1mm$ to $\Delta y'=0.5, 0.25, 0.125mm$ at $j_0=32mm$.

In Fig. 6.4.1-3, we show the *Normalized Error* (6.2.2-1) as a function of time for cases with and without CDM. A significant reduction of error is observed. Most importantly, it is observed that the error resulting from the application of CDM is practically independent of the mesh reduction ratio.

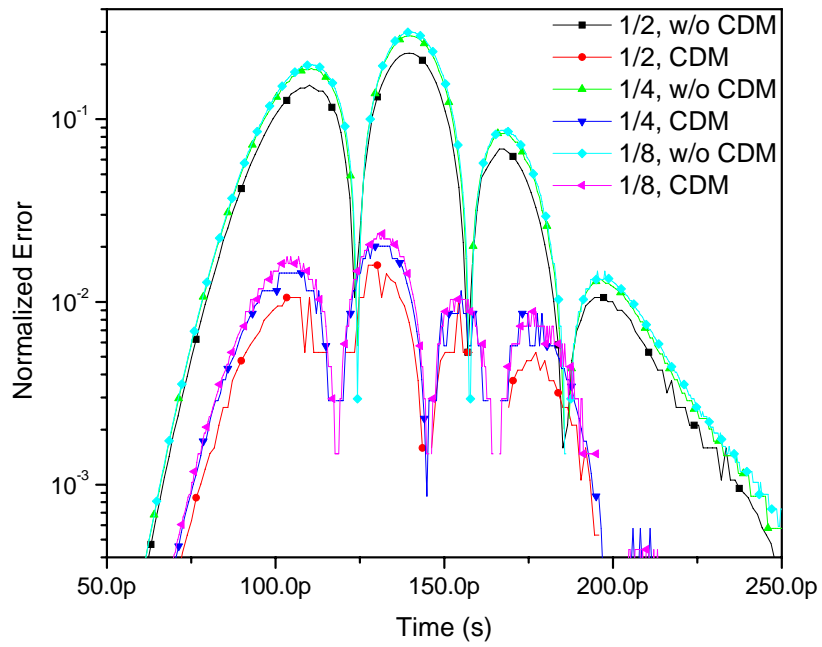


Fig. 6.4.1-3 Normalized error in the H -field as obtained using the ADI-FDTD method with and without CDM.

Chapter 7 **Conclusions and Future Work**

7.1 Conclusions

In this work, first, we studied the stability of high-order Absorbing Boundary Conditions (ABC) when applied in the Alternating Direction Implicit Finite-Difference Time-Domain (ADI-FDTD) method. We demonstrated that the high-order Higdon's ABCs are unstable. The high-order COM also became unstable when the Gaussian excitation was applied. Using the Z-transform, we demonstrated that an excitation with zero frequency content causes instability in the high-order COM.

The Complementary Derivatives Method (CDM) was introduced as a second-order accurate interpolation scheme applicable to Finite-Difference methods. Several experiments demonstrated the performance of CDM on reducing the reflection from boundary of two domains having different grid sizes. Consequently, more accurate results for resonant frequencies and characteristic impedances of different experiments were obtained using the CDM. The CDM was applied to calculation of the reflection coefficient of the advection and wave equations at the grid boundary. The CDM resulted in significant reduction in the reflection coefficients.

Next, we derived the fundamental modes of propagation in the numerical solution of the wave equation using the leap-frog scheme. We calculated the reflection coefficient of the wave equation at the grid boundary when the CDM was applied and compared it with the reflection coefficient in a standard treatment of grid boundary. The CDM, again, reduced the reflection coefficient at the grid boundary considerably.

Finally, the CDM was applied to the ADI-FDTD method. By employing the Sherman-Morrison formula, we retained the numerical efficiency of the conventional ADI-FDTD method when the CDM treatment was applied at the grid boundary. Numerical experiments using the ADI-FDTD method showed that the CDM can be effective in reducing spurious reflections at the grid boundary.

7.2 Future Work

The COM is a versatile mesh truncation scheme and simple to implement. The COM has shown its performance in the absorption of evanescent waves in waveguides and annihilating artificial reflections arising from the truncation of the computational domain. The COM must be modified to be implemented as a stable high-order accurate ABC to terminate open-region problems. The Z-transform can be used as a practical tool to analyze and improve the stability of the COM.

Also, we calculated the reflection coefficients of the advection and wave equations at the grid boundary with and without CDM and compared them numerically. The analytical comparison and demonstration of the better performance of the CDM treatment of the grid boundary to standard treatment can be the subject of further investigation.

Bibliography

Chap.1

- [1] K. S. Yee, "Numerical solution of initial boundary value problems involving Maxwell's equations in isotropic media," *IEEE Trans. Antenna Propagat.*, vol. AP-14, pp. 302-307, May 1966.
- [2] A. Taflove and S. C. Hagness, *Computational Electrodynamics: The Finite-Difference Time-Domain Method*, 3rd ed., *Artech House Publishers*, 2005.
- [3] F. Zheng, Z. Chen, J. Zhang, "A finite-difference time-domain method without the courant stability condition," *IEEE Microwave and Guided Wave Letters*, Vol. 9, No. 11, Nov. 1999, pp. 441-443.
- [4] T. Namiki, "A new FDTD algorithm based on alternating direction implicit method," *IEEE Trans. Microwave Theory Tech.*, vol. 47, pp. 2003-2007, Oct. 1999.
- [5] B. Engquist and A. Majada, "Radiation boundary conditions for the numerical simulation of waves," *Math. Comput.*, vol.31, no. 139, pp. 629-651, 1977.
- [6] R. L. Higdon, "Absorbing boundary conditions for difference approximations to the multidimensional wave equation," *Math. Comput.*, vol. 47, no. 176, pp. 437-459, Oct. 1986.
- [7] R. L. Higdon, "Radiation boundary conditions for elastic wave propagation," *SIAM J. Numer. Anal.*, vol. 27, no. 4, pp. 831-870, Aug. 1990.
- [8] O. M. Ramahi, "Stability of absorbing boundary conditions," *IEEE Trans. Antennas Propagat.*, vol. 47, no. 4, pp. 593-599, 1999.

- [9] O. M. Ramahi, "Application of the complementary operator method to the finite-difference time-domain solution of the three-dimensional radiation problem," *Microwave Opt. Technol. Lett.*, vol. 9, no. 3, pp. 147-149, June 1995.
- [10] O. M. Ramahi, "Complementary operators: A method to annihilate artificial reflections arising from the truncation of the computational domain in the solution of partial differential equations," *IEEE Trans. Antennas Propagat.*, vol. 43, pp. 697-704, July 1995.
- [11] O. M. Ramahi, "Complementary boundary operators for wave propagation problems," *J. Computat. Phys.*, vol. 133, pp. 113-128, 1997.
- [12] D. Sheen, "Numerical Modeling of Microstrip Circuits and Antennas," *Ph.D. Dissertation*, MIT, Cambridge, MA, June 1991.
- [13] C. F. Lee, "Finite Difference Method for Electromagnetic Scattering Problems," *Ph.D. Dissertation*, MIT, Cambridge, MA, June 1990.
- [14] K. Li, C. F. Lee, S. Y. Poh, R. T. Shin, and J. A. Kong, "Application of FDTD method to analysis of electromagnetic radiation from VLSI heatsink configuration," *IEEE Trans. Electromagnetic Compatibility*, vol. 35, pp. 204-214, May 1993.
- [15] S. Xiao, and R. Vahldieck, "An improved 2D-FDTD algorithm for hybrid mode analysis of quasi-planar transmission lines," *IEEE MTT-S digest*, vol. 1, pp. 421-424, 1993.
- [16] H. Jiang, and H. Arai, "3D-FDTD analysis by using non-uniform mesh," *IEEE ICMMT Proc.*, pp. 947-950, 1998.

- [17] T. Namiki, and K. Ito, "Accuracy improvement technique applied to non-uniform FDTD cells using high-order implicit scheme," *IEEE AP-S Proc.*, vol. 1, pp. 56-59, 2001.
- [18] M. Okoniewski, E. Okoniewska and M. A. Stuchly, "Three-dimensional subgridding algorithm for FDTD," *IEEE Trans. Antennas Propagat.*, Vol. 45, No. 3, pp. 422-429, March 1997.
- [19] W. Heinrich, K. Beilenhoff, P. Mezzanotte, and L. Roselli, "Optimum mesh grading for finite-difference method," *IEEE Trans. on Microwave Theory Tech.*, vol. 44, pp. 1569-1574, Sept. 1996.
- [20] D. Choi, J. D. Brown, B. Imbirida, J. Centrella, and P. MacNeice, "Interface conditions for wave propagation through mesh refinement boundaries," *J. Comput. Phys.*, Vol. 193, No. 2, pp. 398-425, 2004.
- [21] G. Chesshire, and W. D. Henshaw, "Composite overlapping meshes for the solution of partial differential equations," *J. Comput. Phys.*, Vol. 90, No. 1, pp. 1-64, 1990.
- [22] W. D. Henshaw, and D. W. Schwendeman, "An adaptive numerical scheme for high-speed reactive flow on overlapping grids," *J. Comput. Phys.*, Vol. 191, No. 2, pp. 420-447, 2003.

Chap. 2

- [1] T. Namiki, "A new FDTD algorithm based on alternating direction implicit method," *IEEE Trans. Microwave Theory Tech.*, vol. 47, pp. 2003-2007, Oct. 1999.

- [2] F. Zheng, Z. Chen, and J. Zhang, "A finite-difference time-domain method without the courant stability condition," *IEEE Microwave and Guided Wave Letters*, Vol. 9, No. 11, pp. 441-443, Nov. 1999.
- [3] T. Namiki, "3-D ADI-FDTD method-unconditionally stable time-domain algorithm for solving full vector Maxwell's equations," *IEEE Trans. on Microwave Theory and Techniques*, Vol. 48, No. 10, pp. 1743-1748, Oct. 2000.
- [4] F. Zheng, Z. Chen, and J. Zhang, "Toward the development of a three-dimensional unconditionally stable finite-difference time-domain method," *IEEE Trans. on Microwave Theory and Techniques*, Vol. 48, No. 9, pp. 1550-1558, Sept. 2000.
- [5] S. W. Staker, C. L. Holloway, A. U. Bhohe, and M. Piket-May, "Alternating-Direction Implicit (ADI) formulation of the Finite-Difference Time-Domain (FDTD) method: algorithm and material dispersion implementation," *IEEE Trans. on Electromagnetic Compatibility*, Vol. 45, No. 2, pp. 156-166, May 2003.
- [6] G. Sun, and C. W. Trueman, "Some fundamental characteristics of the one-dimensional alternating-direction-implicit finite-difference time-domain method," *IEEE Trans. on Electromagnetic Compatibility*, Vol. 52, No. 1, pp. 46-52, Jan 2004.
- [7] S. G. Garcia, R. G. Rubio, A. R. Bretones, and R. G. Martin, "Extension of the ADI-FDTD method to Debye media," *IEEE Trans. on Antennas and Propagation*, Vol. 51, No. 11, pp. 3183-3186, Nov. 2003.
- [8] X. T. Dong, N. V. Venkatarayalu, B. Guo, W. Y. Yin, and W. B. Gan, "General formulation of unconditionally stable ADI-FDTD method in linear

dispersive media,” *IEEE Trans. on Microwave Theory and Techniques*, Vol. 52, No. 1, pp. 170-174, Jan. 2004.

[9] T. Namiki, and K. Ito, “Investigation of numerical errors of the two-dimensional ADI-FDTD method,” *IEEE Trans. on Microwave Theory and Techniques*, Vol. 48, No. 11, pp. 1950-1956, Nov. 2000.

[10] F. Zheng, and Z. Chen, “Numerical dispersion analysis of the unconditionally stable 3-D ADI-FDTD method,” *IEEE Trans. on Microwave Theory and Techniques*, Vol. 49, No. 5, pp. 1006-1009, May 2001.

[11] M. Darms, R. Schuhmann, H. Spachmann, and T. Weiland, “Dispersion and asymmetry effects of ADI-FDTD,” *IEEE Microwave and Wireless Components Letters*, Vol. 12, No. 12, pp. 491-493, Dec. 2002.

[12] A. P. Zhao, “Analysis of the numerical dispersion of the 2-D alternating-direction implicit FDTD method,” *IEEE Trans. on Microwave Theory and Techniques*, Vol. 50, No. 4, pp. 1156-1164, April 2002.

[13] G. Sun, and C. W. Trueman, “Analysis and numerical experiments on the numerical dispersion of two-dimensional ADI-FDTD,” *IEEE Antennas and Wireless Propagation Letters*, Vol. 2, pp. 78-81, 2003.

[14] S. Ju, H. Kim, and H. H. Kim, “A study of the numerical dispersion relation for the 2-D ADI-FDTD method,” *IEEE Microwave and Wireless Components Letters*, Vol. 13, No. 9, pp. 405-407, Sept. 2003.

[15] M. Wang, Z. Wang, and J. Chen, “A parameter optimized ADI-FDTD method,” *IEEE Antennas and Wireless Propagation Letters*, Vol. 2, pp. 118-121, 2003.

- [16] A. P. Zhao, "Improvement on the numerical dispersion of 2-D ADI-FDTD with artificial anisotropy," *IEEE Microwave and Wireless Components Letters*, Vol. 14, No. 6, pp. 292-294, June 2004.
- [17] H. Zheng, and K. W. Leung, "An efficient method to reduce the numerical dispersion in the ADI-FDTD," *IEEE Trans. on Microwave Theory and Techniques*, Vol. 53, No. 7, pp. 2295-2301, July 2005.
- [18] D. L. Sounas, N. V. Kantartzis, and T. D. Tsiboukis, "Optimized ADI-FDTD analysis of circularly polarized microstrip and dielectric resonator antennas," *IEEE Microwave and Wireless Components Letters*, Vol. 16, No. 2, pp. 63-65, Feb. 2006.
- [19] S. G. Garcia, T. Lee, and S. C. Hagness, "On the accuracy of the ADI-FDTD method," *IEEE Antennas and Wireless Propagation Letters*, Vol. 1, pp. 31-34, 2002.
- [20] I. Ahmed, Z. Chen, "Error reduced ADI-FDTD methods," *IEEE Antennas and Wireless Propagation Letters*, Vol. 4, pp. 323-325, 2005.
- [21] S. Wang, F. L. Teixeira, and J. Chen, "An iterative ADI-FDTD with reduced splitting error," *IEEE Microwave and Wireless Components Letters*, Vol. 15, No. 2, pp. 92-94, Feb. 2005.
- [22] S. Wang, and J. Chen, "A performance study of the iterative ADI-FDTD method," *IEEE Trans. on Antennas and Propagation*, Vol. 53, No. 10, pp. 3413-3417, Oct. 2005.
- [23] S. Wang, and J. Chen, "Pre-iterative ADI-FDTD method for conductive medium," *IEEE Trans. on Microwave Theory and Techniques*, Vol. 53, No. 6, pp. 1913-1918, June 2005.

- [24] S. Wang, "On the current source implementation for the ADI-FDTD method," *IEEE Microwave and Wireless Components Letters*, Vol. 14, No. 11, pp. 513-515, Nov. 2004.
- [25] S. G. Garcia, A. R. Bretones, R. G. Martin, and S. C. Hagness, "Accurate implementation of current sources in the ADI-FDTD scheme," *IEEE Antennas and Wireless Propagation Letters*, Vol. 3, pp. 141-144, 2004.
- [26] B. Donderici, and F. Teixeira, "Symmetric source implementation for the ADI-FDTD method," *IEEE Trans. on Antennas and Propagation*, Vol. 53, No. 4, pp. 1562-1565, April 2005.
- [27] G. Liu, and S. D. Gedney, "Perfectly matched layer media for an unconditionally stable three-dimensional ADI-FDTD method," *IEEE Microwave and Guided Wave Letters*, Vol. 10, No. 7, pp. 261-263, July 2000.
- [28] S. D. Gedney, G. Liu, J. A. Roden, and A. Zhu, "Perfectly matched layer media with CFS for an unconditionally stable ADI-FDTD method," *IEEE Trans. on Antennas and Propagation*, Vol. 49, No. 11, pp. 1554-1559, Nov. 2001.
- [29] S. Wang, F. L. Teixeira, "An efficient PML implementation for the ADI-FDTD method," *IEEE Microwave and Wireless Components Letters*, Vol. 13, No. 2, pp. 72-74, Feb. 2003.
- [30] O. Ramadan, "Unconditionally stable ADI-FDTD formulations of the APML for frequency-dependent media," *IEEE Microwave and Wireless Components Letters*, Vol. 14, No. 11, pp. 537-539, Nov. 2004.

- [31] O. Ramadan, "Unconditionally stable ADI-FDTD implementation of PML for frequency dispersive Debye media," *Electronics Letters*, Vol. 40, No. 4, pp. 230-232, Feb. 2004.
- [32] O. Ramadan, "Unconditionally stable nearly PML algorithm for linear dispersive media," *IEEE Microwave and Wireless Components Letters*, Vol. 15, No. 7, pp. 490-492, July 2005.
- [33] J. Chen, Z. Wang, and Y. Chen, "Higher-order alternative direction implicit FDTD method," *Electronics Letters*, Vol. 38, No. 22, pp. 1321-1322, Oct. 2002.
- [34] N. V. Kantartzis, T. T. Zygiridis, and T. D. Tsiboukis, "An unconditionally stable higher order ADI-FDTD technique for the dispersionless analysis of generalized 3-D EMC structures," *IEEE Trans. on Magnetics*, Vol. 40, No. 2, pp. 1436-1439, March 2004.
- [35] W. Fu, and E. L. Tan, "Stability and dispersion analysis for higher order 3D ADI-FDTD method," *IEEE Trans. on Antennas and Propagation*, Vol. 53, No. 11, pp. 3691-3696, Nov. 2005.
- [36] C. Yuan, and Z. Chen, "A three-dimensional unconditionally stable ADI-FDTD method in the cylindrical coordinate system," *IEEE Trans. on Microwave Theory and Techniques*, Vol. 50, No. 10, pp. 2401-2405, Oct. 2002.
- [37] W. Song, Y. Hao, and C. G. Parini, "ADI-FDTD algorithm in curvilinear coordinates," *Electronics Letters*, Vol. 41, No. 23, pp. 1259-1261, Nov. 2005.
- [38] T. Namiki, and K. Ito, "Numerical simulation using ADI-FDTD method to estimate shielding effectiveness of thin conductive enclosures," *IEEE Trans. on Microwave Theory and Techniques*, Vol. 49, No. 6, pp. 1060-1066, June 2001.

- [39] T. Namiki, and K. Ito, "Numerical simulation of microstrip resonators and filters using the ADI-FDTD method," *IEEE Trans. on Microwave Theory and Techniques*, Vol. 49, No. 4, pp. 665-670, April 2001.
- [40] C. Yuan, Z. Chen, "On the modeling of conducting media with the unconditionally stable ADI-FDTD method," *IEEE Trans. on Microwave Theory and Techniques*, Vol. 51, No. 8, pp. 1929-1938, Aug. 2003.
- [41] W. Yuan, and E. Li, "A stable algorithm for interfacing active and nonlinear devices with the ADI-FDTD method," *IEEE Microwave and Wireless Components Letters*, Vol. 15, No. 12, pp. 895-897, Dec. 2005.
- [42] S. Wang, J. Chen, and P. Ruchhoeft, "An ADI-FDTD method for periodic structures," *IEEE Trans. on Antennas and Propagation*, Vol. 53, No. 7, pp. 2343-2346, July 2005.
- [43] H. Rao, R. Scarmozzino, and R. M. Osgood, "An improved ADI-FDTD method and its application to photonic simulations," *IEEE Photonics Technology Letters*, Vol. 14, No. 4, pp. 477-479, April 2002.
- [44] S. Ju, K. Jung, and H. Kim, "Investigation on the characteristics of the envelope FDTD based on the alternating direction implicit scheme," *IEEE Microwave and Wireless Components Letters*, Vol. 13, No. 9, pp. 414-416, Sept. 2003.
- [45] S. Sun, and C. T. M. Choi, "Performance of the improved PML for the envelope ADI-FDTD method in two dimensional domain," *IEEE Microwave and Wireless Components Letters*, Vol. 15, No. 11, pp. 820-822, Nov. 2005.

- [46] C. Ma, and Z. Chen, "Dispersion analysis of the three-dimensional complex envelope ADI-FDTD method," *IEEE Trans. on Antennas and Propagation*, Vol. 53, No. 3, pp. 971-976, March 2005.
- [47] C. T. M. Choi, and S. Sun, "Numerical performance and applications of the envelope ADI-FDTD method," *IEEE Trans. on Microwave Theory and Techniques*, Vol. 54, No. 1, pp. 256-264, Jan. 2006.
- [48] G. Lazzi, "Unconditionally stable D-H FDTD formulation with anisotropic PML boundary conditions," *IEEE Microwave and Wireless Components Letters*, Vol. 11, No. 4, pp. 149-151, April 2001.
- [49] Z. Chen, and J. Zhang, "An unconditionally stable 3-D ADI-MRTD method free of the CFL stability condition," *IEEE Microwave and Wireless Components Letters*, Vol. 11, No. 8, pp. 349-351, Aug. 2001.
- [50] B. Wang, Y. Wang, W. Yu, R. Mittra, "A hybrid 2-D ADI-FDTD subgridding scheme for modeling on-chip interconnects," *IEEE Trans. on Advanced Packaging*, Vol. 24, No. 4, pp. 528-533, Nov. 2001.
- [51] A. Zhao, "More accurate and efficient unconditionally stable FDTD method," *Electronics Letters*, Vol. 38, No. 16, pp. 862-864, Aug. 2002.
- [52] G. Zhao, and Q. H. Liu, "The unconditionally stable pseudospectral time-domain (PSTD) method," *IEEE Microwave and Wireless Components Letters*, Vol. 13, No. 11, pp. 475-477, Nov. 2003.
- [53] G. Sun, and C. W. Trueman, "Approximate Crank-Nicolson schemes for the 2-D finite-difference time-domain method for TE_z waves," *IEEE Trans. on Antennas and Propagation*, Vol. 52, No. 11, pp. 2963-2972, Nov. 2004.

- [54] G. Sun, and C. W. Trueman, "Unconditionally-stable FDTD method based on Crank-Nicolson scheme for solving three-dimensional Maxwell equations," *Electronics Letters*, Vol. 40, No. 10, pp. 589-590, May 2004.
- [55] W. Fu, and E. L. Tan, "Development of split-step FDTD method with higher-order spatial accuracy," *Electronics Letters*, Vol. 40, No. 20, pp. 1252-1253, Sept. 2004.
- [56] L. Xu, and N. Yuan, "PLJERC-ADI-FDTD method for isotropic plasma," *IEEE Microwave and Wireless Components Letters*, Vol. 15, No. 4, pp. 277-279, April 2005.
- [57] J. Shibayama, M. Muraki, J. Yamauchi, and H. Nakano, "Efficient implicit FDTD algorithm based on locally one-dimensional scheme," *Electronics Letters*, Vol. 41, No. 19, pp. 1046-1047, Sept. 2005.
- [58] S. Schmidt, and G. Lazzi, "Extension and validation of a PML formulation for the unconditionally stable D-H FDTD method," *IEEE Microwave and Wireless Components Letters*, Vol. 13, No. 8, pp. 345-347, Aug. 2003.

Chap. 3

- [1] G. D. Smith, *Numerical Solution of Partial Differential Equations*, Oxford, U.K.: Oxford Univ. Press, 1965.
- [2] F. Zheng, Z. Chen, J. Zhang, "Toward the development of a three-dimensional unconditionally stable finite-difference time-domain methods," *IEEE Trans. Microwave Theory Tech.*, Vol. 48, No. 9, Sept. 2000, pp. 1550-1558.

[3] F. Zheng, and Z. Chen, "Numerical dispersion analysis of the unconditionally stable 3-D ADI-FDTD method," *IEEE Trans. Microwave Theory Tech.*, Vol. 49, No. 5, May. 2001, pp. 1006-1009.

Chap. 4

[1] F. Zheng, Z. Chen, J. Zhang, "A finite-difference time-domain method without the courant stability condition," *IEEE Microwave and Guided Wave Letters*, Vol. 9, No. 11, Nov. 1999, pp. 441-443.

[2] A. Taflove and S. C. Hagness, *Computational Electrodynamics: The Finite-Difference Time-Domain Method*, 3rd ed., *Artech House Publishers*, 2005.

[3] D. M. Sheen, S. M. Ali, M. D. Abouzahra, and J. A. Kong, "Application of the three-dimensional finite-difference time-domain method to the analysis of planar circuits," *IEEE Trans. on Microwave Theory Tech.*, vol. 38, No. 7, pp. 849-857, July 1990.

Chap. 5

[1] B. Engquist and A. Majada, "Radiation boundary conditions for the numerical simulation of waves," *Math. Comp.*, vol. 31, no. 139, pp. 629-651, 1977.

[2] R. L. Higdon, "Numerical absorbing boundary conditions for the wave equation," *Math. Comp.*, vol. 49, no. 179, pp. 65-90, 1987.

[3] R. L. Higdon, "Radiation boundary conditions for elastic wave propagation," *SIAM Journal on Numerical Analysis*, vol. 27, no. 4, pp. 831-869, 1990.

- [4] X. Wu, Developing highly accurate and stable open-region electromagnetic simulations, *PhD Dissertation*, 2003.
- [5] O. M. Ramahi, "Application of the complementary operator method to the finite-difference time-domain solution of the three-dimensional radiation problem," *Microwave Opt. Technol. Lett.*, vol. 9, no. 3, pp. 147-149, June 1995.
- [6] O. M. Ramahi, "Complementary operators: A method to annihilate artificial reflections arising from the truncation of the computational domain in the solution of partial differential equations," *IEEE Trans. Antennas Propagat.*, vol. 43, pp. 697-704, July 1995.
- [7] O. M. Ramahi, "Complementary boundary operators for wave propagation problems," *J. Computat. Phys.*, vol. 133, pp. 113-128, 1997.

Chap. 6

- [1] K. S. Yee, "Numerical solution of initial boundary value problems involving Maxwell's equations in isotropic media," *IEEE Trans. Antenna Propagat.*, vol. AP-14, pp. 302-307, May 1966.
- [2] A. Taflove and S. C. Hagness, *Computational Electrodynamics: The Finite-Difference Time-Domain Method*, 3rd ed., *Artech House Publishers*, 2005.
- [3] R. L. Higdon, "Absorbing boundary conditions for difference approximations to the multidimensional wave equation," *Math. Comput.*, vol. 47, no. 176, pp. 437-459, Oct. 1986.

- [4] W. Heinrich, K. Beilenhoff, P. Mezzanotte, and L. Roselli, "Optimum mesh grading for finite-difference method," *IEEE Trans. on Microwave Theory Tech.*, vol. 44, pp. 1569-1574, Sept. 1996.
- [5] R. Vichnevetsky, "Propagation through numerical mesh refinement for hyperbolic equations," *Math. Comput. Sim.*, 23, pp. 344-353, 1981
- [6] J. W. Thomas, *Numerical Partial Differential Equations: Finite Difference Methods*, Berlin, Germany: *Springer Verlag*, 1995.
- [7] R. Vichnevetsky, "Energy and group velocity in semi discretizations of hyperbolic equations," *Math. Comput. Sim.*, 23, pp. 333-343, 1981.

Published Papers:

- [1] M. H. Kermani, and O. M. Ramahi, "The Complementary Derivatives Method: a second-order accurate interpolation scheme for non-uniform grid in FDTD simulation," *Microwave and Wireless Components Letters*, Vol. 16, No. 2, pp. 60-62, Feb. 2006
- [2] M. H. Kermani, and O. M. Ramahi, "The complementary derivatives method for high-accuracy finite-difference time-domain simulations," *Proceedings of 2006 IEEE AP-S International Symposium and USNC/URSI National Radio Science Meeting*, Albuquerque, New Mexico, USA, July 9-14, 2006.
- [3] M. H. Kermani, and O. M. Ramahi, "Reducing truncation error of non-uniform grid size in FDTD methods using the Complementary Derivatives Method (CDM)," *Proceedings of 18th International Conference on Applied Electromagnetics and Communications*, ICECOM 2005, pp. 1-4, Oct 12-14, 2005.
- [4] M. H. Kermani, and O. M. Ramahi, "Unstable 3D ADI-FDTD open-region simulation," *Proceedings of 2005 IEEE AP-S International Symposium and USNC/URSI National Radio Science Meeting*, Vol. 1B, 142-145, Washington, DC., USA, July 3-8, 2005.
- [5] O. M. Ramahi, and M. H. Kermani, "Transmission line resonators for breast tumor detection," *Proceedings of 2005 IEEE AP-S International Symposium and USNC/URSI National Radio Science Meeting*, Vol.3A ,803-806, Washington, DC., USA, July 3-8, 2005.
- [6] M. H. Kermani, and O. M. Ramahi, "The complementary operators method for ADI-FDTD mesh truncation," *Proceedings of 2004 IEEE AP-S International*

Symposium and USNC/URSI National Radio Science Meeting, Vol. 1, 587-590, Monterey, CA., USA, June 20-26, 2004.

[7] M. H. Kermani, and O. M. Ramahi, "Unstable ADI-FDTD open-region simulation," *Proceedings of 2004 IEEE AP-S International Symposium and USNC/URSI National Radio Science Meeting*, Vol. 1, pp. 595-598, Monterey, CA., USA, June 20-26, 2004.

[8] M. Elsabbagh, M. H. Kermani, and O. M. Ramahi, "Accurate broad-band measurement of complex permittivity using striplines," *Proceedings of 2004 IEEE AP-S International Symposium and USNC/URSI National Radio Science Meeting*, Vol. 1, pp. 233-236, Monterey, CA., USA, June 20-26, 2004.

[9] S. Shahparnia, M. H. Kermani and O. M. Ramahi, "Understanding and Validating EMI/EMC Antennas using Numerical Codes," *Proceedings of IEEE International Symposium on Electromagnetic Compatibility*, vol. 2, 2004, pp. 691-696.

[10] X. Wu., M. H. Kermani, and O. M. Ramahi, "Mitigating multi-layer PCB power bus radiation through novel mesh fencing techniques," *Proceedings of 2003 IEEE Conference on Electrical Performance of Electronic Packaging*, pp. 207-210, Oct. 27-29, 2003, Princeton, NJ., USA.

[11] M. H. Kermani, and O. M. Ramahi, "Effects of Segment Length and Number of Turns on Designing a Precise Meander Delay Line," *Proceedings of 2003 IEEE International Symposium on Electromagnetic Compatibility*, Istanbul, Turkey, May 11-16, 2003.

Papers to be submitted:

[12] M. H. Kermani, and O. M. Ramahi, “The complementary derivatives method for high-accuracy finite-difference time-domain simulations,” *to be submitted to IEEE Trans. Antenna Propagat.*

[13] M. H. Kermani, and O. M. Ramahi, “Analytical Investigation of Complementary Derivatives Method,” *to be submitted to Journal of Computational Physics.*

[14] M. H. Kermani, and O. M. Ramahi, “Implementing CDM in the ADI-FDTD method,” *to be submitted to Microwave and Wireless Components Letters.*